An FMCW MIMO Automotive Radar Signal Simulator For Realistic Extended Targets

Yongdian Sun

Delft University of Technology

TU Delft

An FMCW MIMO Automotive Radar Signal Simulator For Realistic Extended Targets

by

Yongdian Sun

To obtain the degree of Master of Science
at the Delft University of Technology(Faculty EEMCS),
to be defended publicly on Thursday August 17, 2023 at 10:00 AM.

Student number:	5200105
Supervisor & Daily supervisor:	Dr. F. Fioranelli & MSc. S. Yuan
Project duration:	March 1, 2022 – August 17, 2023

Thesis committee:	Dr. F. Fioranelli, TU Delft, Associate Professor
	Dr. R.T. Rajan, TU Delft, Assistant Professor
	MSc. S.Yuan, TU Delft, PhD candidate

TU Delft

Preface

This thesis concludes my Master's study at TU Delft and would be a significant milestone in my student career. It was a long journey with unexpected turns, starting from the beginning of 2020. After graduating with a Bachelor's degree in electronics and electrical engineering from the University of Glasgow in 2019, I decided to do a postgraduate study to broaden my horizon. However, the unexpected COVID pandemic changed my study plan and all the courses to online. After two months I moved to the Netherlands. As a consequence, I finished nearly all my studies online on the way to pursue my master's degree.

After the first year of unexpected and tough online study, I got a clearer mind for my study plan and decided to start an extra project as a start in the "Microwave Sensing, Signals and Systems" (MS3) group, which was related to the automotive radar. Later, it was extended to my master's thesis project which will be introduced in the following document.

This thesis aims to build a realistic extended target simulator for automotive radar specific to MIMO FMCW radar. Based on my extra project of analysis and comparison of different open-source real automotive radar data sets, I found the gap in the study of the lack of automotive data and related ground truth information. The idea of setting up a simulator for future study based on the known truth of the environment came to my mind. After doing literature research, I focused the thesis on signal generation for extended targets. In the end, the generated signal was introduced and tested with several beamforming algorithms.

During the trip to the final thesis, it was a great experience to be able to spend a lot of time on a topic and research it in detail. Stepping into a new field is not easy, and I am grateful for all the help and feedback I received. Therefore, I would like to express my gratitude to all the people that supported me during my studies and especially the thesis project.

First of all, I sincerely appreciate my supervisor, Dr. Francesco Fioranelli, and express my deepest thanks to him for all his support in my study and daily life. He always encouraged me to explore my own interests during the thesis and provided help as much as he could. Meanwhile, he was concerned about my daily life in the Netherlands especially when I suffered from accidents.

Secondly, I would like to thank Ph.D. candidate Sen Yuan, my daily supervisor, for his help in guiding me to finish the thesis. I am also grateful to him for supporting me during my hard time.

In addition to that, I am very grateful to Prof. Dr. Alexander Yarovoy for his help in course selection and guidance in my study. Moreover, I would like to thank all the other members of the MS3 group, including lecturers, Ph.D. students, technicians, and MSc student office roommates, for all the useful advice, relaxing discussions, and well-organized activities.

A special thanks are to all the people near me, especially to my apartment roommates, for their help in daily life when I suffered from serious illness, retina detachment, and knee injury.

Last but not least, I thank my family for supporting me morally and financially during my long study journey and always inspiring me and mentally supporting me in my hard time.

Yongdian Sun
Delft, August 2023

Abstract

Nowadays, autonomous driving has been researched for decades, especially with advanced automotive radar. However, there is no common agreement for the best approach to simulations of real-world scenarios of automotive radar. In the academic field of automotive radar research, one of the main obstacles for advanced algorithm development, for instance those based on machine learning, is the lack of real data for developing such algorithms and training them to ensure generalization capabilities. As a strong supplement to experimental measurements, radar signal simulation has made great progress, keeping pace with the revolution in computation and software capabilities. With this, high-fidelity models have become an essential aspect of radar simulation for realistic results with the help of the powerful computer. However, to the best of the author's knowledge, there is no extensive research combining high-fidelity target models with conventional radar simulation techniques.

Therefore, this thesis analyzed the recent radar simulation techniques and proposed a pipeline for an FMCW MIMO automotive radar signal simulator for realistic extended targets and their movement in automotive scenes of interest. Within the proposed simulator, a motion control coordinate system is proposed with high freedom selection of the target model. The shadowing/occlusion condition is also investigated for single and multiple targets cases to increase the reality of the simulation. In the end, by an analysis of the simulated results with the preset ground truth fro CAD models, the simulator has been proved to be able to simulate realistic extended targets with high-freedom for the user.

Contents

Nomenclature

Abbreviations

Abbreviation	Definition
FMCW	Frequency modulated continuous wave
MIMO	Multiple-Input Multiple-Output
ML	Machine learning
MoM	Method of moment
FEM	Finite element method
FDTD	Finite-difference time-domain method
LOS	Line of Sight
RCS	Radar Cross Section
CNN	Convolutional Neural Network
HFSS	High-Frequency Structure Simulator
SBR+	Shooting and Bouncing Rays
GPU	Graphic Processing Unit
UAV	Unmanned Aerial Vehicle
ULA	Uniform linearly antenna
LFM	Linearly Frequency Modulated
CPI	Coherent Processing Interval
HPR	Hidden Point Removal
FFT	Fast Fourier Transform
DoA	Direction of Arrival
MUSIC	Multiple Signal Classifier
MV	Minimum Variance

Symbols

Symbol	Definition	Unit
T	Pulse repetition interval (PRI)	[s]
T_0	Chirp duration	[s]
B	Bandwidth	[Hz]
f_c	Center frequency	[Hz]
f_s	Sample Frequency	[Hz]
N_{Tx}	Number of transmitter antennas	
N_{Rx}	Number of receiver antennas	
N_{chirp}	Number of Chirps	
F_n	Number of Frames	
$\mathcal{N}$	Zero mean White Gaussian Noise	
$\mathbf{A}$	Matrices are denoted by upper-case bold-face letters	
$\mathbf{a}$	Vectors are denoted by lower-case bold-face letters	

Tables

Tables

1 Introduction

In this chapter, an introduction about the need and the differences between radar simulators for automotive and autonomous driving scenes is provided. It is briefly described how in this context a balance between the electromagnetic realism of the simulations and their computational complexity must be found. Specifically, the problem of developing a simulator is formulated for the thesis, which can simulate the radar signatures of extended targets common in automotive scenarios and their (simple) movements. The usefulness of such a simulator for the development of radar signal processing algorithms is highlighted, despite some assumptions to simplify the electromagnetic modeling aspect. The contributions and outline of the thesis are also provided.

1.1. Background

After the 5G era came, with the rapid development of sensing devices and the computing power revolution, automotive driving had become a popular field not only in the car industry but also in the academic community[1]. Nowadays, some application as advanced driver assistance systems (ADAS) has already been used in real life, such as in the Tesla autopilot systems. However, although the concept of (fully) autonomous driving has been widely advertised for many years, there is no commonly established solution for it, also considering the paramount safety of drivers and passengers.

The real-world driving scenario is complex, with many different objects in motion, therefore correct understanding of the scene with suitable sensors is always a bottleneck to making autonomous driving a reality. Focused on situation awareness of automotive driving, computer vision technology based on optical equipment such as the camera or Lidar combined with machine learning had been deeply exploited in the academic field, especially in the past decade [2],[3]. However, the radar-based solution is still in its infancy despite a recent surge of interest. To address the challenges of realistic traffic circumstances, in today's sensing sensor stack, radars have definite perception advantages, especially under low visibility conditions such as rainy days and foggy days, and can provide unique information on the relative velocity and direction of arrival (DOA) of objects, which are crucial for autonomous driving[4].

By applying machine learning (ML) for data processing, an algorithm could reach high-level maturity in a short time with the availability of massive data. In recent years, with advanced radars, ML-based algorithms on radar data have made great progress[5],[6]. At the same time, several experimental radar data sets are openly published for research. In 2018, one of the most famous automotive driving data sets, nuScene[7], was published, which included radar, Lidar, and camera data. Later, Oxford University[8] and the Astyx[9] company released their recorded radar, Lidar, and camera data to the public in 2019. Until 2021, another seven automotive driving data sets contained radar data, namely NLOS[10], CRUW[11], RADIATE[12], CARRADA[13], Zendar[14], RaDICal[15], and Radar Scenes[16], and they were made available for academic research. Comparing the aforementioned data sets (with additional comparison details provided in Appendix A of the thesis), one noticeable characteristic is that all of them include other sensor data such as Lidar and camera, which are mainly used for annotation.

However, with the help of images, it is still time-consuming and complex to manually or semi-manually label all the road users and objects present in the scene. In addition, within different radar data sets, the ground truth categories and the radar data format are different due to the different applied radars, for instance, their resolutions and their operational parameters. Conclusively, experimental radar data sets are relatively small compared with image-based data sets, and this might create difficulties for the implementation of ML algorithms that require a large amount of data for training, such as those for classification and scene segmentation.

Facing inadequate measurement and lack of experimental data, simulation is always regarded as a strong supplementary source of data to perform research. In the radar field, simulation plays an important role before being applied to the practice and great progress had been made in the past years[17]. The revolutionary development in computation power made it possible to model radar signals as realistically as possible since the complex electromagnetic wave propagation could be calculated with exact solvers and/or with the ray tracing method. Specifically, full-wave simulation, using the method of moment (MoM)[18], finite element method (FEM)[19], and finite-difference time-domain method (FDTD)[20], implements and solves the complete Maxwell equations' set during wave propagation, and can provide high-accuracy simulated data. However, they require relatively heavy computation, which increases with larger scenes and with higher operation frequencies, such as indeed the mm-wave band occupied by automotive radar. Nevertheless, for automotive radar simulations, the simplified asymptotic method is more widely used [21].

To conclude, radar simulators for automotive scenes are needed and a lot of research is performed to make them efficient and effective, with several variants proposed to address the need of the specific application at hand and strike the balance between computational requirement and electromagnetic fidelity.

1.2. Radar simulators: brief State of Art

In the past years, several automotive radar signal simulators have been proposed. These are briefly summarized here and described in detail in the Literature Review chapter. One of the most famous applications is the backscatter radar signal function integrated into MATLAB with the walking pedestrian model and the bicycle model, using simplified point scatters [22],[23]. In 2020, X. Lin proposed an automotive radar simulator structure concerned with realistic interference in signals such as measurement errors [2]. Later, an automotive radar simulator that could generate micro-Doppler information based on the high-fidelity physics model was put forward by U.Chipengo[24],[25]. Contemporaneity, C. Schüßler and J. Thieling published the paper for the simulator using an improved ray-tracing model and scalable and physical radar sensor simulation[26][27]. The latest research about radar simulation is published in 2022 by M. Moore, which simulated the micro-Doppler signal for unmanned aerial vehicles (UAV) with dynamic point clouds [28]. Additionally, S. Xu from the MS3 group of TU Delft built a car model for automotive radar in his research for joint parameters estimation using FMCW UWB waveform [29]. Last but not least, commercial software simulators, such as FEKO and Ansys, provide the solution of virtual traffic scene simulation for automotive radar.

Reviewing the different simulators and their characteristics, it appears that nearly most of them are designed for special cases, and some of them require rather heavy computation, especially involving complex ray tracing calculation. Therefore, there is still a gap in designing a simulator with realistic models of common automotive targets of interest and their flexible motion control, using a simplified ray tracing calculation concerned with shadowing problems between objects. Albeit simple, such a simulator can still be extremely useful for the development of radar signal processing algorithms in the field of automotive radar, prior to their extensive verification with experimental data.

1.3. Problem formulation and thesis contribution

Except for advanced commercial software, radar simulators for realistic extended targets in automotive are an active area of research, especially because there are many possible ways to characterize the complexity of the targets' shape and their motion information. Therefore, the problem of this thesis is formulated to establish a simulator for realistic extended targets in automotive radar, such as vehicles and pedestrians. The simulated radar signal should be able to reflect the authenticity of the targets' signatures to the point that they can be used for the development and initial verification of radar signal processing algorithms while maintaining computational feasibility. However, it is important to note that the implementation of a fully accurate EM simulator goes beyond the scope of this thesis.

The main contributions of this thesis can be summarized as follows:

- Established a processing pipeline for an FMCW MIMO radar simulator, starting from the fundamental raw, complex-valued signals.
- Set up a series of coordinate systems and equations of motion to describe the main movements of targets of interest in automotive.
- Verified the proposed simulator with several target categories and their dynamic point clouds.

1.4. Thesis outline

This thesis proposed an extended target radar signal simulator for the FMCW MIMO radar, scoping on the motion control of the target and involving shadowing calculation based on realistic 3D models. The outline of the thesis is as follows.

In chapter 2, a detailed literature review is presented for recent radar signal simulators, including a comparison at the end of the chapter. Chapter 3 describes the procedure and methodology of building the proposed simulator. Specific details for the signal model, target model, and motion control are stated in the chapter. The following chapter, chapter 4 introduces the theoretical derivation of traditional radar signal processing techniques which are then used in the later simulated results. In chapter 5, simulated results of the proposed simulator are shown. The last chapter, chapter 6, concludes the thesis.

2

Literature Review

In this chapter, a review of recent papers and studies about automotive radar simulators will be provided in the different sections, starting from the single target simulator in MATLAB to the more complex electromagnetic commercial software. At the end of the chapter, a comparison of the simulators and an analysis of the gaps are introduced, as a closure for the literature review and a motivation for the work of the thesis.

2.1. MATLAB-based simulator [22],[23],[30]

As one of the most widely-used engineering tools in the world, MATLAB provides radar signal simulation with preset functions and toolboxes. Two of the most famous models are specially designed for a walking pedestrian and a cyclist shown in Fig.2.1 from version R2019a and R2021a.

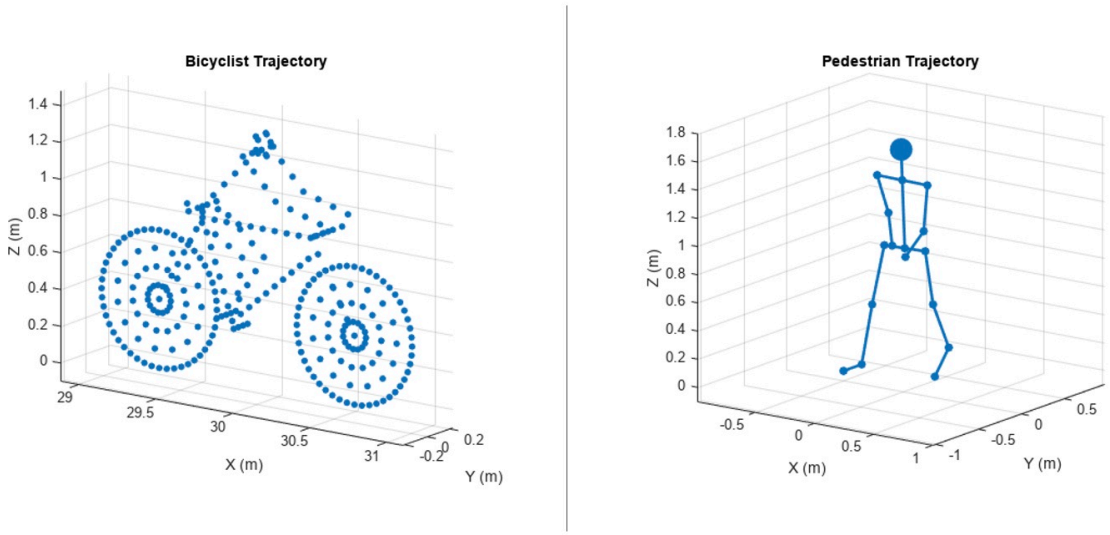

Figure 2.1: Pedestrian model and cyclist model implemented in MATLAB for their radar simulator[22],[23]

It is noticeable that this simulator is mainly for micro-Doppler signal generation based on the theory that came up by V. Chen [31] in 2011. Focused on the targets models, the walking pedestrian model was first put forward by R. Boulic [32], and the cyclist model was introduced by M. Stolz[33]. In detail, The height and the walking speed of the pedestrian are adjustable to generate different reflected signals. More flexible parameter presetting integrated with the cyclist model with the changeable number of scatters, gear transmission ratio, and RCS patterns.

Additionally, there is another scene simulator for automotive radar integrated into MATLAB named 'Radar Signal Simulation and Processing for Automated Driving'. This simulator is specially designed for simulated highway scenarios for automotive radar in a long range. The illustration figure is shown as followed in Fig. 2.2

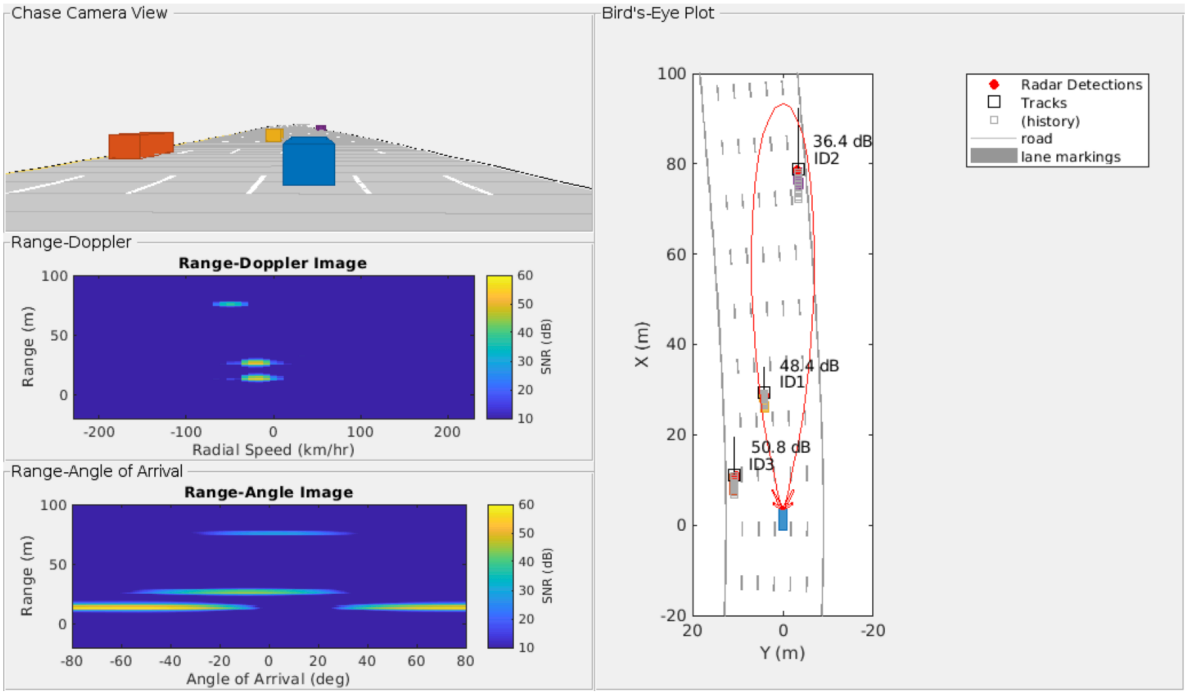

Figure 2.2: Highway radar scene simulator implemented in MATLAB[30]

In this simulator, the target model is simplified into the cuboid box with a certain velocity for generating the reflected signals from radar. At the same time, considering the radar signal propagation in reality, it provides the multi-path radar signal generation, specified for a one-time bounce on the road surface. As a result, the target signal will be spread more widely in range compared with free-space propagation.

In summary, MATLAB, as a powerful tool, provides a convenient platform for radar signal simulation, especially in signal generation. It is a friendly-used startup for learning radar signal simulators. However, due to the limit of integrated functions, it could not always generate specific radar data for use.

2.2. Car simulator by S.Xu [29]

As part of his Ph.D. research of joint parameters estimation using FMCW UWB waveform, Dr. Xu set up this simulator to simulate the validation data to testify the algorithm of motion-based separation and imaging of closely-space extended target [34]. In his simulator, there are two parts for radar signal generation, radar, and target. Firstly, because of his interest in research, the integrated function in MATLAB could not generate the desired signal which contained Doppler shifts under high-speed velocity with an ultra-wideband (UWB) signal. Therefore, he provided the details of the process of generating FMCW radar signals with mathematical expression.

The target model in his simulator originated from a single-car model shown in Fig. 2.3. To model the reflection signal, 137 dominant scatter points are selected from the car model with a uniform distribution of amplitudes on each point. Additional complex Gaussian noise was added in the simulation as well. Later, the validation scene for target separation was built with preset car velocity and acceleration, starting at different initial positions in 2D space illustrated in Fig. 2.4 a), and the reconstructed scene showed in Fig. 2.4 b).

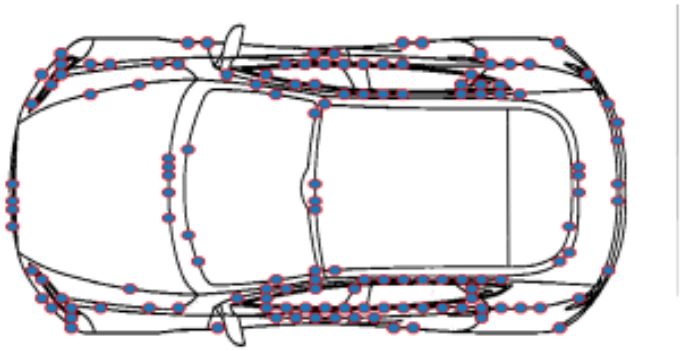

Figure 2.3: Single car model made of multiple radar scatter points used by S. Xu [34]

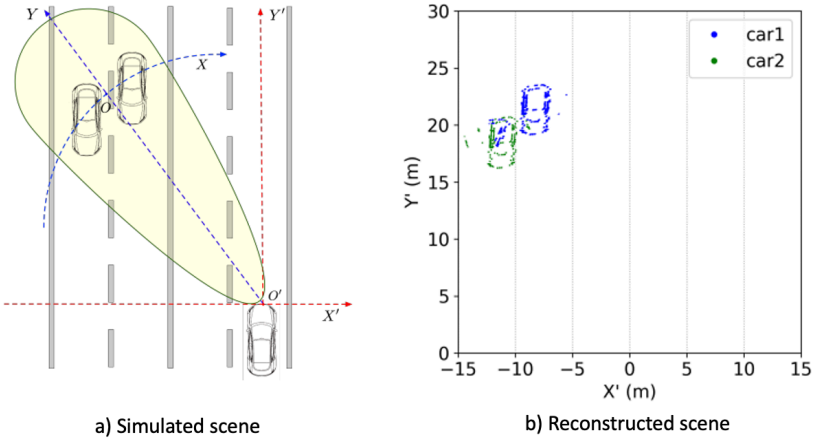

Figure 2.4: An example of a simulated scene with two cars seen by an automotive radar on a third car at the origin using the model proposed by S. Xu [34]

Compared with other radar signal simulators, Dr. Xu's car simulator is highly customized based on his interest in research. Only the line of sight(LOS) in the azimuth domain, without elevation, information is concerned in the simulation.

2.3. Simulator by X. Li [35]

In 2019, X. Li introduced their research on the millimeter wave simulation model for automotive driving. Performance analysis of the radar detection was invested. Therefore, the automotive radar simulator is separated into two parts, the radar physical model and the radar geometry model, and the modeling architecture illustration is shown in Fig. 2.5.

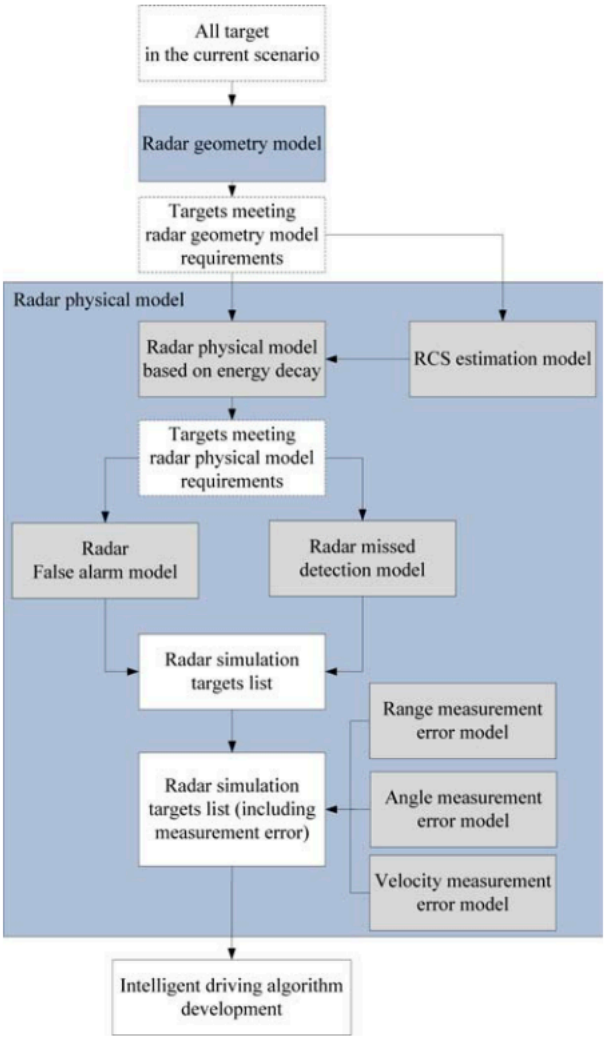

Figure 2.5: Radar simulator architecture proposed by X.Li [35]

Before radar signal generation in the radar physical model, the target geometry information is first calculated in the radar geometry model to figure out the intersection and occlusion between different targets based on the distance to the radar shown in Fig.2.6. Specifically, green target 2 and red target 1 are detectable by radar, while purple target 3 is unable to be observed by radar due to the occlusion with red target 1.

As another output from the radar geometry model, the RCS estimation process was illustrated in Fig. 2.7, where the left part showed the target model of car and pedestrian, and the right part showed the RCS value calculation equation. In his simulator, the target list contained simplified car and pedestrian models from different observation angles by radar, which referred to the D value in the right part equation. S value represented the surface area in the simplified target model. Material reflectivity of the target surface also was a concern in the RCS estimation referred to as the W in the equation.

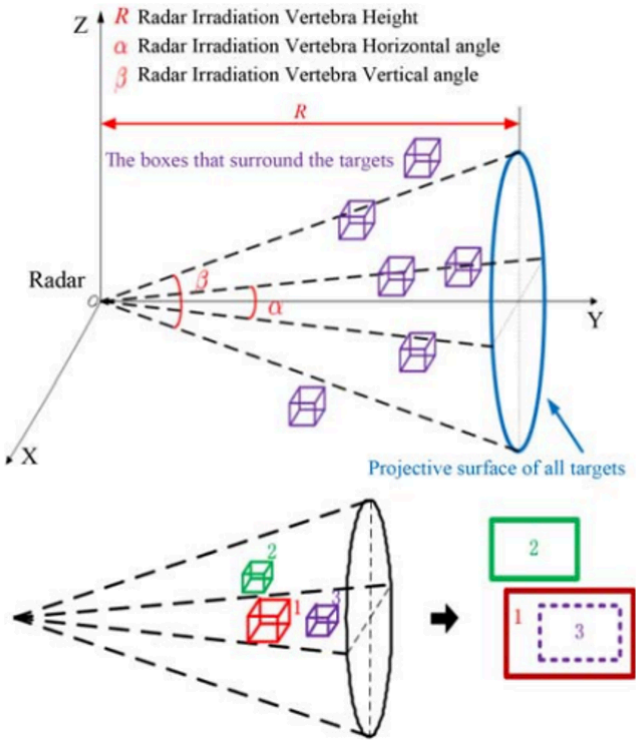

Figure 2.6: Target geometry relationship in the radar simulator proposed by X. Li [35]

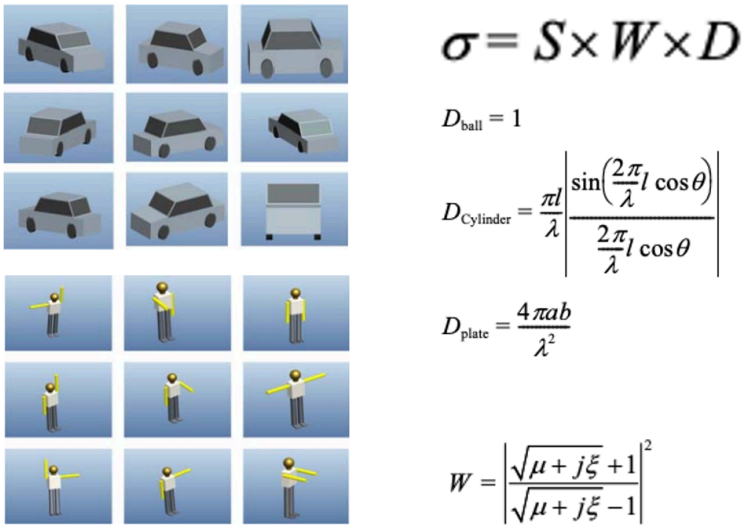

Figure 2.7: RCS estimation model for car and pedestrian in the simulator proposed by X. Li [35]

In the radar physical model, false detection signals, missed detection signals, and measurement errors are concerns in the simulation as one of the innovations for the simulator architecture based on the system analysis of influence factors on both radar and environment scenes. Figure 2.8 indicated the scene for the false detection case and the missed detection case. In reality, multipath propagation may lead to incorrect detection for radar and limit radar velocity ambiguity may fold the high-speed target into background noise caused by stationary targets or the environment. Therefore, in X. Lin's

research, false detection and missed detection model are introduced to simulate the influence of the real scene.

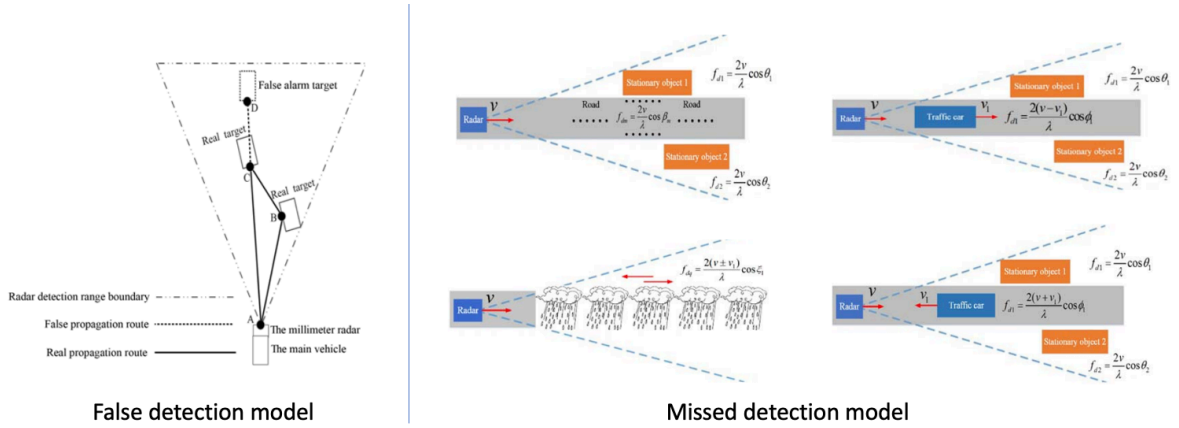

Figure 2.8: False detection and Missed detection model [35]

Additionally, measurement error caused by radar is also formulated based on real radar experiments. Three new factors, range measurement error, velocity measurement error, and angle measurement error, are put forward with the equations shown in the inset Fig.2.9.

$$\Delta R = \frac{1}{0.6 \times \sqrt{2\pi}} \exp\left(-\frac{x^2}{0.72}\right)$$

$$\Delta V = \frac{1}{0.14 \times \sqrt{2\pi}} \exp\left(-\frac{x^2}{0.02}\right)$$

$$\Delta \phi = \frac{1}{\sqrt{2\pi}} \exp(-x^2)$$

Figure 2.9: Measurement errors equations[35]

Conclusively, X.Li work systematically analyzed the radar simulation for automotive radar and provide a good example for future development. Meanwhile, a comparison with the commercial software FEKO validated that the radar simulator design significantly reduces the computation time and could provide likely simulated data.

2.4. Simulator by U. Chipengo [25]

As part of work related to the Ansys simulator, U.Chipengo published his research involving micro-doppler signal generation for CNN-based classification in 2021. In the paper, a comprehensive, large-scale, spectrogram-based classification study involving pedestrians, cars, cyclists, and dogs, and a high-fidelity, physics-based simulation approach related to mentioned road users were proposed. Figure. 2.10 shows the difference between different models-based methods for generated signals in radar research.

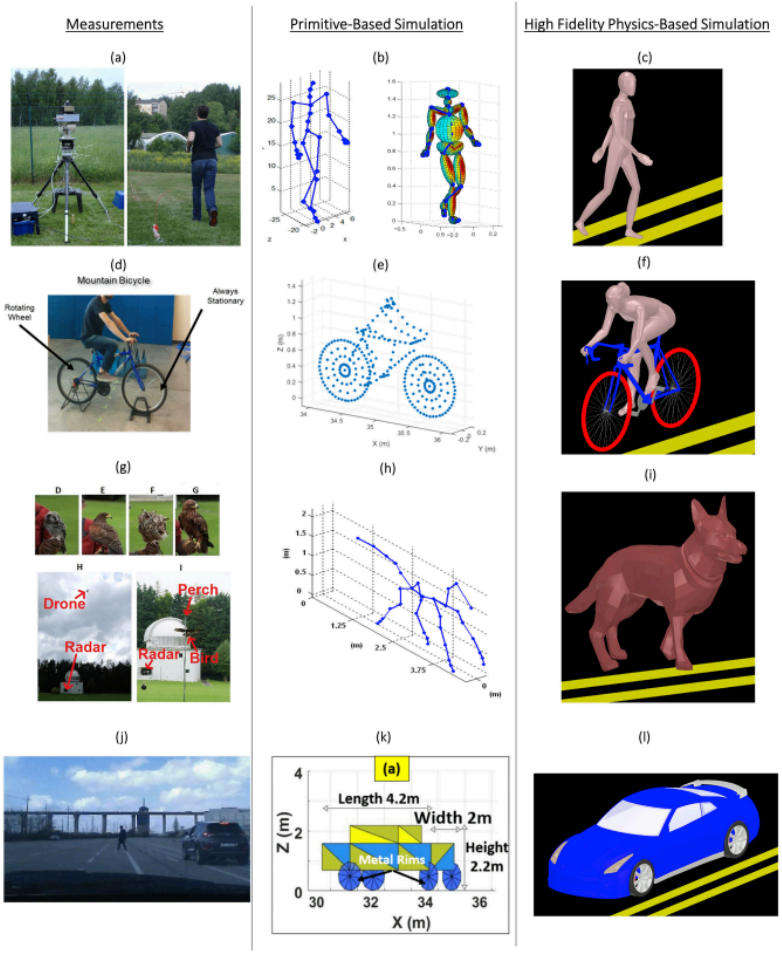

Figure 2.10: Signal generation methods with different models, as proposed by Chipengo [25]

Compared to each other, high-fidelity physics-based simulation is more accurate than primitive-based simulation with less cost considering the real measurements. To be more specific, the radar signal is generated based on the shooting and bouncing ray approach for accurate spectrograms for full-scale representatives of the models. Meanwhile, the micro-doppler information is generated with a modified coordinate system shown in the left of Fig. 2.11. In detail, the anchor points and rotation points are defined in 3D models of road users to calculate the rotation or oscillation movement which leads to the micro-doppler signals. The right figure in Fig. 2.11 shows the linear velocity calculation based on the equation $v_{linear} = \omega * r$, where the spheres represent the non-rigid target rotation or oscillation parts in addition to the bulk translation.

With the help of High-Frequency Structure Simulator (HFSS) Shooting and Bouncing Rays (SBR+) solver from Ansys, the simulated data is available for further CNN classification. The real measurement of single pedestrian and cyclist validated the simulated results. Figure 2.12 shows the simulated results at different angles of arrivals.

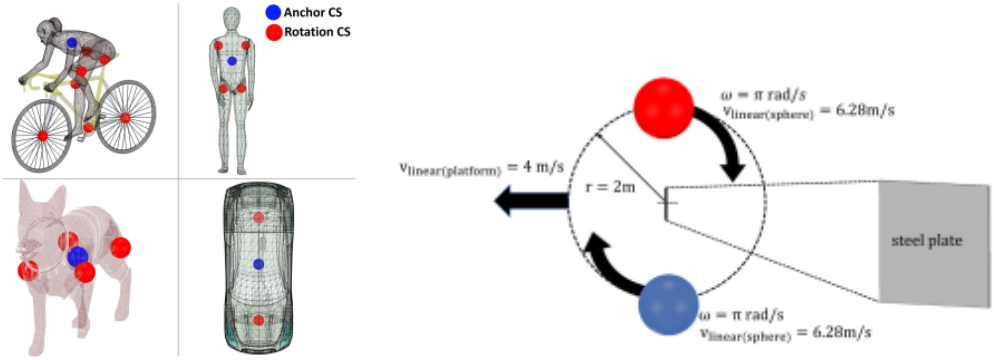

Figure 2.11: Coordinate system for radar micro-Doppler generation in the simulator by Chipengo [25]

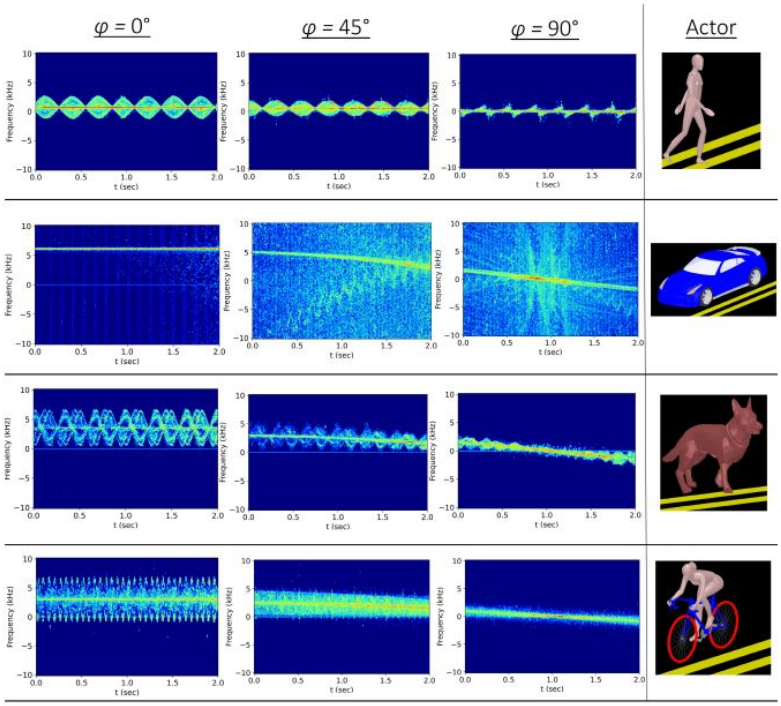

Figure 2.12: Simulated data for different targets under different angles of arrival, as generated by the simulator proposed by Chipengo [25]

2.5. Simulator by C. Schüßler [10]

Schüßler published his large MIMO arrays simulator in 2021, focused on the elimination of phase errors caused during radar signal propagation between the transmitter antenna and receiver antenna. The left figure in Fig. 2.13 illustrated the case which leads to the phase error. Based on his simulator, the propagation path from different transmitter antennae to the same receiver antenna would merge at the first hit point. Due to the large computation on the calculation of wave propagation between antennae, Nvidia raytracing Engine is merged in the simulator, where right figure Fig. 2.13 shows the structure of the software architecture mainly contains the radar trace generation and IF-signal generation.

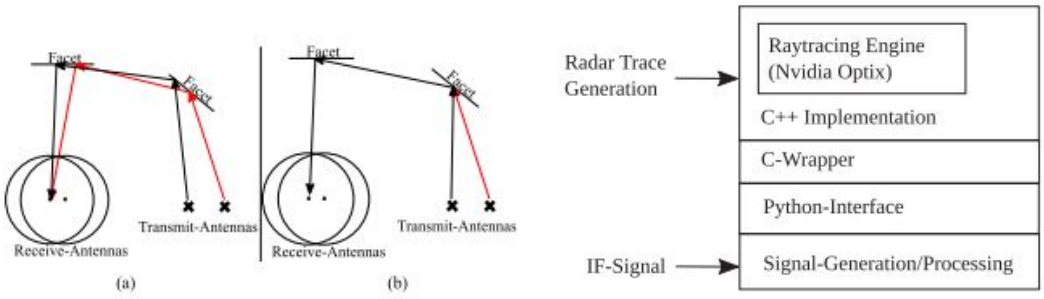

Figure 2.13: Illustration the cause of phase error, and proposed radar simulator structure [10]

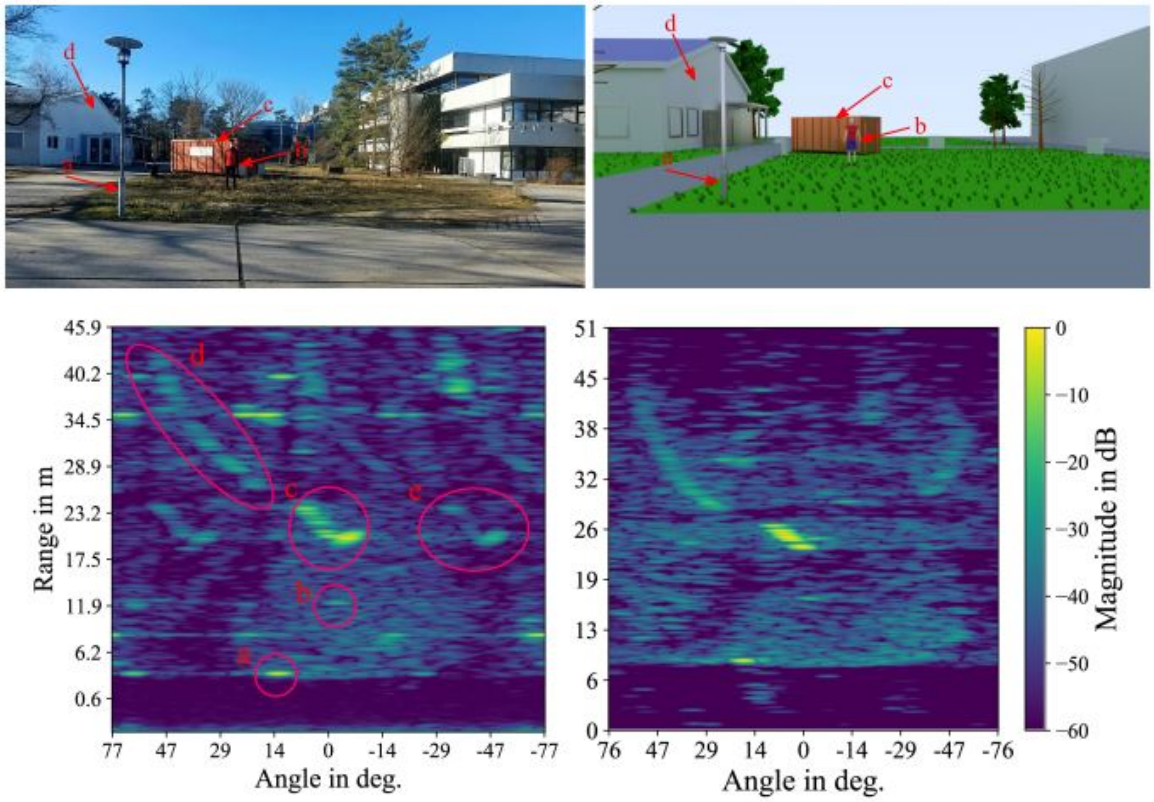

Figure 2.14: Measurement and simulation comparison of a scene to validate the simulator proposed by Schüßler [10]

Figure.2.14 shows the validation procedure between measurement data and simulated data. Compared with other simulators, Schüßler's simulator is only available for the static scene, however, one advantage of his simulator that could not be ignored is that the camera scene shown in the above figure could be simulated simultaneously.

2.6. Simulator by J. Thieling [27]

A generalized and physical radar sensor simulation model came up by J Thieling in 2021, which focuses on providing a solution for functional validation of radar-based applications independent of their domain or manufacturer based on highly detailed but generic virtual 3D environments. In Fig. 2.15, the reusable structure of the modeling radar sensor is given by J. Thieling, where the system is made of three parts, radar sensor, information carrier, and 3D scene object.

Figure 2.15: Physical structure of modeling radar sensor with reusable building blocks proposed by Thieling [27]

In the radar sensor part, three factors are considered, antenna power distribution and signal modulation shown in Fig. 2.16, and receiver noise. Due to the purpose of generalized simulation, the Fibonacci-lattice method is chosen because of its even distribution feature. Several typical modern automotive radar modulation technique is introduced with correlated resolutions in range and velocity, and the noise on the receiver antenna is also mentioned as the

$$P_{r,min} = P_n * SNR_{min}$$

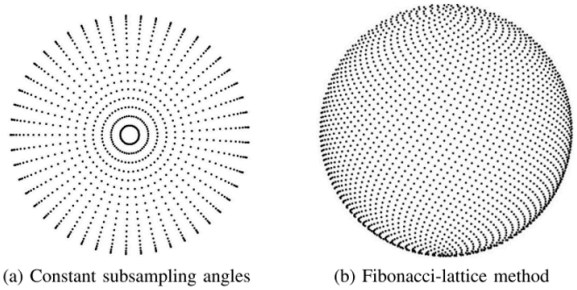

(a) Constant subsampling angles (b) Fibonacci-lattice method

Antenna Power distribution

Modulation Type	Distance Resolution	Velocity Resolution
Pulsed Radar	$\Delta d = \frac{c\tau_p}{2}$	n.a.
CW Radar	n.a.	$\Delta v = \frac{c}{2\tau_{cw} f_0}$
FMCW Radar	$\Delta d = \frac{c}{2\Delta F}$	$\Delta v = \frac{c}{2f_0}\frac{1}{T_m}$
Chirp-Sequence Radar	$\Delta d = \frac{c}{2\Delta F}$	$\Delta v = \frac{c}{f_0 \tau_p}$
Pulse-Doppler Radar	$\Delta d = \frac{c\tau_p}{2}$	$\Delta v = \frac{c}{2f_0 \tau_{cw}}$

Signal modulation technique

Figure 2.16: Radar sensor characteristics, as implemented in the simulator by Thieling [27]

Focused on the information carrier, atmosphere attenuation, and rain scattering are detailed and explained, where multi-path propagation is merged into the 3D object part considered different reflections on the surface of the targets. An intensity function at the radar receiver is derived from the radar equation shown below, where the coefficient changes under different environments such as rainy days.

In the 3D object model, the target is a set of triangle mesh with generic geometry shown in Fig. 2.17. With the help of GPU, all the algorithms mentioned before combine together for simulation. Figure. 2.18 indicates the structure of GPU use.

Figure 2.17: Car model in 3D as an object for the simulator [27]

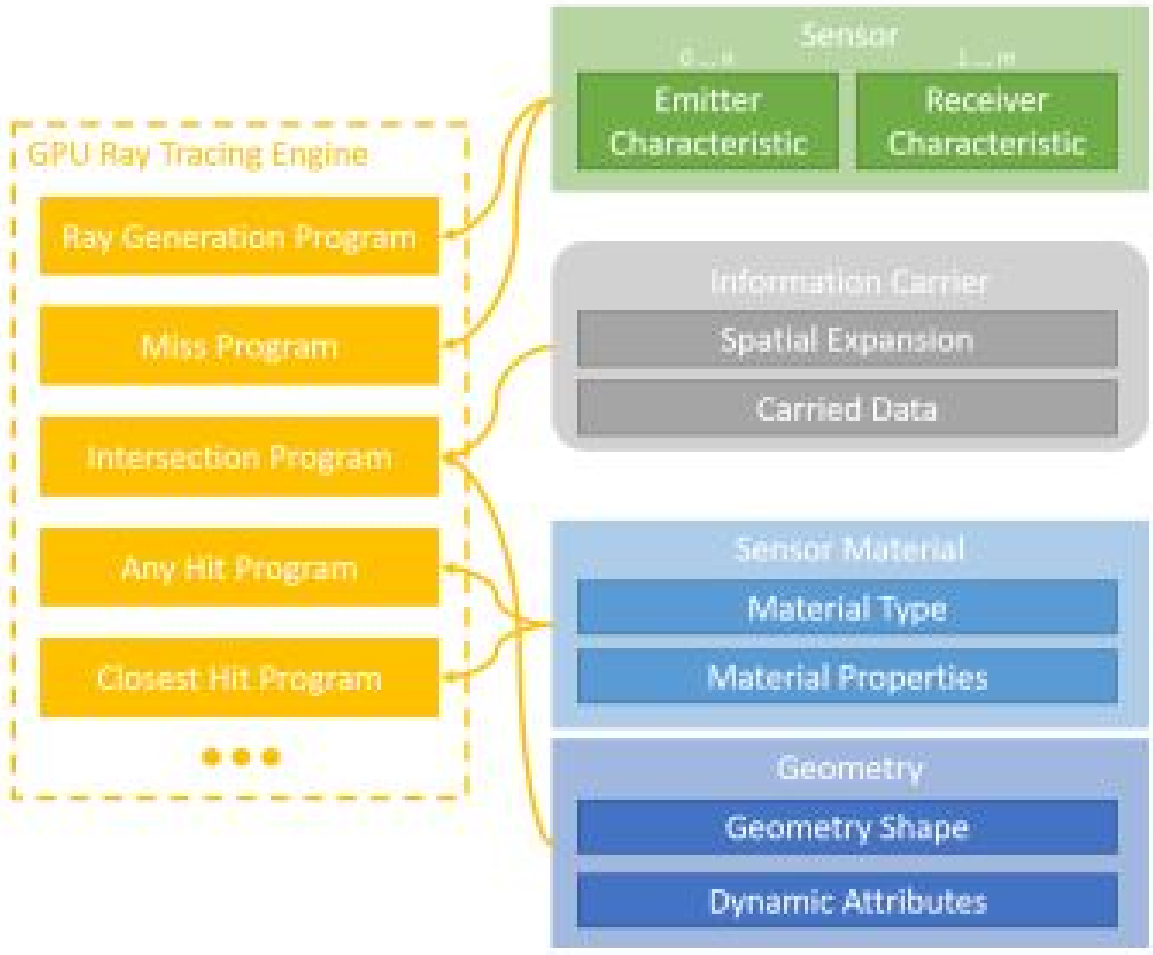

Figure 2.18: GPU structure for simulation as proposed in [27]

2.7. Simulator by M.Moore [28]

In 2022, the simulation for UAV micro-Doppler using dynamic point clouds is introduced by M. Moore. Based on his paper, point clouds derived from a 3D CAD model are used to generate the micro-Doppler information for the classification of the different UAVs. Figure. 2.19 illustrates the pipeline of simulation. After the superposition of returned radar signals from observed points, the simulated spectrograms are available for classifying different UAVs.

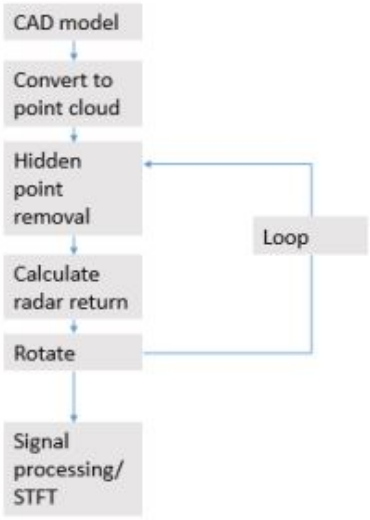

Figure 2.19: Flow chart of simulation proposed in [28]

With the help of the hidden point removal algorithm, the point clouds of the UAV propeller shown in Fig. 2.20a could be filtered out the points that are not in the line of sight of radar. Figure.2.20b shows the dynamics of the system with respect to the radar

(a) Point clouds of the UAV propellers [28]

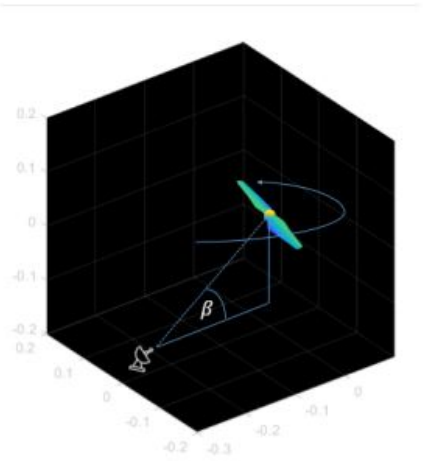

(b) Dynamics of the simulated system [28]

2.8. Comparison of reviewed simulators and gaps

Before comparing the aforementioned simulators from the literature, it is notable that, nowadays, advanced commercial software is available to simulate radar signals with very high accuracy by fully simulating the radar signal during the propagation using powerful solvers, such as FEKO, and Ansys. However, although very accurate, this software is relatively costly in terms of licensing and may not scale well to the large, complex scenes required in realistic automotive radar scenarios, especially at the mm-wave frequency band.

Table 2.1: Comparison between different simulators reviewed in this chapter

Simulator	Radar signal model	Object	Extra servers	Dynamics
MATLAB[22],[23],[30]	FMCW	Primitive model (pedestrian, cyclist, cars on the highway)	No	Yes (translational)
S. Xu [29]	FMCW MIMO	2D car model	No	Yes (translational)
X. Li[35]	FMCW	Primitive model (car and human)	No	Yes (translational)
U. Chipengo[25]	FMCW	3D Target	Yes	Yes (translational and rotaional)
C. Schüßler[10]	FMCW MIMO	3D Target (scene simulator for CARLA)	Yes	No
J. Thieling[27]	Multi-type (FMCW/Pulsed)	3D Target (triangle meshes)	Yes	Yes (translational and rotational)
M.Moore[28]	FMCW	3D Target (point clouds of UAV propellers)	No	Yes (rotaional)

Based on the listed literature review, it is clear that in the research of radar signal simulators, improvement of signal realism is significant, especially with the help of advanced servers, such as Nvidia ray-tracing engine or other servers from commercial software. A lot of attention has been focused on the improvement of simulated realistic wave propagation. Table 2.1 shows the difference between the aforementioned simulators. It is clear that there is a gap in combining realistic 3D extended objects with a conventional radar simulator, i.e., a simulator that does not aim for extreme electromagnetic fidelity, and yet can generate signals and signatures helpful to develop and assess the feasibility of radar signal processing algorithms. Even if not focused on automotive scenarios, M. Moore's simulator [28]shows the possibility of applying 3D point clouds to generate multi-targets radar signals for classification.

2.9. Summary

In summary, the analysis of the literature on existing simulators for radar signals and scenarios has shown that there are many multiple variants with different characteristics, depending on the application to target. In general, a trade-off is present between computational requirements and electromagnetic fidelity. A gap is found in the development of a simulator to reproduce radar signatures of extended 3D targets common in automotive scenarios and their simple movements. Such simulator can be useful to support the validation of radar signal processing algorithms beyond very simplistic, ideal point targets, prior to more extensive validation with real, experimental data. This is what the following work described in the thesis will focus on.

3

Methodology of the Proposed Simulator

In this chapter, the methodology for the proposed simulator will be introduced. Specifically, its pipeline will be described, starting from the structure of the simulator design, followed by its sub-system blocks, such as signal model, target model, shadowing calculation, and motion control of the targets of interest.

3.1. Simulator structure

As the basis for the radar signal simulation, the structure design of the radar system plays an important role in the simulation of the radar signal. In literature reviews, X. Lin and J. Thieling mentioned the general radar system structure as shown in Fig 2.5 and Fig.2.15. Besides that, S. Xu provided another basic radar simulator case for radar signal simulation. In general, a radar simulator could be made of three main sub-systems, namely the radar physical model, the target model, and the radar signal propagation model between radar and targets in the scene. Specifically, the radar model defines the simulated signal/waveform based on the radar settings, while the target model includes the geometry/shape information and radar cross-section (RCS) information for the reflected radar signal. Within the signal propagation model, multi-path propagation, radar signal power attenuation, and other possible error signals can be considered, for instance, interference from the environment or other radar emitters. Inspired by the above cases, the automotive radar simulator in this thesis is designed as shown in the flow chart below, see Fig.3.1.

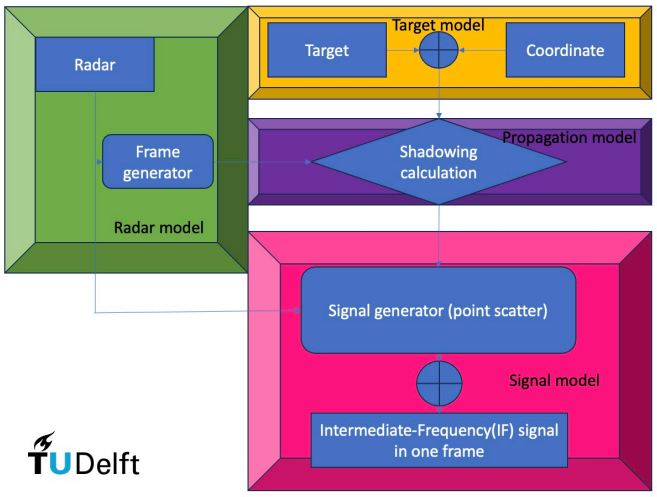

Figure 3.1: Proposed radar simulator structure with its main blocks (models)

In detail, the radar simulator contains four sub-models, radar, target, propagation, and signal model. The radar setting and frame generation are defined in the radar model, with input parameters of radar and observation time. The frame information is generated simultaneously for later signal generation. Within the target model, the target 3D point scatterer characteristics and target motion information including translation and rotation movements are generated by the simulator. The propagation model calculates the shadowing in 3D spatial coordinates based on the target model information frame by frame. In the end, the reflected signal is generated for only the observed point scatterers, i.e. those that are not occluded by direct propagation path with respect to the radar.

3.2. Radar model

In this model, the radar signal/waveform is defined with the desired settings including radar characteristics, and observation time of the whole simulation. As an example to demonstrate the simulated signals in the later simulation results chapter (chapter 5), the widely-used FMCW MIMO radar signal is chosen, as the main type of radar employed in state-of-the-art automotive applications.

3.2.1. Radar (FMCW MIMO radar)

As one of the most widely-used automotive radar, in addition to the common radar advantage of weather/light robustness, FMCW MIMO radar has superiority [36] in:

- Relatively large RF bandwidth and low interference with other radar sensors
- High accuracy in range, velocity, and angular measurement for multi-target cases
- Small compact size and complementary capabilities to other sensors such as camera and Lidar
- Relatively low cost in power consumption and manufacture

FMCW signal design:

In the designed simulator, linear frequency-modulated continuous wave (LFMCW) is applied to signal generation. The range information of the target can be extracted from the FMCW waveform by calculating the phase difference/frequency change caused by round-trip delay based on the characteristics of the waveforms. Figure. 3.2 demonstrates the LFMCW signal modulated technique, where T and T_0 represent chirp duration and pulse repetition interval (PRI), respectively.

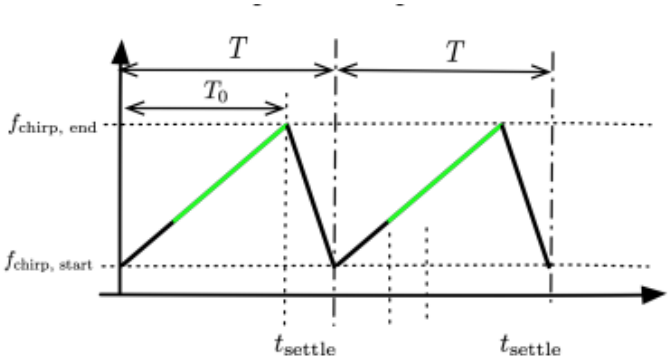

Figure 3.2: Illustration of the LFMCW signal modulation (upward ramp sawtooth modulation)[34]

MIMO Channel design:

As another important part of the radar signal simulation, MIMO channels provide the additional dimension of angular information, simultaneously with range and Doppler information. Figure. 3.3 shows an example of a uniform linearly antenna (ULA) MIMO channel with two transmitted antennae and four received antennae, which provides eight channels in signal processing by transforming the real antenna array into a virtual antenna array. These can then be used to estimate the angle of arrival of the signal, i.e., the angular position of targets of interest.

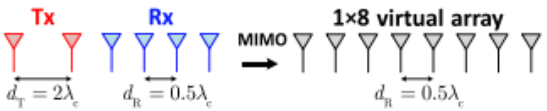

Figure 3.3: MIMO channel array illustration

T	Pulse repetition interval(PRI)	B	Bandwidth of the radar signal
T_0	Chirp duration	N_{Tx}	Transmitter
f_c	Center frequency of the radar	N_{Rx}	Receiver

Table 3.1: Main radar parameters to be defined in the simulator

In summary, based on the previous analysis, Table 3.1 shows the crucial radar parameters for signal/waveform simulation. With additional preset radar coordinates in a 3D Cartesian system, also known as the world coordinate system, the radar waveform can be generated as described in the following content.

3.2.2. Frame generator

In real radar data measurement, such as using TI radar board[37], the radar received signals are collected beats by beats, also known as frames by frames, wherein each beat/frame several chirps signals are generated based on different radar settings. Therefore, in simulation, the total number of chirps in the frame needs to be determined in advance with the mathematical expression shown below, where F_n represents the total number of chirps in the frame, $T_{observation}$ refers to the total observation time for the simulation, N_{chirp} and T is related to the radar waveform setting of chirp number and pulse repetition interval for signal generation. Considering the uneven case during the calculation, the rounding ceiling function is added to generate a correct, integer number of chirps per frame.

$$F_n = \lceil \frac{T_{observation}}{N_{chirp} * T} \rceil \tag{3.1}$$

3.3. Signal model

In this section, the detailed derivation of the simulated signals backscattered from the target will be given. Prior to starting with the mathematical expression, some assumptions need to be defined about the generality of the chosen approach:

- Monostatic antenna array with one transmitter and L receivers
- Uniformly distributed linear array (ULA) with omnidirectional elements
- Points scatterers with identical RCS values/distributions located in the far field of the antenna array

In terms of subsequent signal processing in the pipeline of the simulator, techniques such as matched filter and de-chirping technique are widely used to process the received signal to remove the frequency modulation and extract the target signal depending on the later intended application such as detection and classification. Compared with matched filters, the de-chirping technique has the advantage of withdrawing the target signal from the modulated frequency and down-converting it to the baseband signal with reduced sample frequency, especially for linear frequency modulation (LFM) chirp signals. Figure 3.4 shows a sketch of the process of the de-chirping technique. The green and blue lines represent the transmitted and received signals, respectively, while the red line refers to the de-chirped signal obtained by the instantaneous frequency difference, also known as the 'beat signal', containing range information as well as Doppler information. However, in a single-beat signal, the Doppler information is usually neglected since it is much smaller for objects of interest in automotive. The Doppler information can however be estimated by using multiple beat signals.

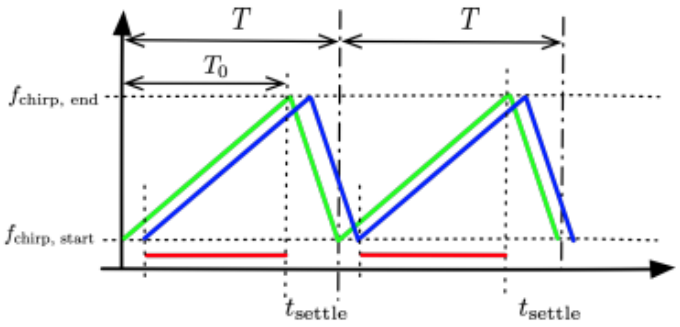

Figure 3.4: Illustration of the de-chirp technique at the receiver of an FMCW radar [34]

3.3.1. Point scatterer signal model

Based on the aforementioned assumptions, the radar signal is defined for *I* observed point scatterers in one captured frame, assumed to be within one coherent processing interval(CPI). They have known initial range $\mathbf{r} = \{R_1, R_2, R_3, ..., R_i\}$, velocity $\mathbf{v} = \{V_1, V_2, V_3, ..., V_i\}$, and angle with respect to the radar $\Theta = \{\theta_1, \theta_2, \theta_3, ..., \theta_i\}$. An FMCW chirp transmitting signal with chirp duration (T_0) and pulse repetition interval (T) can be written in the normalized mathematical expression shown below based on the Fig. 3.2:

$$s_0(t) = \begin{cases} e^{j2\pi(f_0 t + \frac{\mu t^2}{2})}, & t \in [0, T_0] \\ reset/resettle, & t \in (T_0, T) \end{cases} \tag{3.2}$$

where in this form f_0 represents the starting frequency calculated with $f_0 = f_c - \frac{B}{2} = f_{chirp,start}$, and μ refers to the frequency modulation rate $\mu = \frac{B}{T_0}$.
Extending the single chirp transmitted signal to multi-chirps and introducing T_{total} which refers to the total observation/simulated time, the transmitted signal would become as in Equation (3.3), where $t = t^* + mT$, and m represents the chirp number within the whole observation time ($m = 0, 1, 2, 3, ..., M-1$).

$$s(t) = s(t^* + mT) = s(m, t^*) = s_0(t^*), t \in (0, T_{total}), t^* \in (0, T) \tag{3.3}$$

Therefore, we can write the expression for the known round trip delay of the ith point target shown in Equation (3.4), where R_i and v_i are initial range and radical velocity, and c is the light speed in free space.

$$\tau_i(m, t^*) = \frac{2(R_i + v_i(t^* + mT))}{c} = \frac{2R_i}{c} + \frac{2v_i(t^* + mT)}{c} \tag{3.4}$$

The reflected/backscattered signal including the MIMO channel of the ith single point target is expressed in Equation (3.5) with respect to the transmitted signal $s(t)$,

$$\begin{aligned} r_i^{(l)}(t) &= \alpha_i e^{j\varphi_i^{(l)}} s(t^* + mT - \tau_i(m, t^*)) \\ &= \alpha_i e^{j\varphi_i^{(l)}} e^{j2\pi(f_0(t^* + mT - \tau_i(m,t^*)) + \frac{\mu(t^* + mT - \tau_i(m,t^*))^2}{2})} \end{aligned} \tag{3.5}$$

α is the reflected signal amplitude related to the RCS of the target, and the operator $e^{j\varphi_i^{(l)}}$ indicates the reflected signal phase delay with respect to the lth receiver in the virtual array discussed in the previous paragraphs. From the previous equation, the instantaneous frequency could be derived from the phase change shown below,

$$\begin{aligned} \frac{d\Phi}{dt} &= \frac{f_0(t^* + mT - \tau_i(m, t^*)) + \frac{\mu(t^* + mT - \tau_i(m,t^*))^2}{dt^*}}{dt^*} \\ &= f_0(1 - \frac{d\tau_i(m, t^*)}{dt^*}) + \mu(t^* - \tau_i(m, t^*))(1 - \frac{d\tau_i(m, t^*)}{dt^*}) \\ &\approx f_0 + \mu t^* \end{aligned} \tag{3.6}$$

The simplification of the term in the above equation is because of the short-range assumption $\tau_i^{(l)}(m, t^*) << T_0$ and $v_i << c$. So the phase delay of the lth receiver is formulated as:

$$\varphi_i^{(l)} = 2\pi(f_0 + \mu t^*)\frac{ld}{c} sin\theta_i \tag{3.7}$$

where l indicates the sequence of the receiver and d is the spacing distance between neighboring receivers in the virtual array.

By correlating the received signal with the conjugate copy of the transmitted signal, the received lth receiver de-chirped signal of the ith point scatterer is shown as follows:

$$\begin{aligned}
x_i^{(l)}(m,t^*) &= r_i^{(l)}(t) \times s^*(m,t^*) \\
&= \alpha_i e^{j\varphi_i^{(l)}} e^{j2\pi(f_0(t^*-\tau_i)+\frac{\mu(t^*-\tau_i)^2}{2})} \times e^{-j2\pi(f_0 t^* + \frac{\mu(t^*)^2}{2})} \\
&= \alpha_i e^{j\varphi_i^{(l)}} e^{j2\pi(f_0(t^*-\tau_i)+\frac{\mu(t^*-\tau_i)^2}{2}) - (f_0 t^* + \frac{\mu(t^*)^2}{2}))} \\
&= \alpha_i e^{j\varphi_i^{(l)}} e^{j2\pi(-f_0\tau_i + \frac{\mu}{2}\tau_i^2 - \mu t^* \tau_i)} \\
&\overset{(1)}{\approx} \alpha_i e^{j\varphi_i^{(l)}} e^{j2\pi(-f_0\tau_i - \mu t^* \tau_i)} \\
&= \alpha_i e^{j\varphi_i^{(l)}} e^{-j2\pi(f_0(\frac{2R_i}{c} + \frac{2v_i t^*}{c} + \frac{2v_i mT}{c}) + \mu t^*(\frac{2R_i}{c} + \frac{2v_i t^*}{c} + \frac{2v_i mT}{c}))} \\
&= \alpha_i e^{j\varphi_i^{(l)}} e^{-j2\pi(f_0\frac{2R_i}{c} + t^*(f_0\frac{2v_i}{c} + \mu\frac{2R_i}{c}) + f_0\frac{2v_i}{c}mT + \mu\frac{2v_i}{c}t^{*2} + \frac{2v_i}{c}mT\mu t^*)} \\
&\overset{(2)}{\approx} \alpha_i e^{j\varphi_i^{(l)}} e^{-j2\pi(\mu\frac{2R_i}{c}t^* + f_0\frac{2v_i}{c}mT + \frac{2v_i}{c}mT\mu t^*)} \\
&= \alpha_i e^{j2\pi(f_0+\mu t^*)\frac{ld}{c}sin\theta_i} e^{-j2\pi(\mu\frac{2R_i}{c}t^* + (f_0+\mu t^*)\frac{2v_i}{c}mT)} \\
&\overset{(3)}{\approx} \alpha_i * exp(j2\pi(f_0\frac{ld}{c}sin\theta_i)) * exp(-j2\pi(\mu\frac{2R_i}{c}t^*)) * exp(-j2\pi(f_0\frac{2v_i}{c}mT))
\end{aligned} \tag{3.8}$$

In the above derivation, some approximations are involved to simplify the computation under certain reasonable conditions or assumptions.

- (1): With the previous equation of the round-trip delay, it is notable that under a single chirp, the round-trip delay time is much smaller than the sampling time concerned the relatively much larger value of light speed in free space, which leads to the first approximation in the fifth line, namely: $\frac{\mu}{2}\tau_i^2 - \mu t^* \tau_i \overset{\tau \ll t^*}{\approx} -\mu t^* \tau_i$
- (2): In this step, $e^{-j2\pi f_0 \frac{2R_i}{c}}$ is constant, therefore it could be removed by merging with α_i. Then $\mu\frac{2v_i}{c}t^{*2}$ is neglected due to its much smaller value (t^{*2}) compared with other operators (t^*, mT). Lastly, $t^*(f_0\frac{2v_i}{c} + \mu\frac{2R_i}{c}) \approx t^*\mu\frac{2R_i}{c}$, as the Doppler frequency is negligible with respect to the beat frequency under the conditions of $f_0\frac{2v_i}{c} \ll \mu\frac{2R_i}{c}$, and $f_0\frac{2v_i}{cf_s} \ll \frac{Nyquistbound}{2}$, where f_s is the sampling frequency.
- (3): The assumption for computation simplification is that the automotive FMCW MIMO radar is a narrow-band radar, which means the bandwidth is much smaller than the center frequency, and there is no range and angle migration within the beat frequency signal.

After an analog-digital converter (ADC) with sampling frequency f_s, the analogous signal is discretized and shown below,

$$\begin{aligned}
&x_i^{(l)}(m,t^*) = \alpha_i * exp(j2\pi(f_0\frac{ld}{c}sin\theta_i)) * exp(-j2\pi(\mu\frac{2R_i}{c}t^*)) * exp(-j2\pi(f_0 * \frac{2v_i}{c}mT)) \\
&\overset{ADC(f_s)}{\Longrightarrow} x_i^{(l)}(m,k) = \alpha_i * exp(j2\pi(a(\theta_i)l) * exp(j2\pi(f_d(v_i)m)) * exp(j2\pi(f_r(R_i)k))
\end{aligned} \tag{3.9}$$

where

$$a(\theta_i) = f_0\frac{d}{c}sin\theta_i, f_d(v_i) = -f_0\frac{2v_i}{c}, f_r(R_i) = -\frac{\mu 2R_i}{cf_s}$$

where $k = fs * t^*$ is the index of fast-time samples (i.e., k = 0, 1, 2..., K − 1, and K is the total number of samples in one PRI).

For simplification of subsequent signal processing, the radar data is always reshaped into the radar cube matrix shown in Fig. 3.5. In this project, one radar cube contains a single frame of simulated radar data, where three axes are corresponding to the fast-time (K), slow-time (M), and number of channels

(L). Stacking the generated signal into matrix form from the aforementioned equation, the signal model could be written as:

$$\mathbf{X}_i = \alpha_i \mathbf{a}(\theta_i) \cdot \mathbf{f_d}(v_i) \cdot \mathbf{f_r}(R_i) \tag{3.10}$$

where:

$$\mathbf{a}(\theta_i) = [1, e^{j2\pi a(\theta_i)}, ..., e^{j2\pi a(\theta_i)(L-1)}]^T, \in \mathbb{C}^{L\times 1}$$
$$\mathbf{f_d}(v_i) = [1, e^{j2\pi f_d(v_i)}, ..., e^{j2\pi f_d(v_i)(M-1)}]^T, \in \mathbb{C}^{M\times 1}$$
$$\mathbf{f_r}(R_i) = [1, e^{j2\pi f_r(R_i),...,e^{j2\pi f_r(R_i)(K-1)}}]^T, \in \mathbb{C}^{K\times 1}$$

Therefore, the initial radar cube can be decomposed into three radar cube subsets that are only related to a single parameter with given values based on the above equation. It is notable that the sub-cube should have the same size and origin as the original radar cube, and each sub-cube should be homologous on the dimension of the corresponding aforementioned vector.

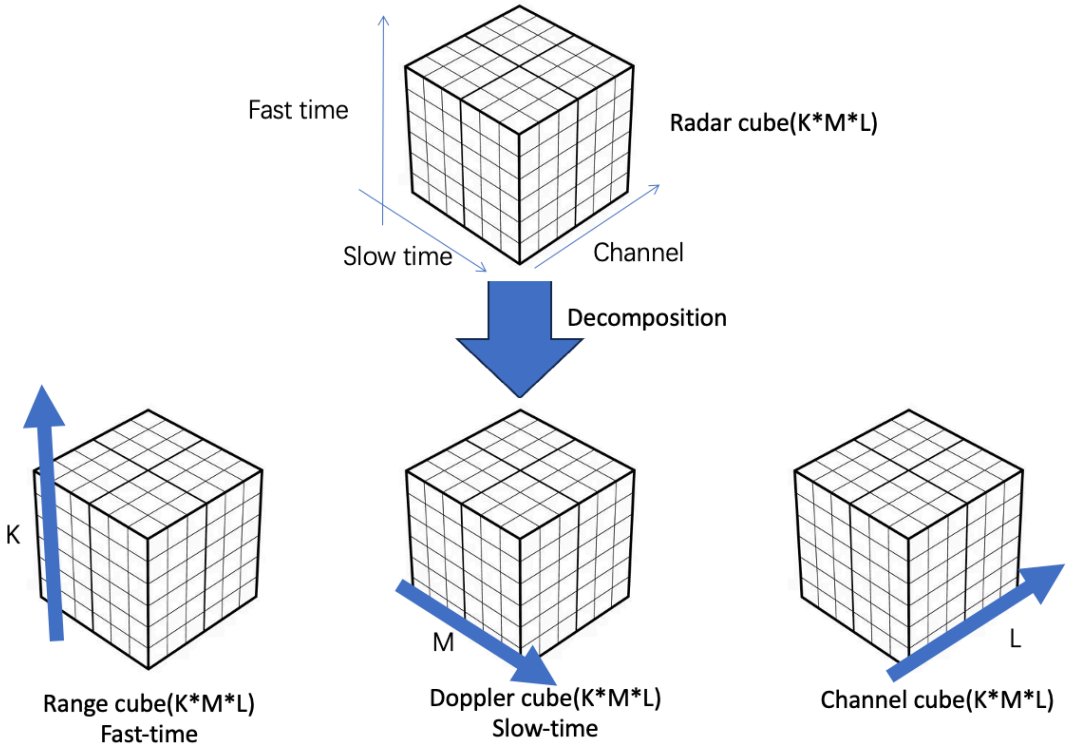

Figure 3.5: Illustration of the radar cube and decomposition along specific directions with their meaning, namely fast-time, slow-time, and number of MIMO channels

Then the received data of the f_nth frame in the presence of radar line of sight (LOS) with the Gaussian noise $\mathcal{N}$ is written as

$$\mathbf{Z}^{(f_n)} = \sum_{i=1}^{I} \mathbf{X}_i + \mathcal{N} \tag{3.11}$$

3.4. Target model

As one of the most important parts of the radar signal simulation, different possible approaches take a significant influence on the accuracy of the target model. As listed in the literature review, U.Chipengo[25] illustrated three main models for signal generation in this context. It is obvious that the primitive base model could simplify the computation in wave propagation by reducing the complexity in geometry. In contrast, high-fidelity physics-based models provide more accurate radar signals, especially for later target tracking and classification. However, heavy computation of wave propagation is required. In this part of the designed simulator, a realistic target model based on detailed CAD models which are

widely used in industrial design is proposed. Based on the CAD models, the grid of scattering points for the radar signals is generated and demonstrated in this section with examples of car(sedan) and human(pedestrian).

3.4.1. Scatter Model

It is important to note that the scatterers in the CAD models do not aim to precisely mimic electromagnetic scattering behavior from the actual objects. Rather, they serve as a representation of the object's body shape and extent, with denser scatterers located in the areas where more detailed physical structures are present in the objects. Figure 3.6, 3.7, shows the target model extracted from the 3D CAD model. Depending on the CAD source and the target's shape and complexity, the total number and distribution of extracted point scatters can be very different, therefore, pre-processing for scaling the target model is necessary to get an acceptable target size in terms of the considered scattering points. The sub-figures on the right-hand side below show the corrected point scatterers distribution.

Compared between models, the human model contains more scatterers concerned with the complexity of the human shape with its curved surfaces and body parts. As for the car and bus, their wheels contain more point scatterers compared to the flat surfaces of the chassis.

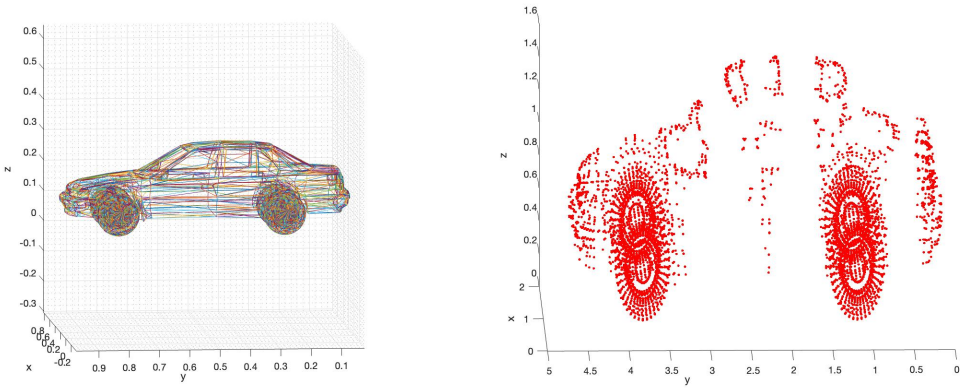

Figure 3.6: Car model used in the simulator

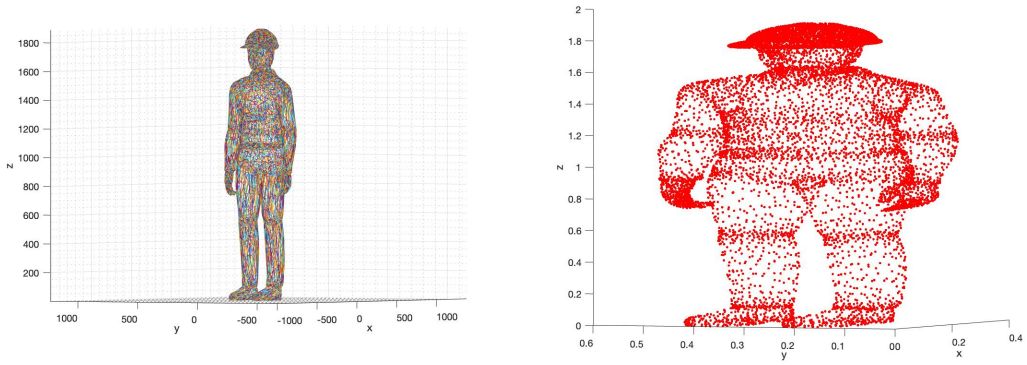

Figure 3.7: Man/pedestrian model used in the simulator

Radar Cross Section (RCS) In radar simulations, the RCS value is an important feature for target models that can significantly influence the resulting simulated signals. In this part, the RCS is specified according to the Swerling model, also known as fluctuation loss. For MIMO radar, the Swerling model influences the performance with respect to the DoA estimation [38].

Based on the general definition of the Swerling model, there are various types with different RCS definitions, namely Swerling model I, Swerling model II, Swerling model III, Swerling model IV, and Swerling model V (also known as Swerling model 0),

- Swerling model V (Swerling model 0): The RCS values of scatter points are constant at infinite degrees of freedom.
- Swerling model I: In this model, the RCS varies according to a chi-squared probability density function, with two degrees of freedom scan to scan. Specifically, in the proposed simulator, the RCS varies from frame to frame, as the frame is the common unit of data generated by current automotive radars.
- Swerling model II: It is similar to the Swerling model I, but with faster changes from pulse-to-pulse (chirp to chirp) with the same chi-squared probability density function with two degrees of freedom as the Swerling model I.
- Swerling model III: In this model, the RCS values change scan to scan as in the Swerling model I, but with a different chi-squared probability density function with four degrees of freedom.
- Swerling model IV: In this model, the RCS values have the same probability density function as in the Swerling model III, but with faster changes from pulse to pulse (chirp to chirp).

It needs to be outlined that in the following chapter 5, the Swerling model V (Swerling model 0) is selected in the simulation presented for feasibility, where all scatter points of the point clouds have identical values. A further improvement for the proposed simulator could be to investigate the influence of applying different Swerling models, and how to accurately estimate the RCS values for point clouds. Such modifications is expected to be not complicated, as it would only entail the modification of the intensity values from constant ones to those statistically drawn from a distribution.

3.4.2. Coordinate system

With the derived signal model and target model given in the previous sections, to accurately describe the space information for point scatterers, a 3D coordinate system is established shown in Fig.3.8 with an example of a single point target in the radar line-of-sight. To be more specific, the coordinate system is made of two parts, the world coordinates system and the radar observation system, where the blue labels are related to the parameter in the world coordinate system (XYZ-O) and black labels are related to the radar observation system (X'Y'Z'-O').

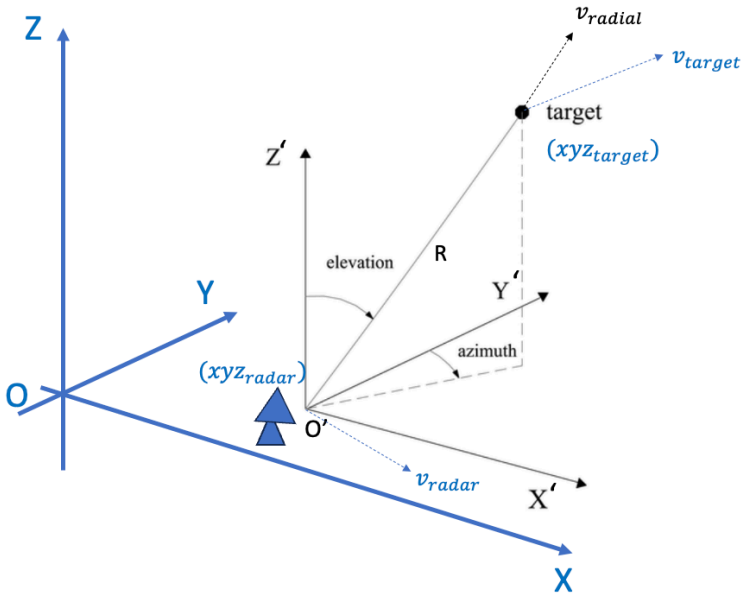

Figure 3.8: World coordinate systems and radar observation

The world coordinate system (3D Cartesian coordinate system) is the basis of the radar observation system which is used to generate the radial velocity (v_{radial}), range (R), and azimuth angle (θ_i) used in Equation (3.8).

With the known initial position of radar (xyz_{radar}) and single-point target (xyz_{target}), the range and azimuth angle between radar & target can be calculated with the below equation:

$$\begin{aligned} R &= ||xyz_{target} - xyz_{radar}|| \\ sin(\theta) &= (\frac{||x_{radar} - x_{target}||}{||xy_{radar} - xy_{target}||}) \end{aligned} \tag{3.12}$$

while the radial velocity (v_{radial}) can be calculated with projected v, the given velocity of radar (v_{radar}) and target (v_{target}) in world coordinates by using Equation (3.13).

$$\begin{aligned} v_{radial} &= |\frac{(v_{radar} - v_{target}) * x'y'z'_{target}}{||x'y'z'_{target}||^2} x'y'z'_{target}| \\ x'y'z'_{target} &= xyz_{target} - xyz_{radar} \end{aligned} \tag{3.13}$$

where $x'y'z'_{target}$ refers to the target position in the radar observation system.

However, to accurately describe the dynamic information of the target and the radar, the motion information is divided into two parts, translational motion, and rotational motion.

Translational motion: Within the measurement time (t), the target position would be changed in the world coordinate system based on the below equation:

$$xyz_{translation}(t) = v_{translantion}(t) * t + xyz_{target}(t = 0) \tag{3.14}$$

Rotational motion: Compared with translational motion, rotational motion is more complex due to an extra rotation coordinate system involved. For simplification, the sphere coordinate is introduced to define the rotational motion shown in Fig.3.9.

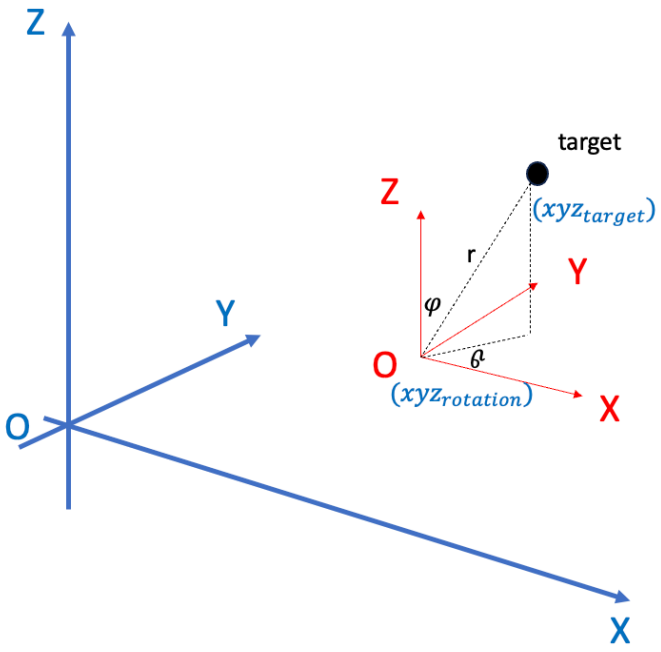

Figure 3.9: Rotational motion coordinate system

With set rotation center ($xyz_{rotation}$), rotation direction (ϑ, φ), and rotation speed(ω), the target position can be calculated using the equations below:

$$\begin{aligned} xyz_r &= ||xyz_{target} - xyz_{rotation}|| \\ u_{xyz} &= [sin\varphi cos\vartheta, sin\varphi sin\vartheta, cos\varphi]^T \\ \theta_{rotation}(t) &= \omega * t \\ xyz_{afterrotation}(t) &= xyz_{target} + rm(t) * xyz_r \end{aligned} \tag{3.15}$$

where xyz_r refers to the target coordinate in the rotation coordinate system, u_{xyz} represents the unit rotation direction vector ($u_x^2 + u_y^2 + u_z^2 = 1$) according to the Right-hand rule, and the rm is the rotation matrix defined as follows by substituting $\theta = \theta_{rotation}(t)$

$$rm(t) = \begin{bmatrix} cos\theta - u_x^2\ (1 - cos\theta) & u_x\ u_y\ (1 - cos\theta) - u_z\ sin\theta & u_x\ u_z\ (1 - cos\theta) + u_y\ sin\theta \\ u_y\ u_x\ (1 - cos\theta) + u_z\ sin\theta & cos\theta - u_y^2\ (1 - cos\theta) & u_y\ u_z\ (1 - cos\theta) - u_x\ sin\theta \\ u_z\ u_x\ (1 - cos\theta) - u_y\ sin\theta & u_z\ u_y\ (1 - cos\theta) + u_x\ sin\theta & cos\theta - u_z^2\ (1 - cos\theta) \end{bmatrix} \tag{3.16}$$

Meanwhile, the instant linear velocity in the world coordinate system would be:

$$v_{linear}(t) = (\omega \dot{u}_{xyz}) \times rm(t) * xyz_r \tag{3.17}$$

where $(\omega \dot{u}_{xyz})$ is the angular velocity in vector form.

Therefore, for the single-point scatter shown in Fig.3.9, the instant position and radial velocity are the combined translational motion and rotational motion together shown in the equation below:

$$\begin{aligned} xyz_{target}(t) &= xyz_{translational}(t) + xyz_{afterrotation}(t) + xyz_{target}(t = 0) \\ v_{radial}(t) &= v_{translation}(t) + v_{linear}(t) + v_{radial}(t = 0) \end{aligned} \tag{3.18}$$

3.5. Propagation model

As discussed before, only line-of-sight targets (point scatterers) are considered in the radar signal simulation in this project. Therefore, the shadowed/occluded part of the targets needs to be filtered out and eliminated before the final signal generation.

3.5.1. Shadowing estimation

To accurately estimate the hidden points with respect to the radar line-of-sight, a hidden point removal algorithm is applied based on the research of S. Katz[39],[28]. In MATLAB, a function has already been published and testified by M. Moore according to his paper for simulating Micro-Doppler information of unmanned aerial vehicles (UAV) with dynamic point clouds.

Figure.3.10 shows the implementation of the hidden point removal (HPR) algorithm with an example of the sphere in 3D space. As shown in the figure, after being filtered with the HPR algorithm, observing from the red star point considered to be the radar, only the points marked by the 'X' are visible.

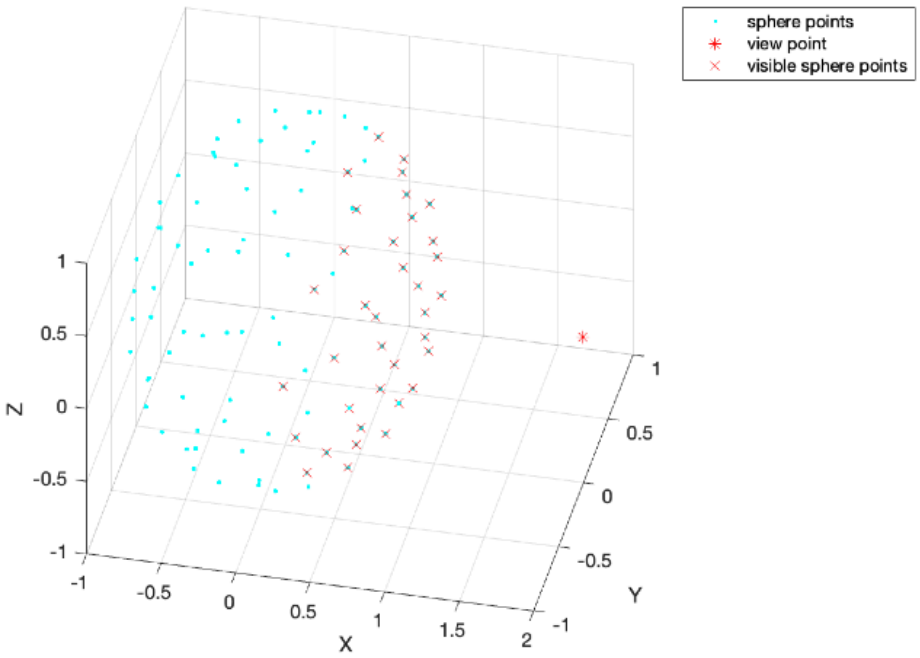

Figure 3.10: Illustration of hidden point removal algorithm applied in the proposed simulator, where out of the whole cloud of points belonging to a sphere object, only those marked by 'X' are visible to the radar located in the view point

Summarizing this chapter, with preset motion information for each target model and with user-defined radar parameters, the proposed simulator can generate simulated radar signals and signatures with and without the HPR algorithm to model occlusion/shadowing. This algorithm uses the ground truth information from the original CAD models in every frame to mark only a subset of points to be the actual radar scatter points for further processing.

4

Implementation Details

In this chapter, several radar signal processing techniques such as Fast Fourier Transform, and Direction of Arrival (DoA) estimation are introduced. These are then applied to the simulated radar signals and signatures to evaluate the performance of the simulator developed in this work. The actual results will be shown in the next chapter, while the following content describes their derivation based on the signal model introduced in the previous chapter.

4.1. Fast Fourier Transform (FFT) algorithm

As one of the fundamental techniques for radar signal processing, the FFT (Fast Fourier Transform) algorithm is widely used to estimate the targets' range, velocity, and angle with respect to the radar. It is particularly effective in radar systems that use Linear Frequency Modulated Continuous Wave (LFMCW) or Frequency Modulated Continuous Wave (FMCW) waveforms due to the inherent characteristics of these waveforms. Depending on the application in radar signal processing, range-Doppler image, range-azimuth (cross-range) image, and Doppler-azimuth (cross-range) image could be plotted by using multi-dimensional FFT.

Specifically, the range-Doppler image could be generated by applying the 1D FFT algorithm on the fast-time domain (range) and then another 1D FFT on the slow-time domain (Doppler). Similarly, the range-azimuth image could be derived by changing the second 1D FFT on the azimuth domain (which is referred to as the channel domain in the previous chapters). As for the Doppler-azimuth image, It could be derived from applying a third 1D FFT on the Doppler domain of range-azimuth, or channel domain of range-Doppler.

Back to the theoretical derivation, the mathematical equation of the introduced signal with respect to the ith scatter point in the previous chapter is shown below:

$$\begin{aligned} x_i^{(l)}(m,k) &= \alpha_i * exp(j2\pi(a(\theta_i)l) * exp(j2\pi(f_d(v_i)m)) * exp(j2\pi(f_r(R_i)k)) \\ where, a(\theta_i) &= f_0\frac{d}{c}sin\theta_i, f_d(v_i) = -f_0\frac{2v_i}{c}, f_r(R_i) = -\frac{\mu 2R_i}{cf_s} \end{aligned} \tag{4.1}$$

Therefore, the de-chirped received signal in one frame for all targets is:

$$\mathbf{y}_m^{(l)}(k) = \sum_{i=1}^{I} x_i^{(l)}(m,k) + \mathcal{N} \tag{4.2}$$

where $\mathcal{N}$ is the additive Gaussian noise.

After applying 1D FFT on the fast-time domain with sample number N on the signal, the signal model $\mathbf{Y}(n)$ of the nth range cell can be written as:

$$\mathbf{Y}_m^{(l)}(n) = \begin{cases} \sum_{k=1}^{K} y_m^{(l)}(k) * e^{-j2\pi(\frac{(n-1)(k-1)}{N})} & n \in [1, K] \\ 0 & n \in [K+1, N] \end{cases} \tag{4.3}$$

where $n \in [1, N], k \in [1, N]$.

Similarly, by applying another 1D FFT on the slow-time domain and azimuth (channel) domain with sample numbers P and Q respectively, the signal model $\mathbf{Y}_p^{(l)}(n)$ and $\mathbf{Y}_m^{(q)}(n)$ are defined as:

$$\begin{aligned} \mathbf{Y}_p^{(l)}(n) &= \begin{cases} \sum_{m=1}^{M} \mathbf{Y}_m^{(l)}(n) * e^{-j2\pi(\frac{(p-1)(m-1)}{P})} & p \in [1, M] \\ 0 & p \in [M+1, P] \end{cases} \\ \mathbf{Y}_m^{(q)}(n) &= \begin{cases} \sum_{l=1}^{L} \mathbf{Y}_m^{(l)}(n) * e^{-j2\pi(\frac{(q-1)(l-1)}{Q})} & p \in [1, L] \\ 0 & p \in [L+1, Q] \end{cases} \end{aligned} \tag{4.4}$$

Lastly, with proper FFT sample numbers, the signal after applied 3D FFT to the radar cube is shown below:

$$\mathbf{Y}_p^{(q)}(n) = \sum_{k=1}^{K} \sum_{m=1}^{M} \sum_{l=1}^{L} \mathbf{Y}_m^{(l)}(k) * e^{-j2\pi(\frac{(q-1)(l-1)}{Q})} * e^{-j2\pi(\frac{(p-1)(m-1)}{P})} * e^{-j2\pi(\frac{(n-1)(k-1)}{N})} \tag{4.5}$$

In general, for a conventional 3D radar cube as the one mentioned in the previous chapter, the target features of range, velocity, and angle with respect to the radar, including their elevation-azimuth coupling information, could be extracted from raw data intuitively after applying multi-dimensional FFT, shown in Fig. 4.1.

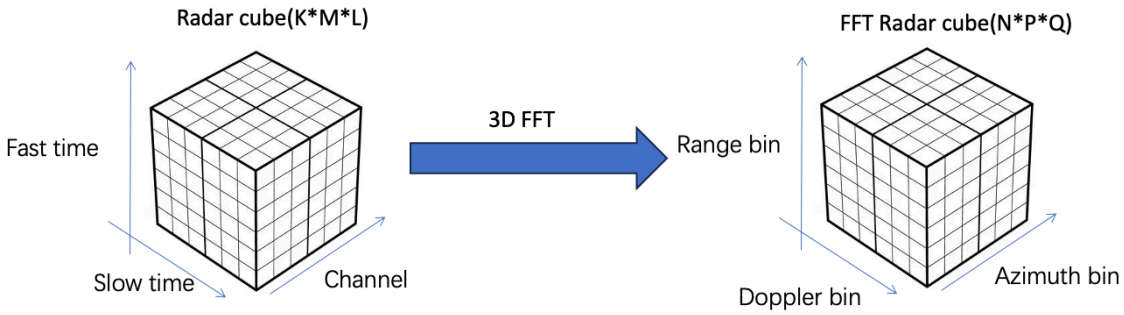

Figure 4.1: Illustration of the 3D FFT radar cube in MIMO FMCW radar

4.2. Direction of Arrival (DoA) estimation

As one of the key advantages of Multiple-Input Multiple-Output (MIMO) radar systems compared with traditional single-antenna radar systems, Direction of Arrival (DOA) estimation techniques had been deeply studied, even if ongoing research is still active to find new methods to improve angular resolution. With simple 2D FFT on the radar data, DOA estimation could be realized by detecting peaks on range-azimuth images, i.e., finding the maximum magnitude Doppler bins (m) of $|\mathbf{Y}_m^{(q)}(n)|$. However, sometimes due to the limitation of conventional angular resolution, enhanced DOA estimation algorithms are applied to improve the performance of the results for the classification of closely-spaced targets.

Three commonly used enhanced DOA estimation algorithms, namely Beamscan, Capon[40], and Multiple Signal Classifier (MUSIC)[41], are introduced as follows, with the rewritten signal model related to the steering vector (azimuth) from Equation (3.10) with respect to the sample time index K, and array elements L:

$$\mathbf{X}(k) = \mathbf{a}(\theta_i) \cdot \mathbf{x}(k) + \mathcal{N} \tag{4.6}$$

4.2.1. Beamscan

Beamscan, also known as conventional beamforming or delay-and-sum beamforming is a fundamental technique used in array signal processing to focus the sensitivity of an antenna array in a specific direction while attenuating signals arriving from other directions.

With known received signal $\mathbf{X}(k)$, a weight related to all possible angles of arrival (steering vector) is added and denoted as $\mathbf{w}$. Therefore the output mean power of the beamformer is:

$$\begin{aligned} P(\theta) &= \mathbb{E}[|\mathbf{w}^H \cdot \mathbf{X}(k)|^2] \\ &= \mathbf{w}^H E[\mathbf{X}(k)^H \mathbf{X}(k)]\mathbf{w} \\ &= \mathbf{w}^H * \mathbf{R} * \mathbf{w} \end{aligned} \tag{4.7}$$

where R is the spatial correlation matrix of the received signal.
From Equation (4.6), when the direction of arrival is equal to θ_i, the mean power in Equation (4.7) reached to maximum by substituting all possible angle $\mathbf{a}(\theta)$ for $\mathbf{w}$.

Thus, the arrival angles θ are determined by evaluating the power peaks:

$$P_{beamscan} = \mathbf{a}(\theta)^H * R * \mathbf{a}(\theta) \tag{4.8}$$

4.2.2. CAPON

CAPON, also known as Minimum Variance (MV) beamforming, is more advanced than simple beamscan method. Instead of detecting the peak of the output power as beamscan, Capon approach aims to minimize the variance of the estimated output power by constraining the beamformer gain to be 1 .

Therefore, the mathematical derivation of the Capon is:

$$\begin{aligned} &\min_{\mathbf{w}} \mathbf{w}^H * \mathbf{R} * \mathbf{w}, \\ &set\ \mathbf{w}^H \mathbf{a}(\theta) = 1, \\ &P_{capon} = \frac{1}{\mathbf{a}(\theta)^H * \mathbf{R}^{-1} * \mathbf{a}(\theta)} \end{aligned} \tag{4.9}$$

4.2.3. Multiple Signal Classifier (MUSIC)

Multiple Signal Classifier (MUSIC), is an advanced beamforming technique using the special property between steering vectors and noise, i.e., that the steering vector, as the subspace of signal, is orthogonal to the noise subspace.

Therefore, the value of $P_{MUSIC}(\theta)$ implies a relatively large value when angle θ is equal to the DoA related to one of the signals. The definition of $P_{MUSIC}(\theta)$ is shown below:

$$P_{MUSIC}(\theta) = \frac{1}{\mathbf{a}(\theta)^H \mathbf{Q}_n \mathbf{Q}_n^H \mathbf{a}(\theta)} \tag{4.10}$$

where $\mathbf{Q}_n$ refers to the noise subspace matrix.

5

Simulated Results and Analysis

In this chapter, all the representative results for simulated signals based on different target models and scenarios are presented. Specifically, the simulations are presented in two parts, one showing a simpler scene with one single target, and one part with multiple targets. The simulated results contain the ground truth of the target, range-azimuth images, and range-Doppler map(only for the moving targets). Prior to showing the results, the radar settings for the simulation are shown in the following Table 5.1.

Table 5.1: Simulated radar parameters for the presented simulations in this chapter

Center Frequency(Fc)	77GHz	Radar position	(0,0,0.5)	System Noise(wgn)	3dB
Bandwidth(B)	1GHz	Sampling Frequency(Fs)	12.8MHz	Range resolution	0.15m
Chirp Time(Tc)	20us	Frame sample time	0.5s	Max unambiguous range	38.4m
Number of transmitter antenna(nTx)	3	Signal Channel	12	Velocity resolution	0.3805m/s
Number of receiver antenna(nRx)	4	Radar velocity	(0,0,0)	Max unambiguous velocity	48.703m/s

5.1. Single target scenes

In this section, there are three parts involving multiple different target models including the car model and pedestrian model mentioned in 3. Simulated results without and with the HPR algorithm are listed to evaluate the simulator performance with different DoA estimation algorithms. Figure.5.1 shows an example of the single-target simulation ground truth in the world coordinate system.

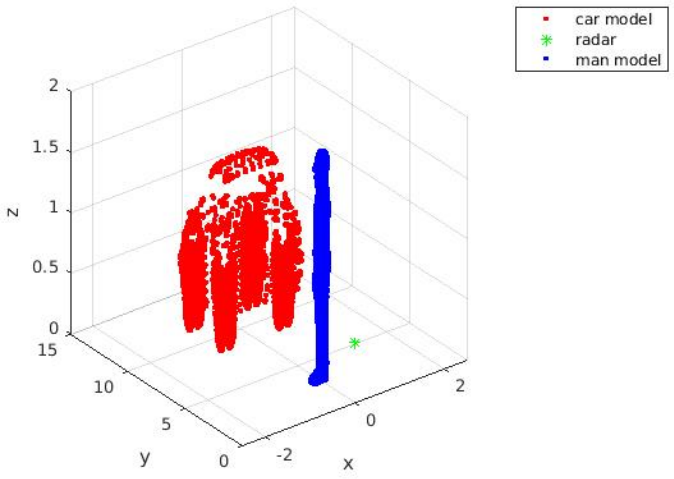

Figure 5.1: Target position with respect to radar in world coordinates(meter), 3D example visualization with car and pedestrian

5.1.1. Man model simulation

Applying the man model shown in Fig. 5.1, the target man is located in front of the radar, where the human body center is at (0,3,0) in world coordinates, which means the distance is 3m between human standing position and radar position on ground (xy-plane). The man model is about 1.8m high, while the radar is lifted to the height of 0.5m to simulate the real case, mounted on the car's front bumper. The radar signal is generated under a static state, where the heading direction of the pedestrian is changed in each simulation.

In Fig. 5.2, the visible scattering points after the application of the HPR algorithm are marked on the previously-shown frames for demonstration where the different headings of the target in the 3D Cartesian space can be seen as well. It should be noted that these are the only points that will be considered as actual scattering points of the targets for the radar simulator, essentially excluding those that are occluded by other points with respect to the radar line of sight, and the RCS value for all the point scatters in the target model is identical, default setting as 1. The following sub-figures in Fig.5.3 then show the range-azimuth images generated by applying different imaging algorithms such as 2D FFT, beamscan, capon and MUSIC. These algorithms are applied on a frame-by-frame basis, essentially mimicking what would happen in an experimental automotive radar producing a stream of frames.

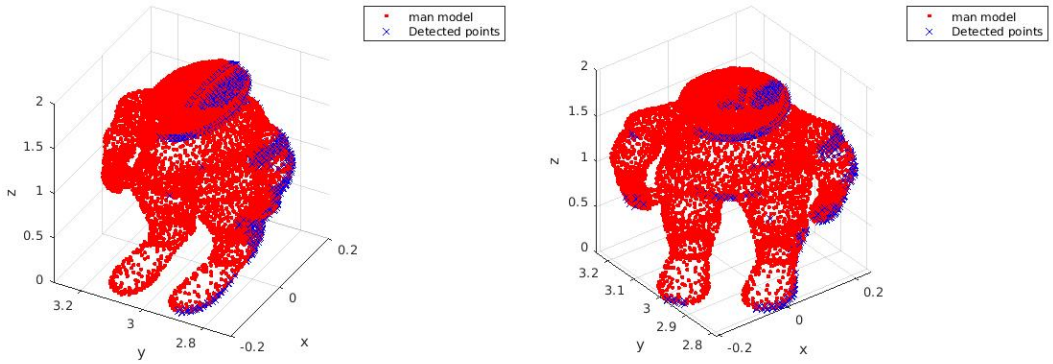

(a) Heading to -x direction

(b) Heading to -x-y direction

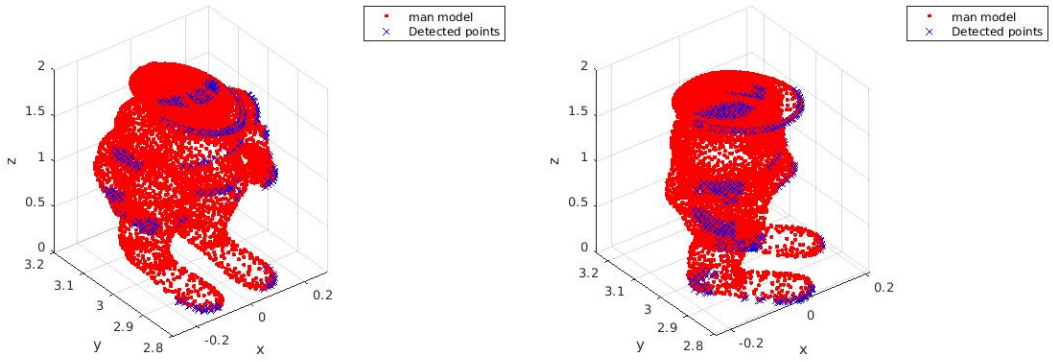

(c) Heading to -y direction

(d) Heading to -yx direction

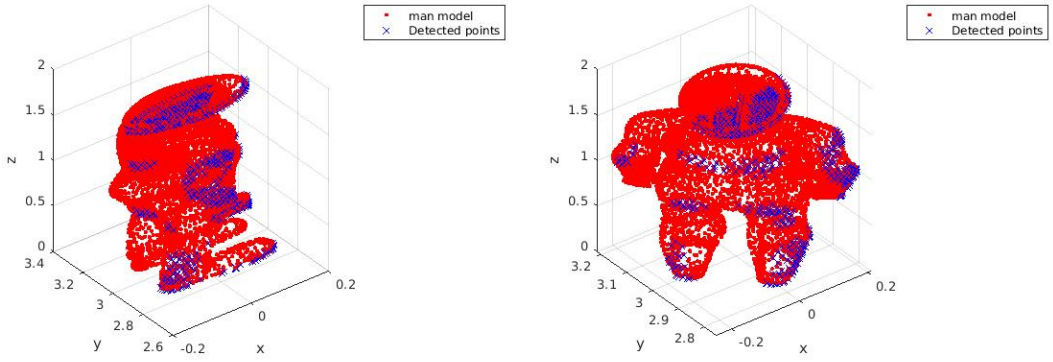

(e) Heading to x direction

(f) Heading to xy direction

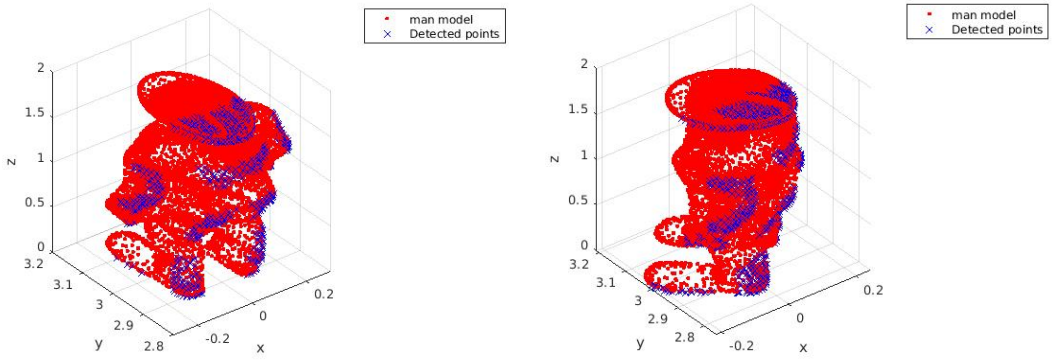

(g) Heading to y direction

(h) Heading to -xy direction

Figure 5.2: Visible points used as scattering target points for the radar signal after the application of the HPR algorithm. The frames represent the man/pedestrian model with different headings considered as an example in this section.

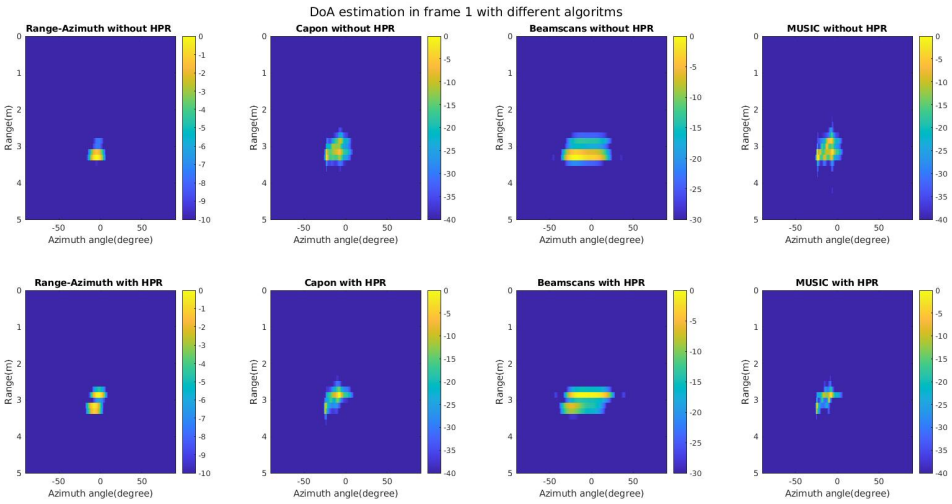

(a) Heading to -x direction

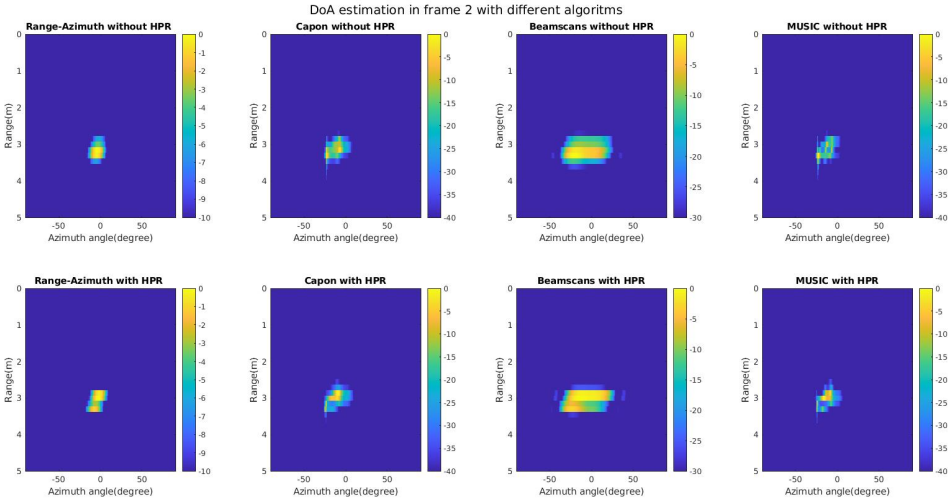

(b) Heading to -x-y direction

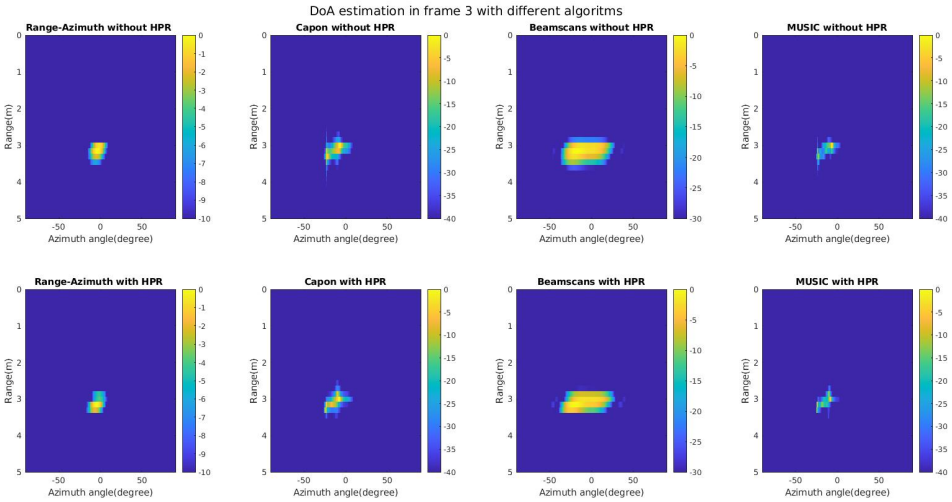

(c) Heading to -y direction

Figure 5.3: Range-azimuth figures generated for different heading directions for the man model and by applying imaging algorithms (i.e., by columns left to right simple range-azimuth, Capon, beamscan, MUSIC)

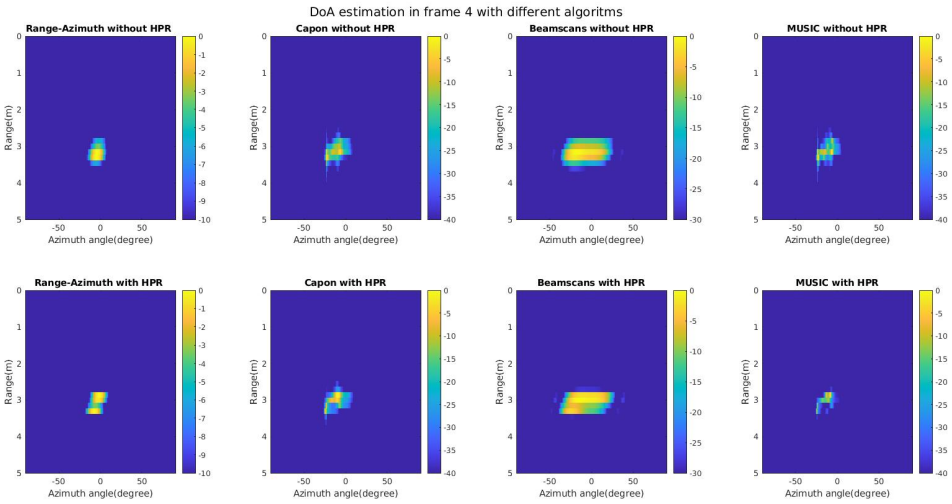

(d) Heading to -yx direction

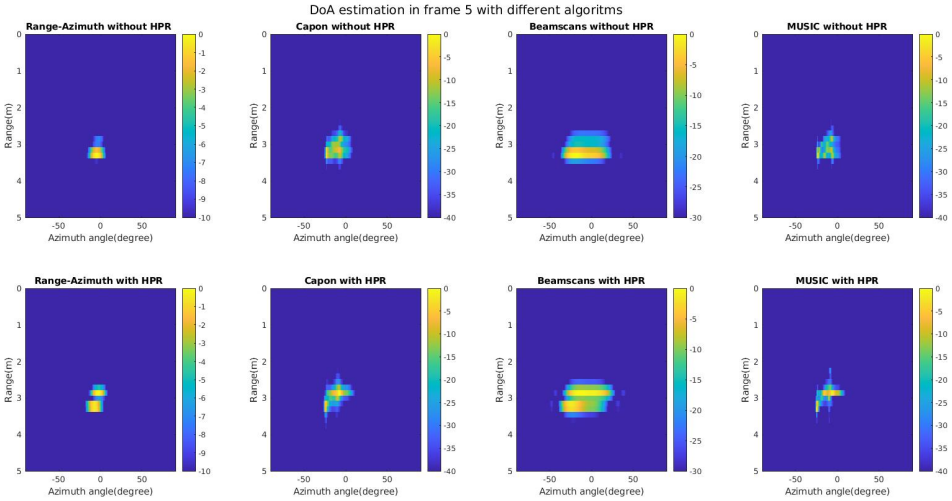

(e) Heading to x direction

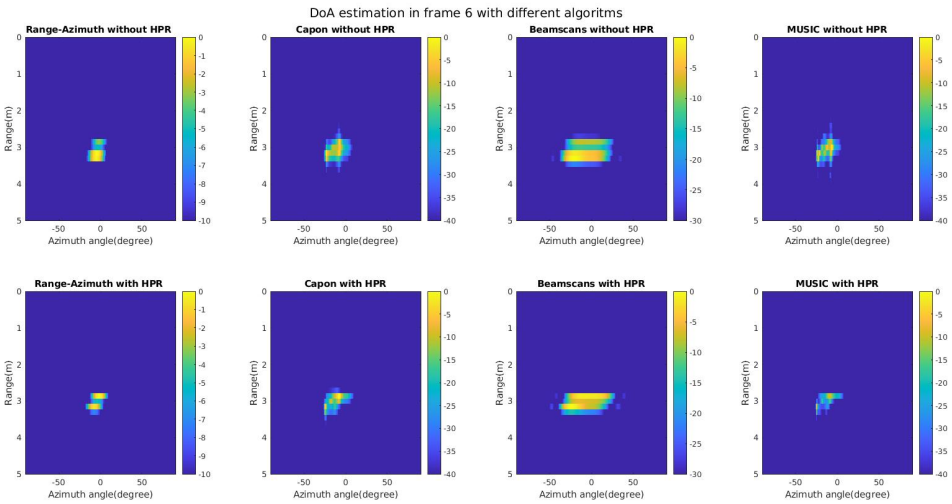

(f) Heading to xy direction

Figure 5.3: Range-azimuth figures generated for different heading directions for the man model and by applying imaging algorithms (i.e., by columns left to right simple range-azimuth, Capon, beamscan, MUSIC)

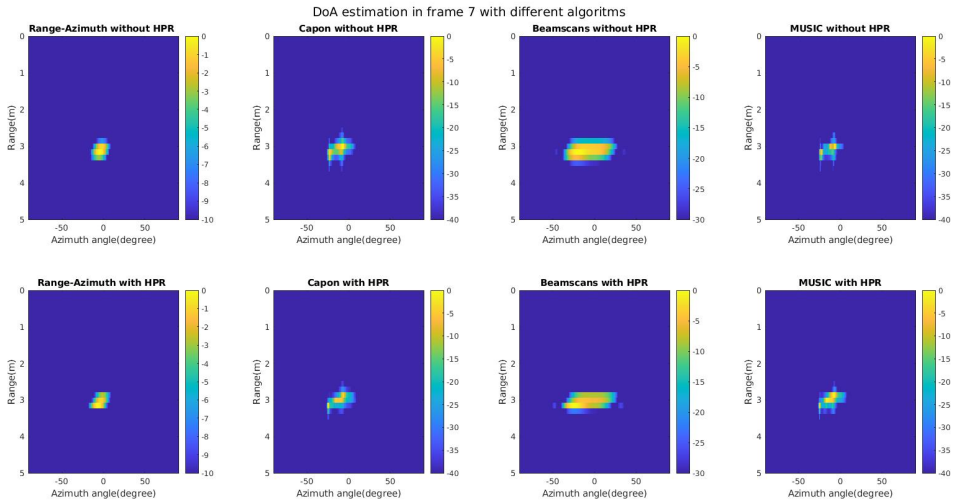

(g) Heading to y direction

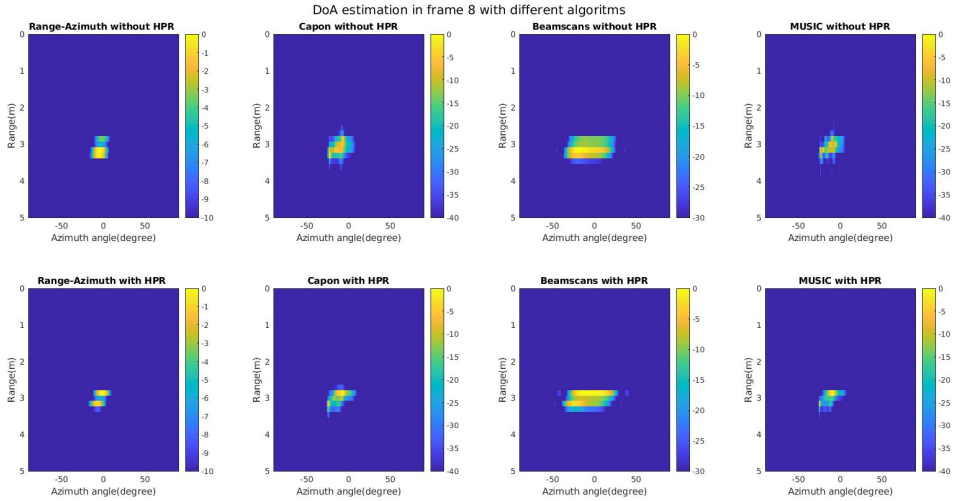

(h) Heading to -xy direction

Figure 5.3: Range-azimuth figures generated for different heading directions for the man model and by applying imaging algorithms (i.e., by columns left to right simple range-azimuth (2D-FFT), Capon, beamscan, MUSIC)

Through the results shown in Fig.5.3, under different head directions, except when the pedestrian facing to -y direction and y direction, an extra highlighted point-like signal distributed on another range bin could be observed in the simulated results applied HPR algorithm. This finding is caused by change the distribution of scattered points after shadowed points are removed. Without HPR algorithm, the point clouds of the target are concentrated distributed, which leads to a single strong point-like signal in the range-azimuth image. Therefore, there is no possibility to distinguish the heading direction of the pedestrian.

Another insightful observation is that the range-azimuth figures generated with Capon and MUSIC has a relative clearly view among all the results, more centralized power distribution. Comparing the performance of the MUSIC and Capon algorithms with that of the Beamscan method, and 2D-FFT method. The former two techniques exhibit superior resolution capabilities, evidenced by their ability to delineate targets with more distinct contours and enhanced separation within the human model, i.e. its distinct body parts. Furthermore, the images derived from diverse frames exhibit distinct characteristics, such as varying peak distributions. This proves that the frame generator operates in accordance with

its intended functionality, effectively capturing different aspects of the scene across frames.

5.1.2. Car model simulation

Similar to the simulated setting mentioned in the pedestrian model, however, the car model center is placed at (0,10,0), 10 meters away from the radar on the ground, concerned with the length of the car model, to avoid car collision in the real world. The radar signal is simulated under a static state as well but changing the car heading directions with identical RCS value for all the scatter point. Figure.5.4 gives the visualization of simulation top view ground truth including detected points distribution filtered by HPR algorithm in different frames which is corresponding to one heading direction starting from positive y direction.

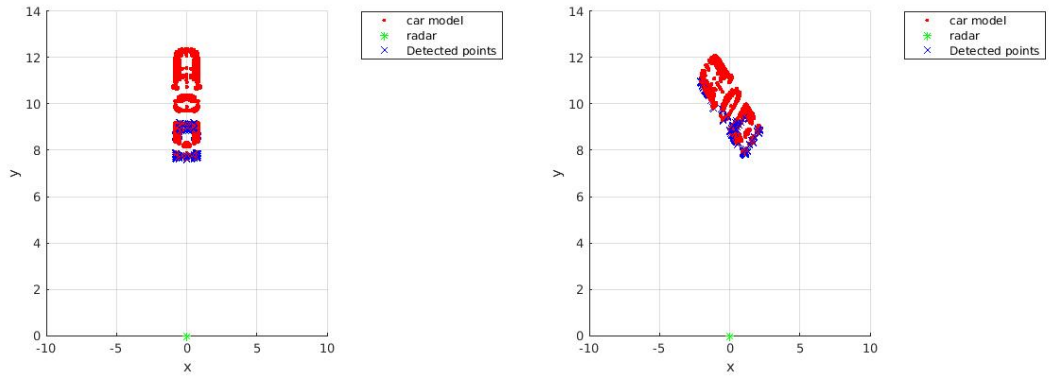

(a) Heading to y direction

(b) Heading to -xy direction

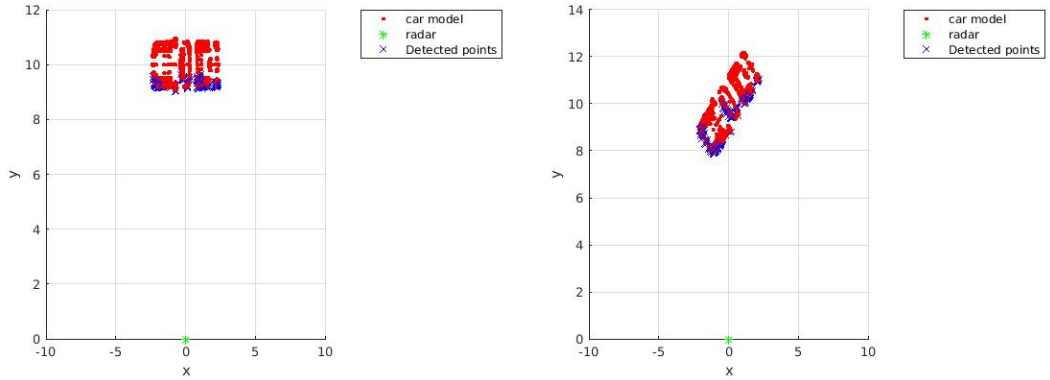

(c) Heading to -y direction

(d) Heading to -x-y direction

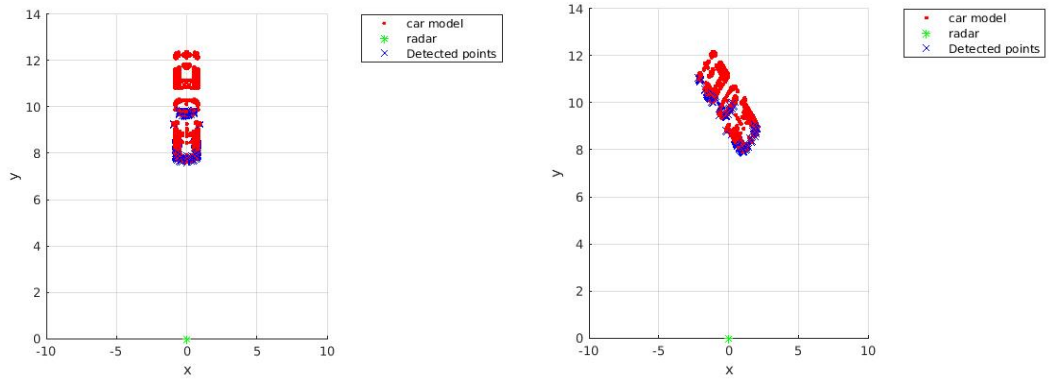

(e) Heading to -y direction

(f) Heading to x-y direction

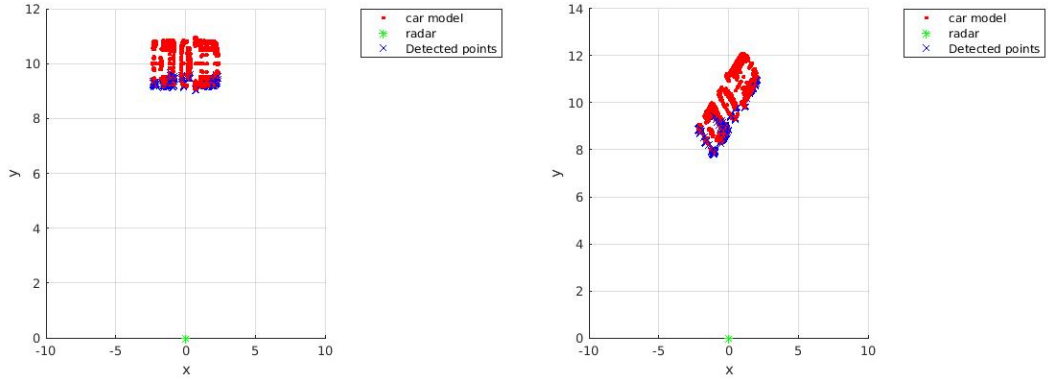

(g) Heading to x direction

(h) Heading to xy direction

Figure 5.4: Visible points used as scattering target points for the radar signal after the application of the HPR algorithm. The frames represent the car model with different headings considered as an example in this section.

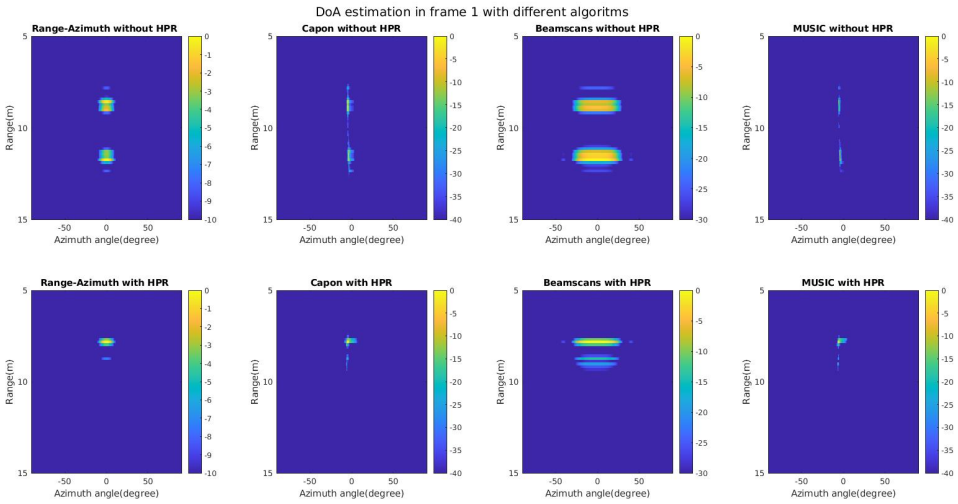

(a) Heading to y direction

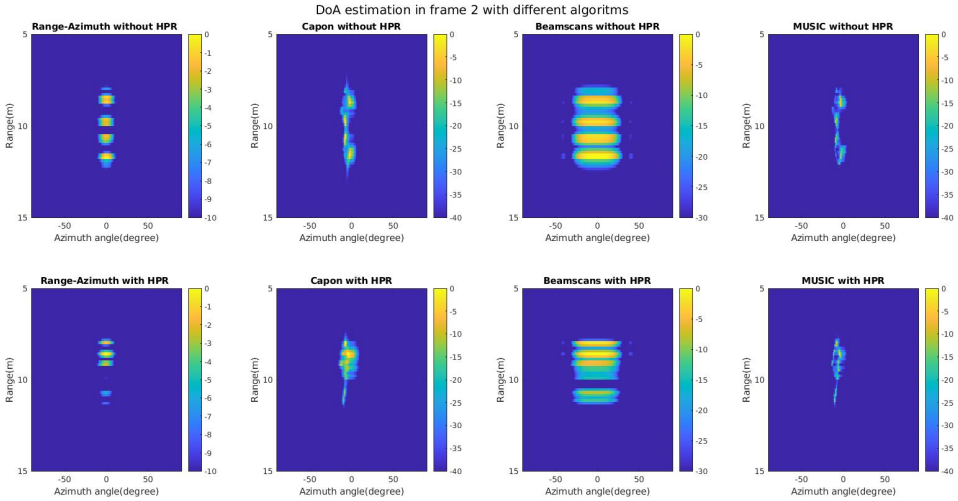

(b) Heading to -xy direction

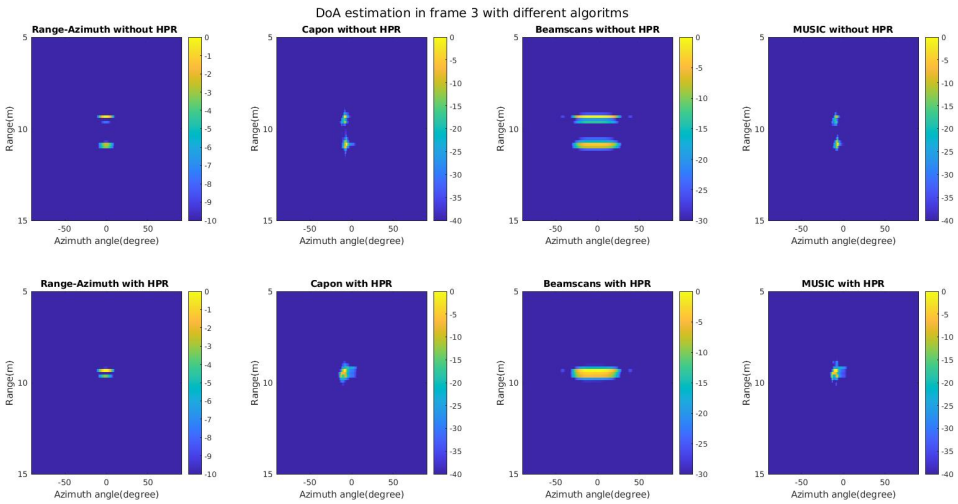

(c) Heading to -x direction

Figure 5.5: Range-azimuth figures generated for different heading directions for the car model and by applying imaging algorithms (i.e., by columns left to right simple range-azimuth(2D-FFT), Capon, Beamscan, MUSIC)

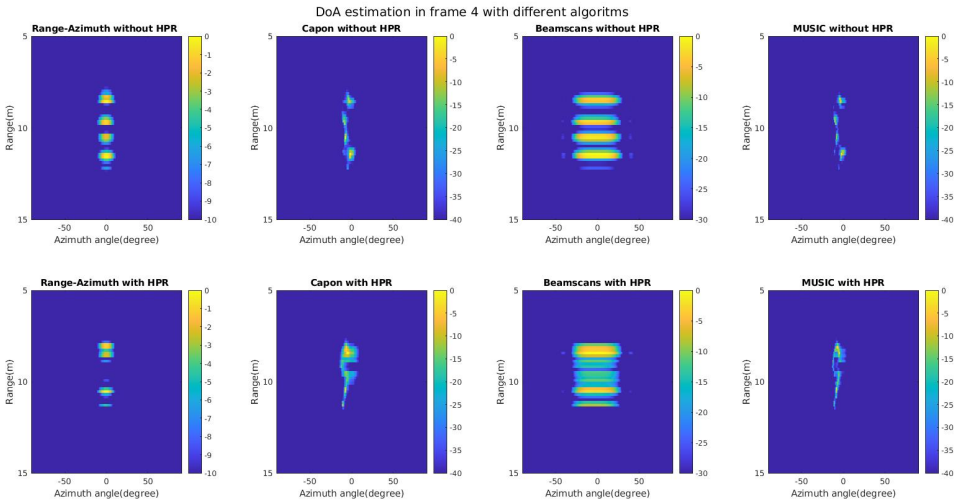

(d) Heading to -x-y direction

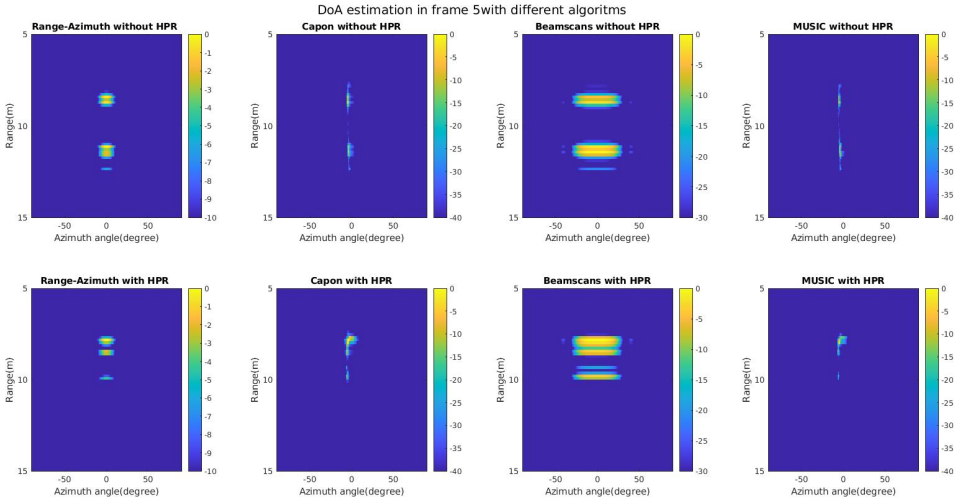

(e) Heading to -y direction

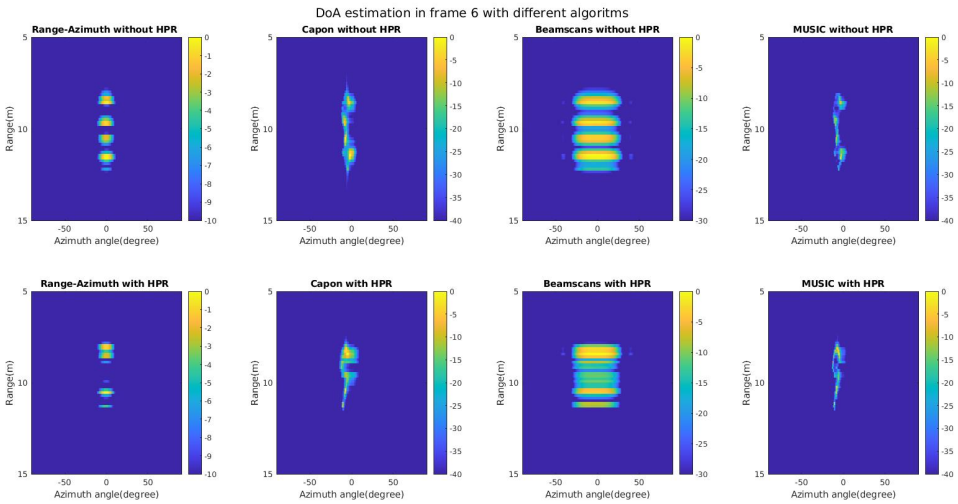

(f) Heading to xy direction

Figure 5.5: Range-azimuth figures generated for different heading directions for the car model and by applying imaging algorithms (i.e., by columns left to right simple range-azimuth, Capon, beamscan, MUSIC)

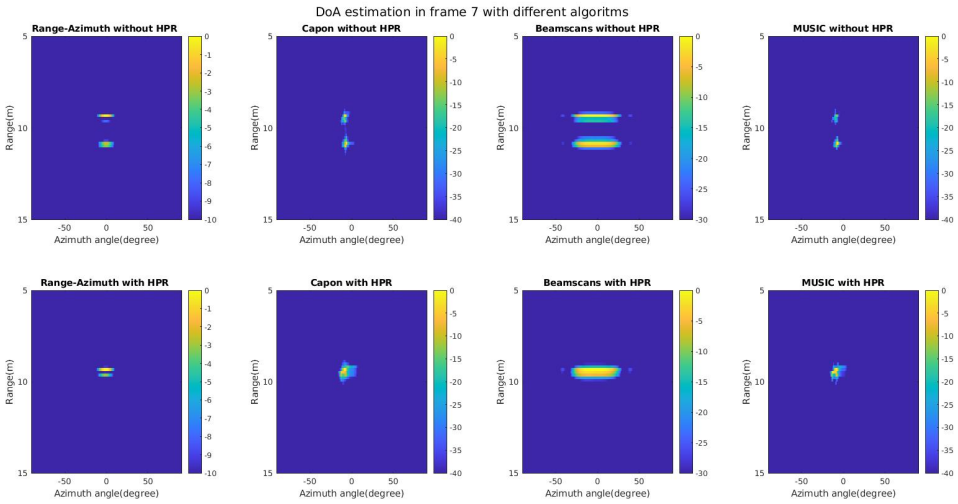

(g) Heading to y direction

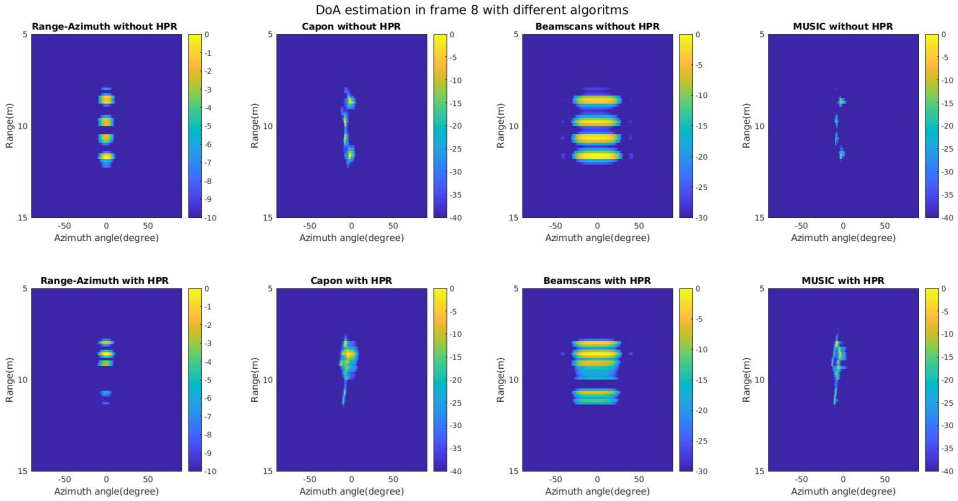

(h) Heading to -xy direction

Figure 5.5: Range-azimuth figures generated for different heading directions for the car model and by applying imaging algorithms (i.e., by columns left to right simple range-azimuth(2D-FFt), Capon, beamscan, MUSIC)

Comparing the different results shown in the previous figures, it is clear that the HPR algorithm has better performance on the car model, concerning the target shape influence of the HPR algorithm.

Another valuable observation is that the simulated signals in range-azimuth images are highly similar with respect to two pairs of heading directions, (xy,x-y,-x-y,-xy) and (-x,x). The HPR algorithm only affected the energy distribution due to the eliminated shadow points, but did not affect the similarity of the target shape. However, for y, and -y heading direction, the simulated results are the same without removed hidden points, but still they show some difference after the application of the HPR algorithm.

More importantly, with the HPR algorithm, the simulated results became more realistic, especially for car models, as the shadowed/occluded parts are eliminated under different cases (different heading direction).

5.1.3. Different car types' simulation

In this section, additional two car models, the F1 racing car model (McLaren MP4/4,1988) and the Ferrari car model (Ferrari concept car) are applied to the simulator with the same settings as the car model mentioned before. The simulation is simplified to five heading direction concerned conclusion from single car model Another noticeable condition for different car type simulation is that, to keep the simulation academic, all the car models are scaled down the point scatters to a constant by random selection from original point clouds. Figure 5.6, 5.8, 5.10, 5.12, 5.14 are the top view ground truth of the models' position with respect to the radar location, whereas Fig.5.7, 5.9, 5.11, 5.13, 5.15 is the corresponding range-azimuth images based on the simulated data generated by the proposed simulator.

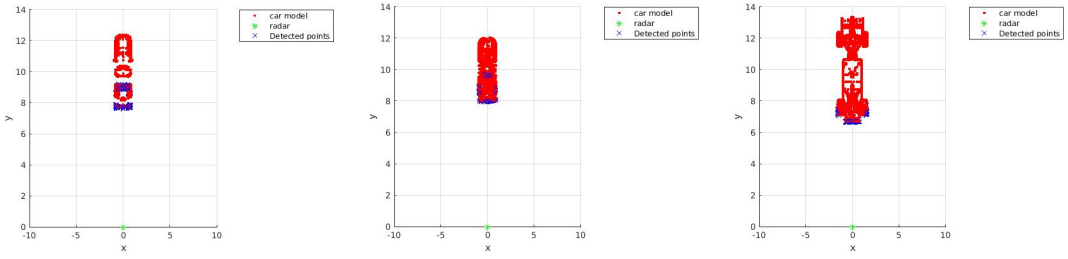

(a) Car model **(b)** Ferrari model **(c)** F1 model

Figure 5.6: Ground Truth of different car models from top view with detected points illustration of heading to y direction

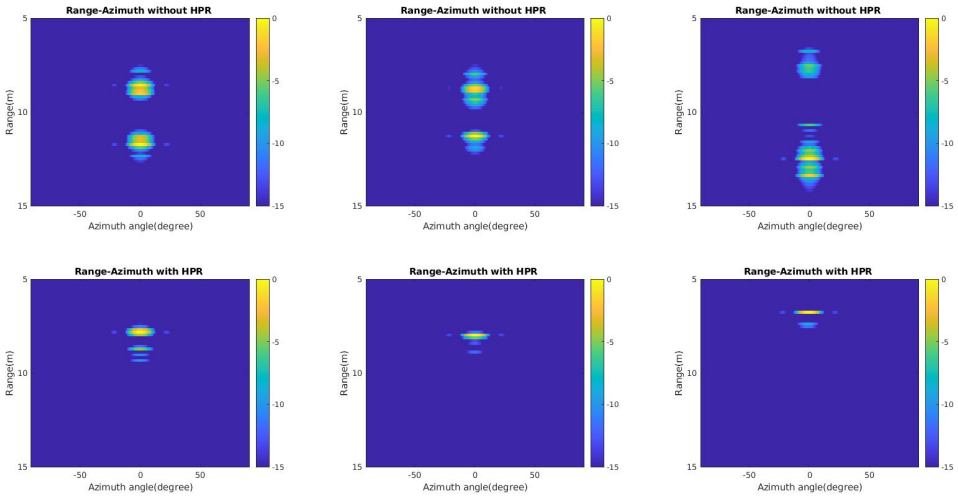

Figure 5.7: Simulated range-azimuth images of the car models shown in the previous figure without (top row) and with (bottom row) HPR algorithm to model occlusion of points with respect to the radar. The heading is to the y direction

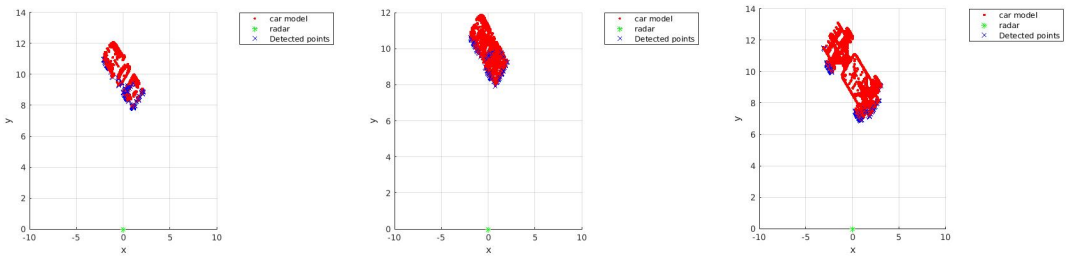

(a) Car model **(b)** Ferrari model **(c)** F1 model

Figure 5.8: Ground Truth of different car models from top view with detected points illustration of heading to -xy direction

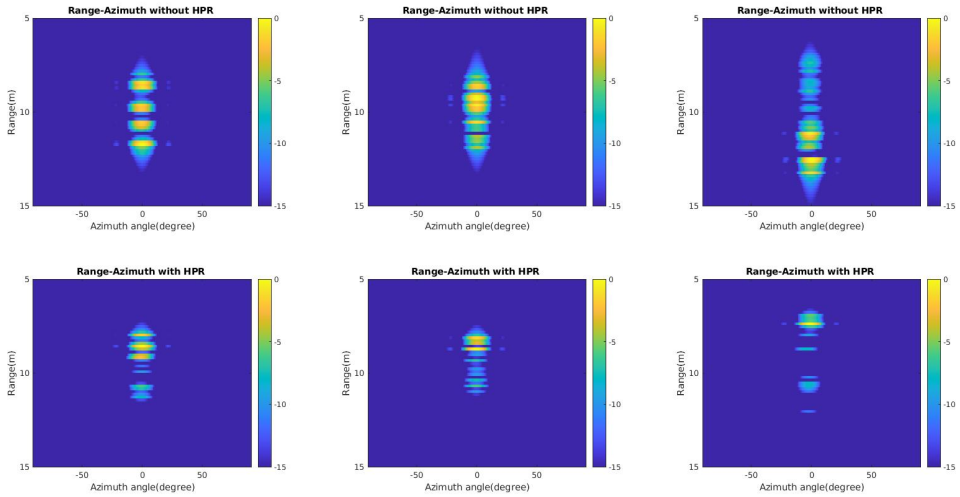

Figure 5.9: Simulated range-azimuth images of the car models shown in the previous figure without (top row) and with (bottom row) HPR algorithm to model occlusion of points with respect to the radar. The heading is to the -xy direction

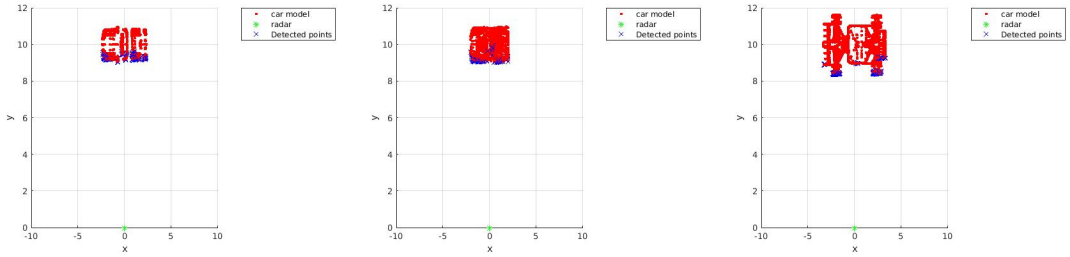

(a) Car model **(b)** Ferrari model **(c)** F1 model

Figure 5.10: Ground Truth of different car models from top view with detected points illustration of heading to -x direction

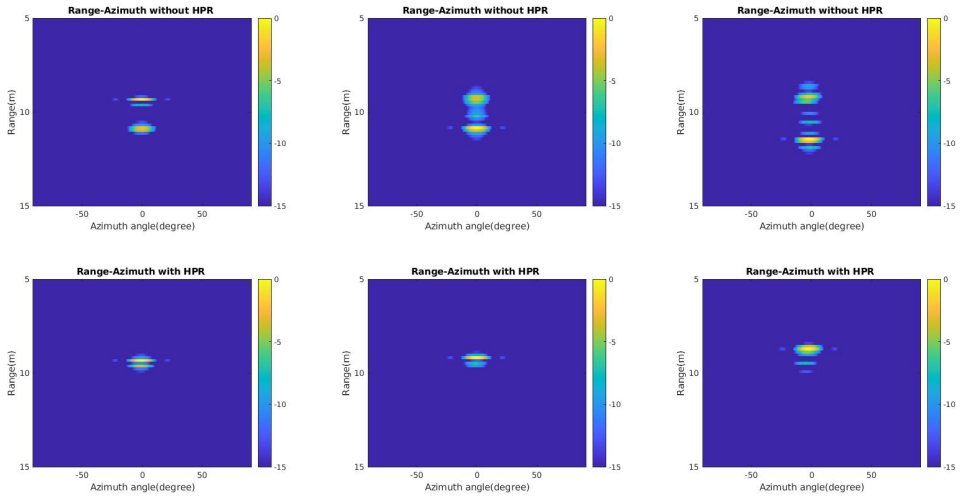

Figure 5.11: Simulated range-azimuth images of the car models shown in the previous figure without (top row) and with (bottom row) HPR algorithm to model occlusion of points with respect to the radar. The heading is to the -x direction

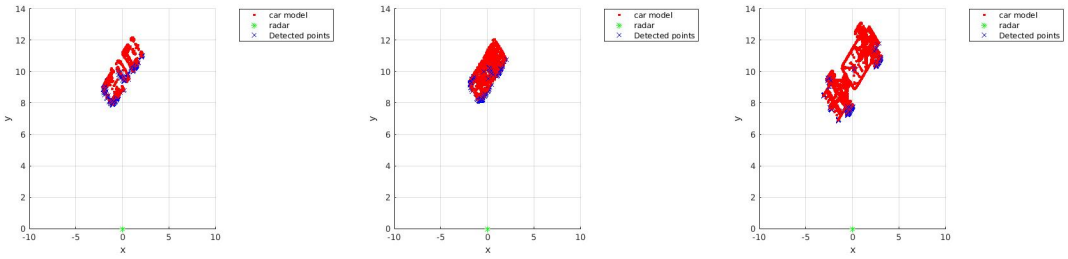

(a) Car model **(b)** Ferrari model **(c)** F1 model

Figure 5.12: Ground Truth of different car models from top view with detected points illustration of heading to -x-y direction

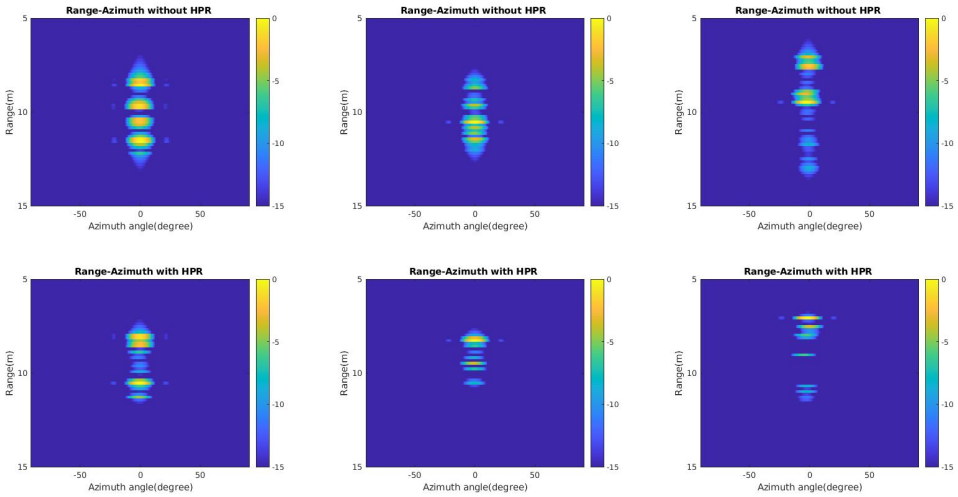

Figure 5.13: Simulated range-azimuth images of the car models shown in the previous figure without (top row) and with (bottom row) HPR algorithm to model occlusion of points with respect to the radar. The heading is to the -x-y direction

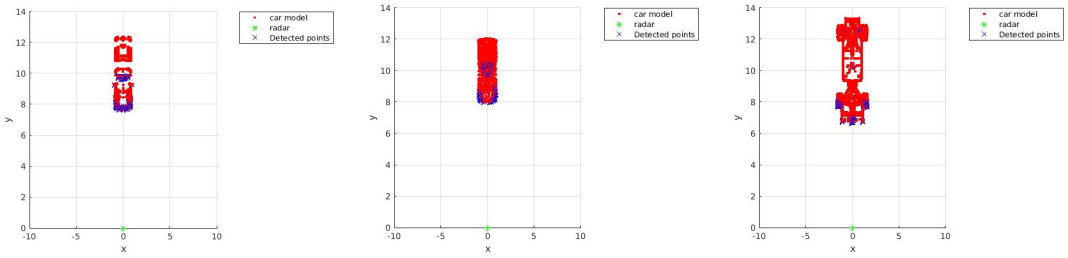

(a) Car model **(b)** Ferrari model **(c)** F1 model

Figure 5.14: Ground Truth of different car models from top view with detected points illustration of heading to -y direction

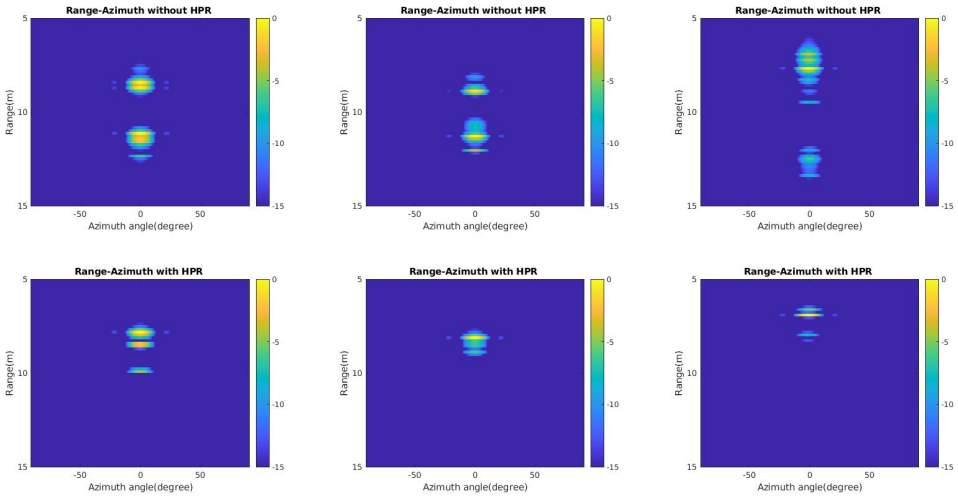

Figure 5.15: Simulated range-azimuth images of the car models shown in the previous figure without (top row) and with (bottom row) HPR algorithm to model occlusion of points with respect to the radar. The heading is to the -y direction

From the above results, it is noticeable that the different target car models could generate different results under different heading directions with and without HPR algorithm, which proves the initial steps to render realism of the proposed simulator. However, it needs to be outlined that the results are highly dependent on the specific car or vehicle model used. The higher the density of model points clouds, the better performance with the HPR algorithm could be achieved. This is important to notice as a characteristic of the developed simulator, whereby the number of points used for the generation of the actual radar signatures will strongly depend on the definition/resolution of the original CAD model.

5.2. Multi-targets simulation

To evaluate the performance of the simulator under different scene simulations, referred to as *multi-target simulations*, in this section, two simplified scenes containing different target models are built and presented with the aim of capturing two interesting situations in automotive scenarios, namely a pedestrian crossing the street in front of a parked car, and cars overtaking each other. Under these two scenes, the automotive radar is mounted on another approaching vehicle which will not be shown in the ground truth, but the radar position will be marked as a green star, as done before in other figures.

5.2.1. Car and crossing pedestrian

In this sub-section, the man and car models used before in single-target simulations are combined to build the traffic scene where a pedestrian is walking across the street in front of a parking car, while the radar-mounted car is moving toward the pedestrian. Figures 5.16,5.17,5.18 demonstrate the corresponding top view ground truth, range-azimuth images, and range-Doppler images in different frames, respectively.

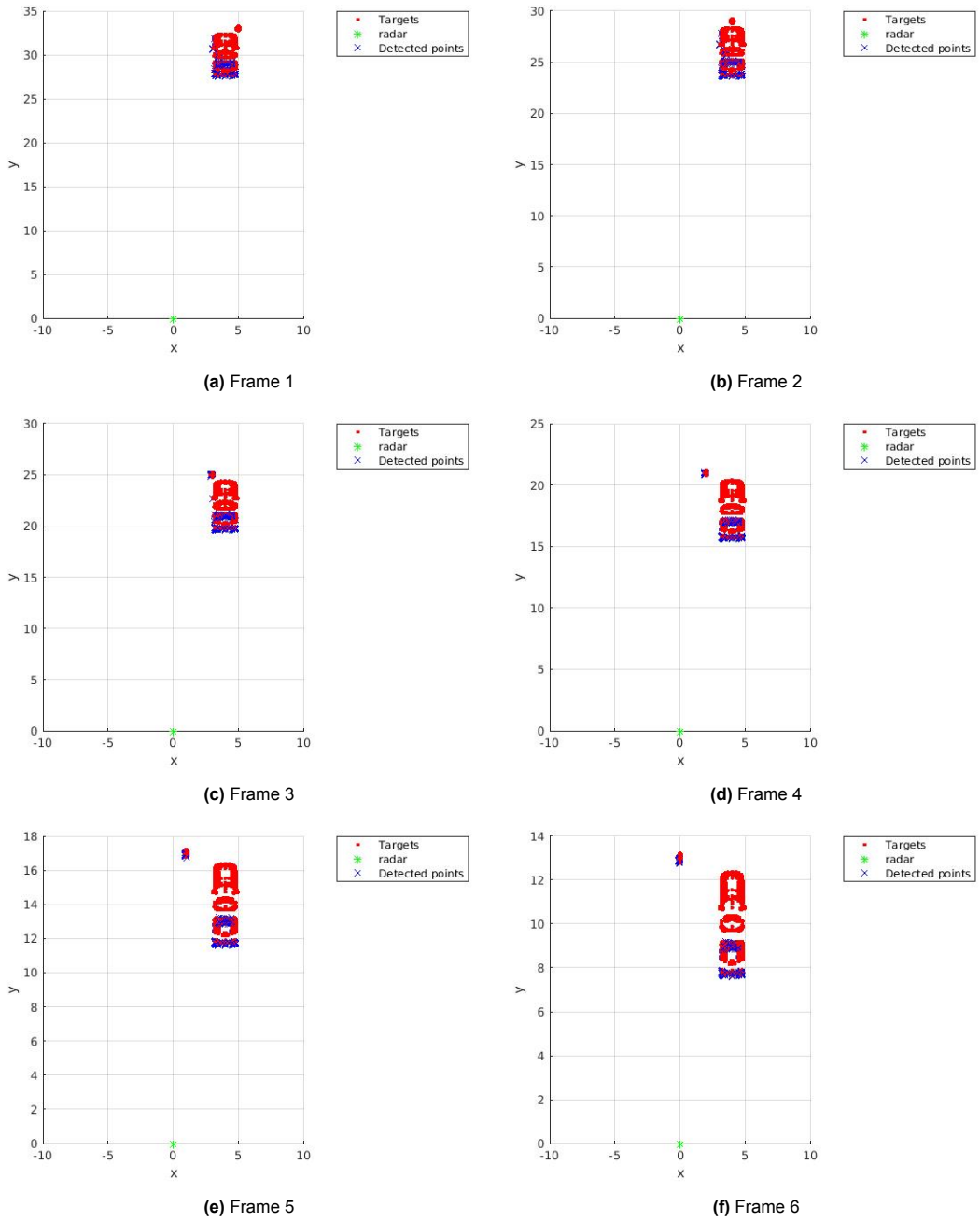

(a) Frame 1 **(b)** Frame 2

(c) Frame 3 **(d)** Frame 4

(e) Frame 5 **(f)** Frame 6

Figure 5.16: Pedestrian crossing from the side near a parked car in front of the radar. Different frames of ground truth (CAD models with HPR algorithm applied) are shown in top view

Through the ground truth figures, it could be found that, the pedestrian is supposed not to be visible by the radar in first two frames since there is detected labels on the pedestrian model which is a single right point located on the top left of car model. Since the third frame, the HPR algorithm predicates the pedestrian model is partially detectable with few detected points labeled. With frame changes, more and more blue labels are marked on the pesdestrian model and the marked points changed location on the pedestrian model, which satisfied the expectation of the assumption that, the pedestrian model will gradually appear in the radar view with more points being detected.

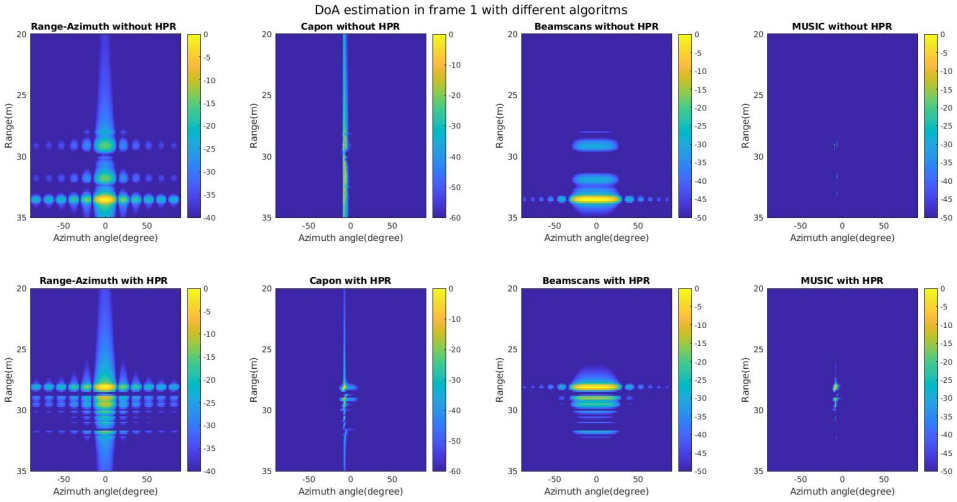

(a) Frame 1

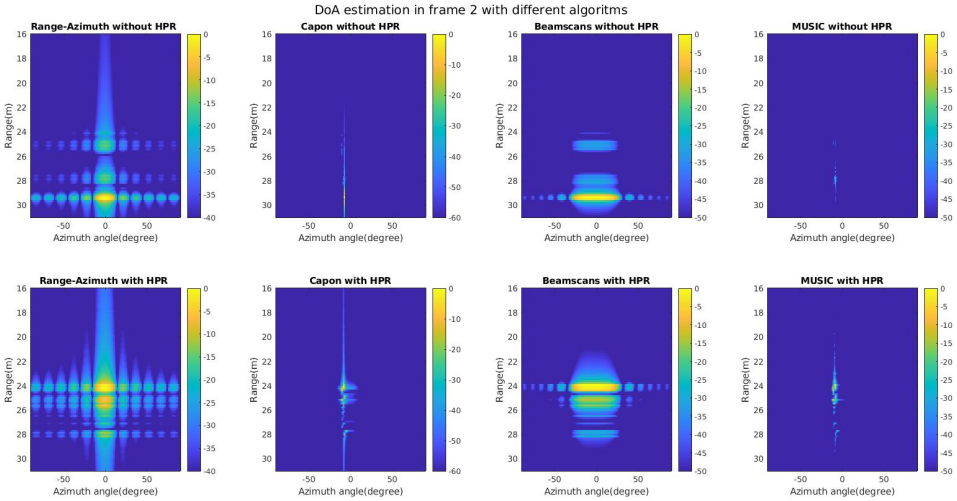

(b) Frame 2

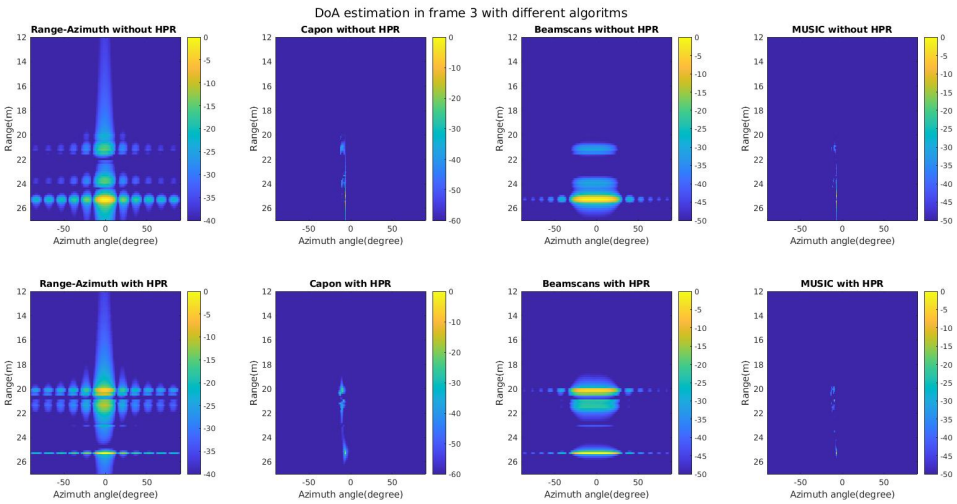

(c) Frame 3

Figure 5.17: Range-azimuth images of a pedestrian crossing from the side near a parked car in front of the radar. Six different frames are shown (a-f), with four different imaging algorithms applied per frame as well as the difference of applying the HPR algorithm or not

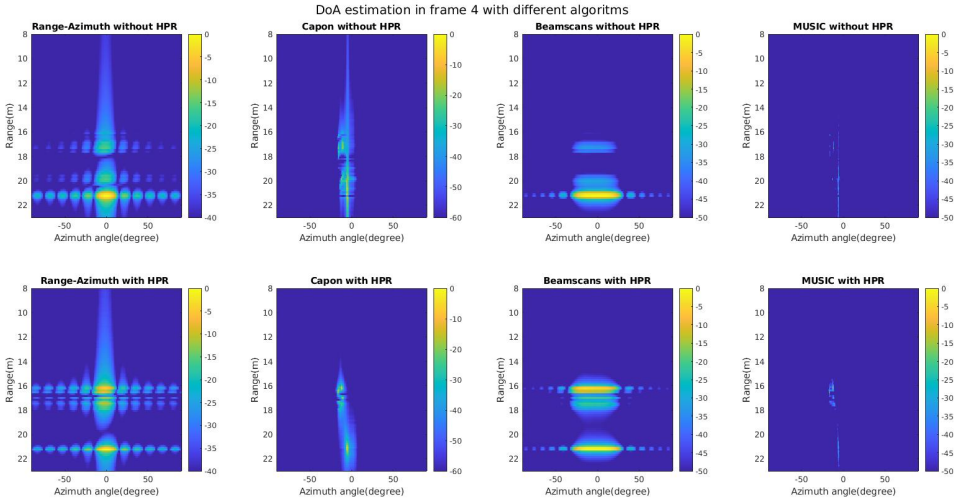

(d) Frame 4

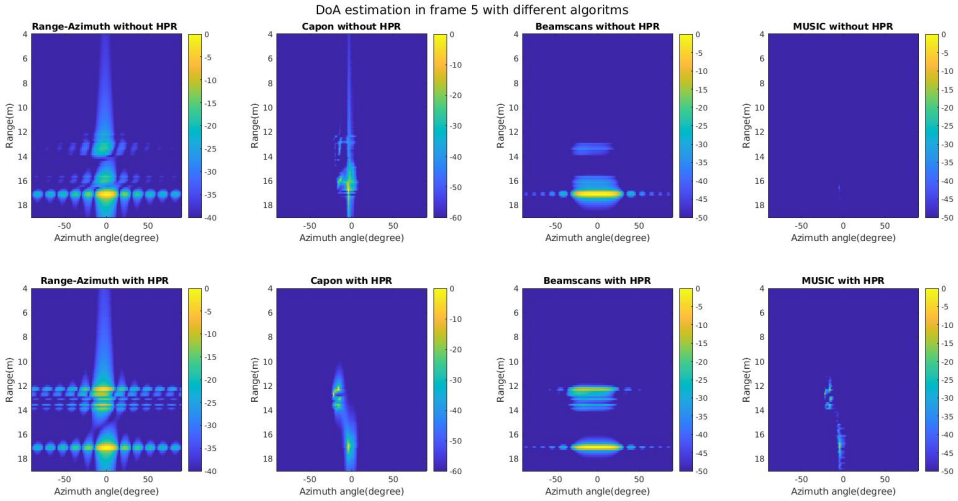

(e) Frame 5

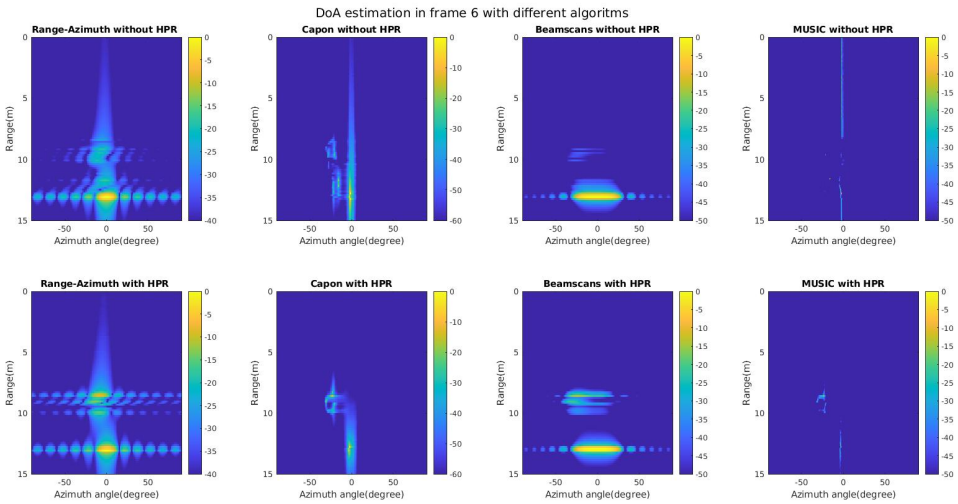

(f) Frame 6

Figure 5.17: Range-azimuth images of a pedestrian crossing from the side near a parked car in front of the radar. Six different frames are shown (a-f), with four different imaging algorithms applied per frame as well as the difference of applying the HPR algorithm or not

From the range-azimuth image shown above, it is obvious that beamscan and capon algorithms perform worse(rare points are detected) than traditional 2D FFT and beamscan algorithms for the simulated results without the HPR algorithm especially when the pedestrian is not visible. The reason for this is that, compared to the car model, the point clouds of the pedestrian model is more centralized in space which leads to the power concentrated on the position where the pedestrian model is located when the RCS value are identical for all the points. With HPR algorithm, the car model is more detectable when the pedestrian model is not visible at the first two frames. The range-azimuth images of the following four frames satisfied the ground truth described before.

Combined with the range-Doppler map shown below in Fig.5.18, The HPR algorithm could improve the signal reality in multi-target scene. The range-Doppler maps satisfied the illustration of ground truth that, the pedestrian is detectable since frame 3 and proved the feasibility of motion control in the coordinate systems.

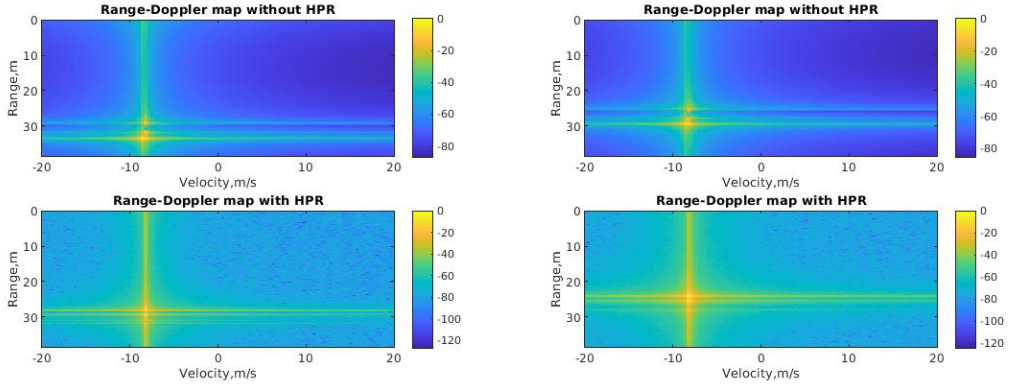

(a) Frame 1

(b) Frame 2

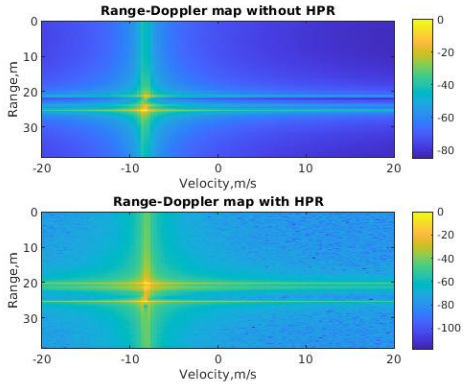

(c) Frame 3

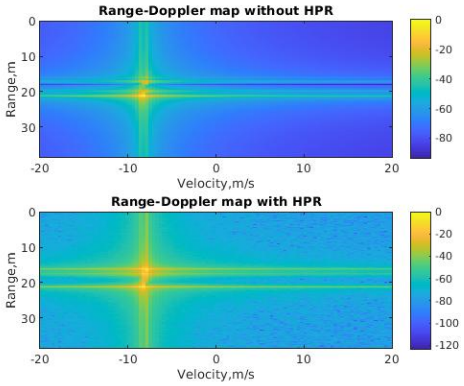

(d) Frame 4

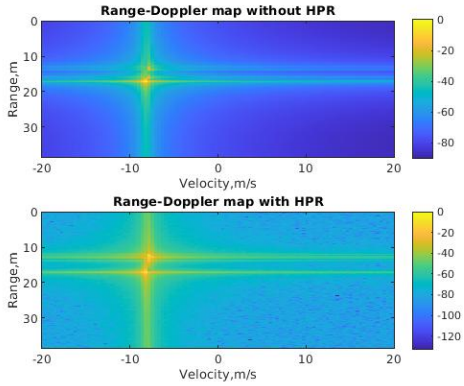

(e) Frame 5

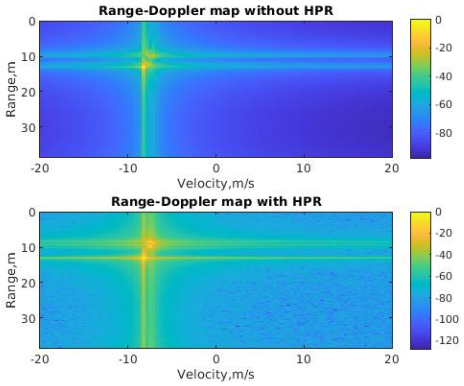

(f) Frame 6

Figure 5.18: Range-Doppler images of a pedestrian crossing from the side near a parked car in front of the radar. Six different frames are shown (a-f), with the difference of applying the HPR algorithm or not to model occlusion

5.2.2. Car overtaking

In this section, the traffic scene of car overtaking is simulated with two identical single-car models used in the previous section with identical point scatter RCS value. Basically, in this simulated scene the radar is mounted on a vehicle travelling in the direction of the positive y axis and two other cars are travelling in front, of which one is overtaking the other.

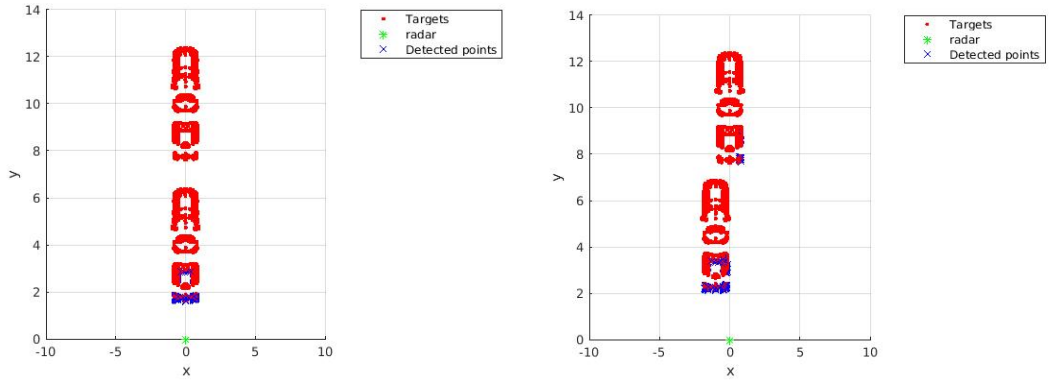

(a) Frame 1

(b) Frame 2

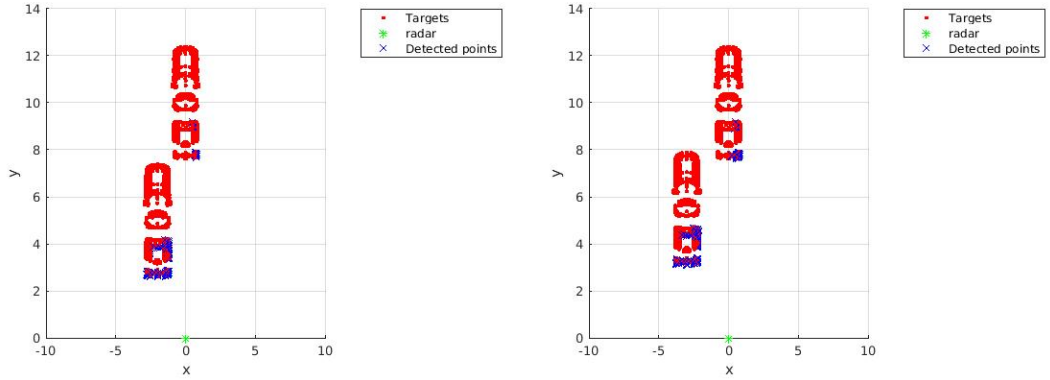

(c) Frame 3

(d) Frame 4

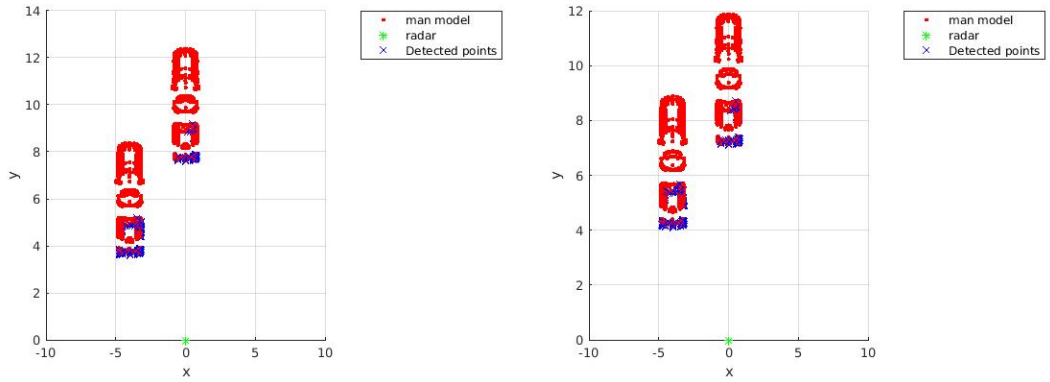

(e) Frame 5

(f) Frame 6

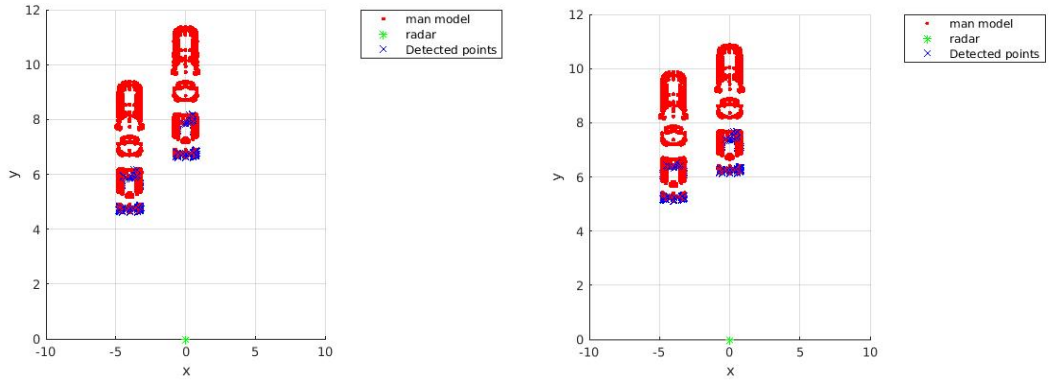

(g) Frame 7

(h) Frame 8

Figure 5.19: Car overtaking (to the -x direction first and then heading to y direction)top view ground truth. Different frames (a-h) of ground truth (CAD models with HPR algorithm applied) are shown in top view

During the car overtaking shown above, both car are heading to the y direction where the second car is overtaking the first one by steering to -x direction first and then drive to y direction. The overtaking drive is divided into to parts, the first four frame steering to -x direction and the rest four frame speed up to y direction. In the first four frames, since there is always a velocity heading to y direction, the overtaking car is doing shift motion to -xy direction with a different component velocity on y and -x direction while the overtaken car has a constant velocity to -y direction, acted like the mounted-radar car speeding up. Starting from the fifth frames, both car are only have velocity on y and -y direction until the end.

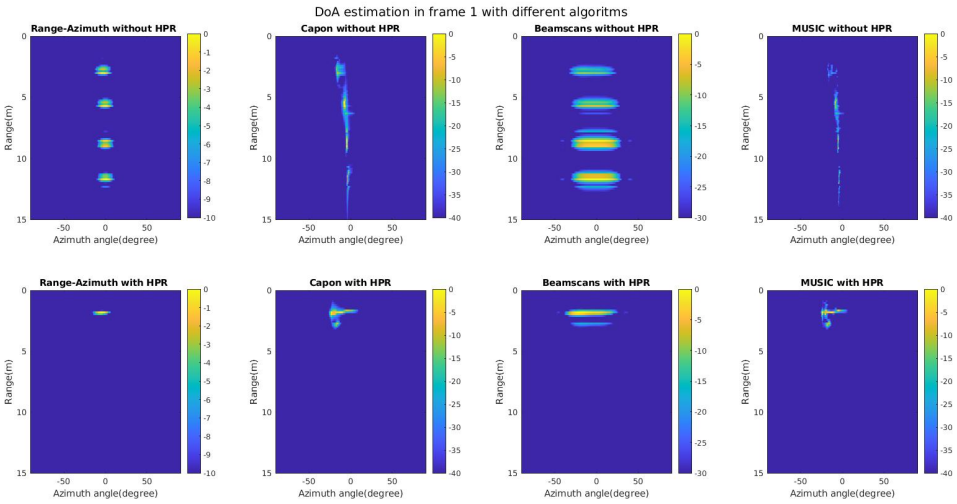

(a) Frame 1

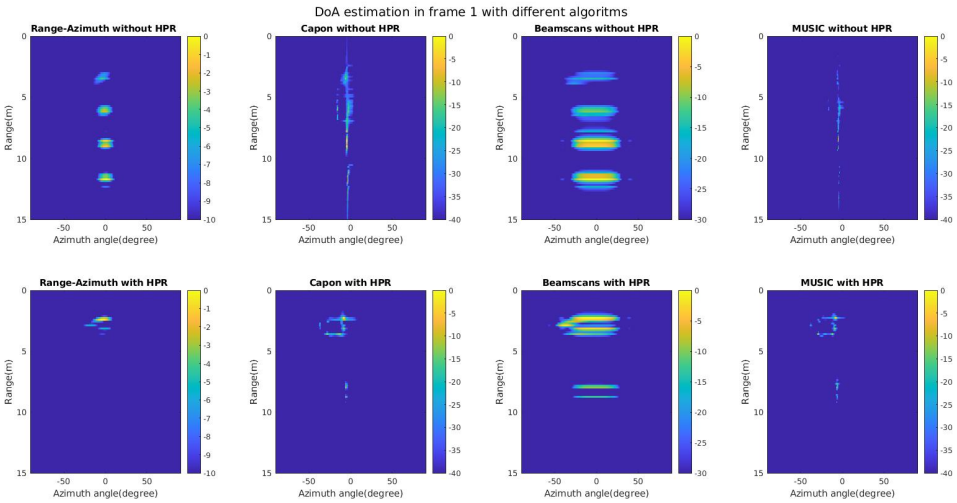

(b) Frame 2

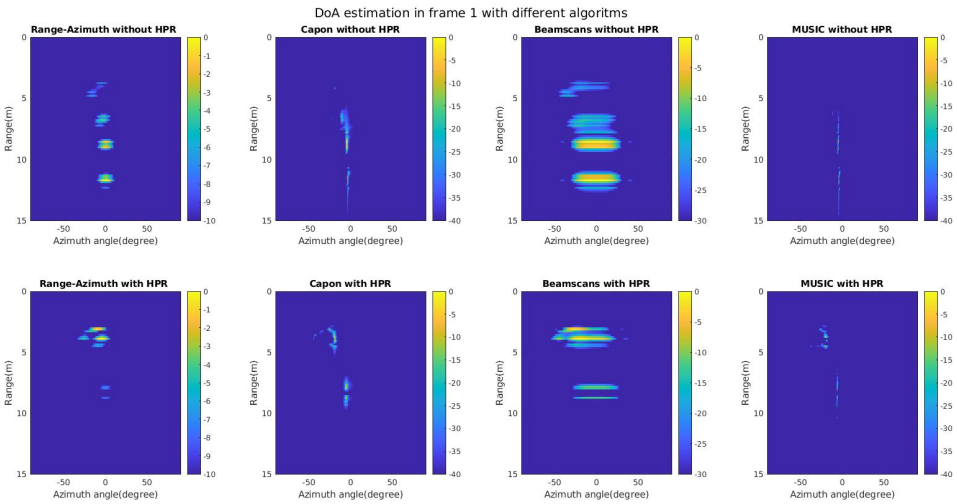

(c) Frame 3

Figure 5.20: Car overtaking simulated range-azimuth images. Eight different frames are shown (a-h), with the difference of applying the HPR algorithm or not to model occlusion

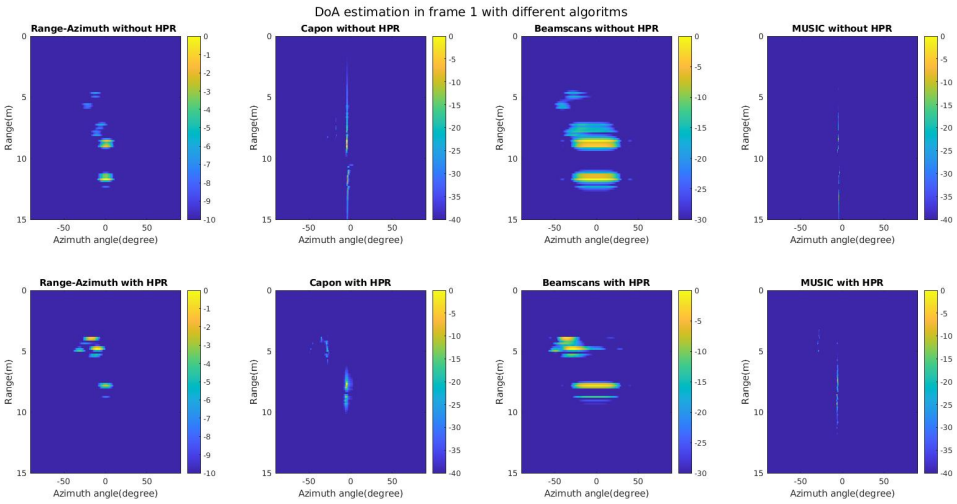

(d) Frame 4

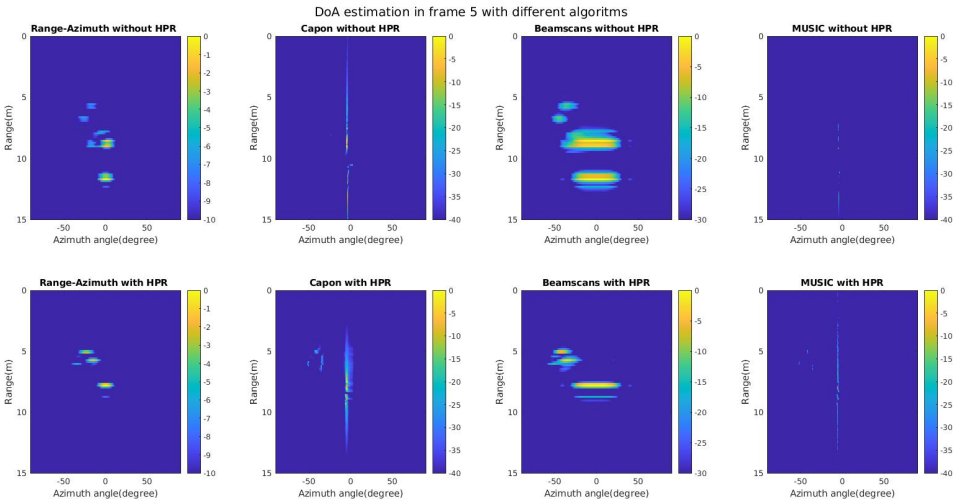

(e) Frame 5

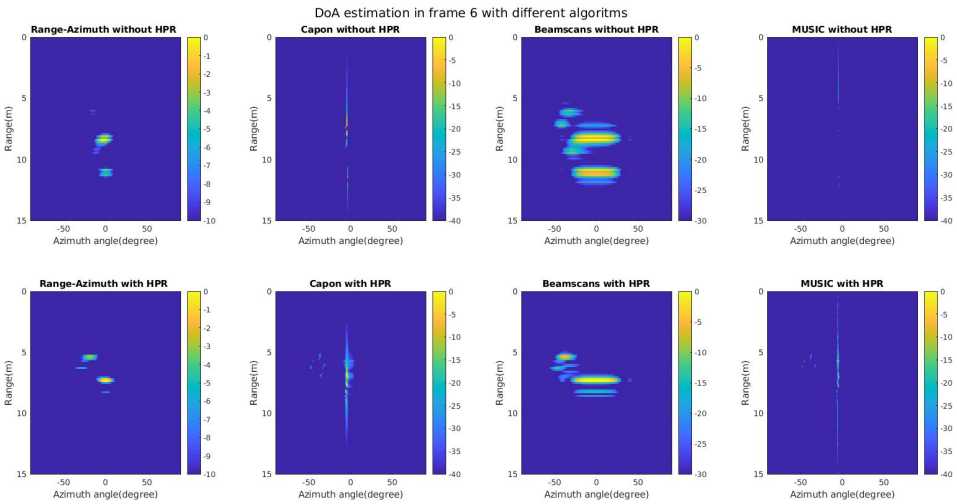

(f) Frame 6

Figure 5.20: Car overtaking simulated range-azimuth images. Eight different frames are shown (a-h), with the difference of applying the HPR algorithm or not to model occlusion

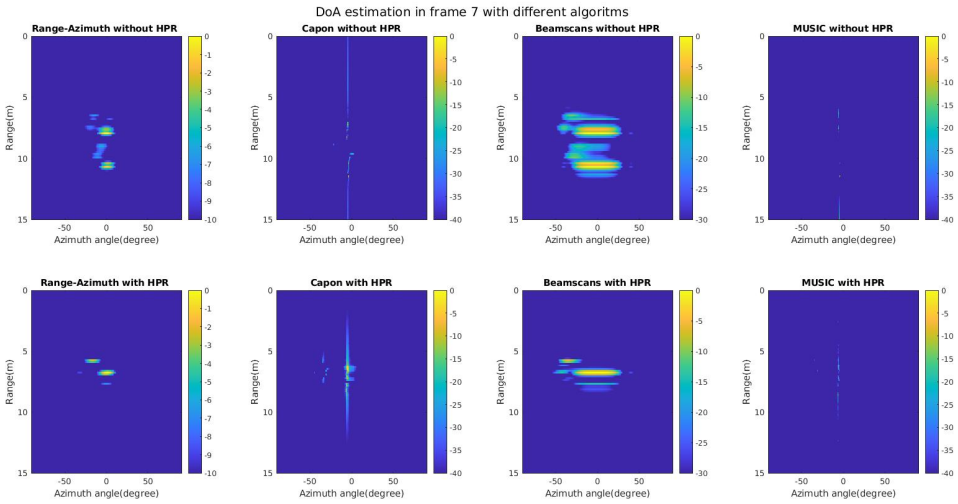

(g) Frame 7

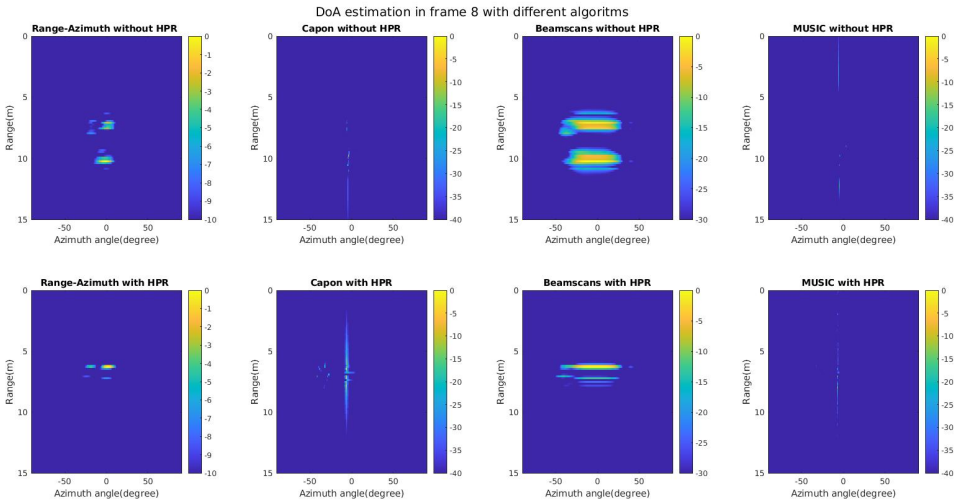

(h) Frame 8

Figure 5.20: Car overtaking simulated range-azimuth images. Eight different frames are shown (a-h), with the difference of applying the HPR algorithm or not to model occlusion

Figure.5.20 above shows the range-azimuth images based on the previously introduced car overtaking process. It is obvious that without HPR algorithm, multi-signals can be seen among the whole process, where HPR algorithm simulated more realistic signals starting with single reflected signal generated by overtaking car, and the overtaken car is fully invisible. With overtaking taking place, the overtaken car is gradually detected and reach to single line signal in the end when overtaking car and overtaken car drive parallel in the eighth frame.

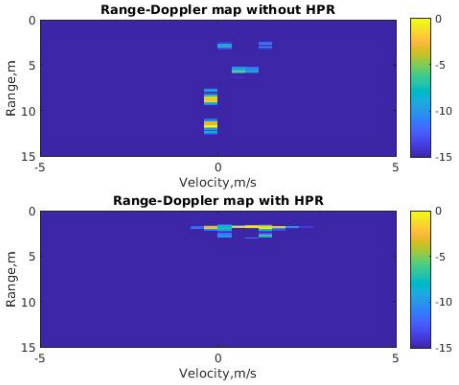

(a) Frame 1

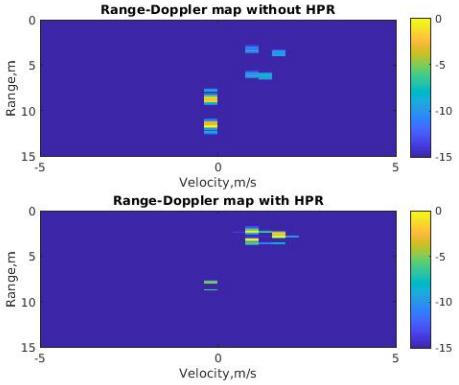

(b) Frame 2

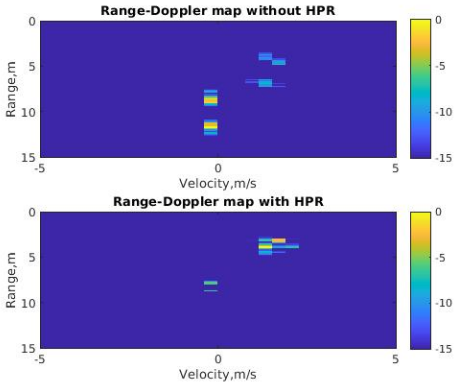

(c) Frame 3

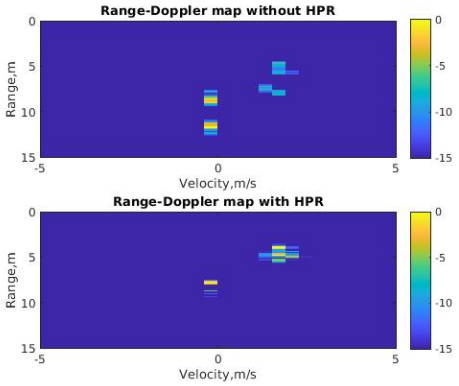

(d) Frame 4

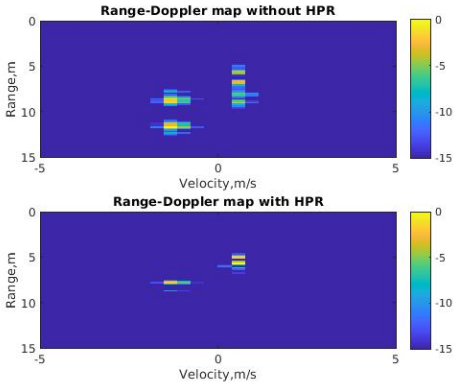

(e) Frame 5

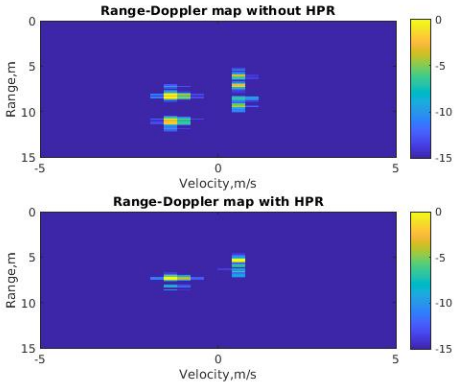

(f) Frame 6

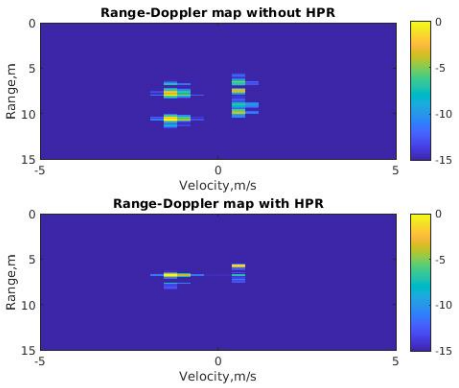

(g) Frame 7

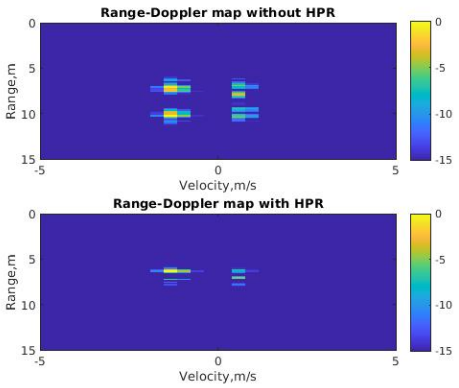

(h) Frame 8

Figure 5.21: Car overtaking simulated range-Doppler maps. Eight different frames are shown (a-h), with the difference of applying the HPR algorithm or not to model occlusion

Compared with range-azimuth images, the range-Doppler image could illustrate the overtaking more vividly, since the change of velocity is more visible in the range-Doppler map. In the first frame, it can be seen that the overtaking car has already steered the wheel, because a positive velocity could be seen, and without the HPR algorithm, the overtaken car's velocity could also be seen in the first frame. Simulated data without the HPR algorithm proved the feasibility of motion control since the overtaken car velocity could be kept seen, and the range between if and radar is decreasing. Additionally, the range-Doppler images without and with the HPR algorithm directly demonstrate the influence and accuracy of using the HPR algorithm for shadow point detection.

5.3. Simulator performance analysis

From the above-simulated results, the proposed simulator which uses dynamic point cloud generation from CAD models of targets, combined with the HPR algorithm to model occlusion and shadowing, could be employed to simulate complex single-target radar signatures and more elaborated scenes with multiple targets and their movements.

Compared to the integrated MATLAB simulator discussed in Chapter 2, the designed simulator increases the flexibility of model selection and provides extra features for detection and classification tasks, such as the change of shape/appearance under different heading directions, and the difference in the range-azimuth image of different car models. Another benefit of this simulator is high freedom in control, which means two aspects, the first one is motion control, which involves translational motion and rotational motion in 3D space. The second control aspect is depending on the user demand of trade-off between computation time and the reality, fidelity of the results.

Using realistic point clouds from CAD models for radar simulation increases the required computation, although the HPR algorithm can significantly reduce the load by removing the shadowed/occluded points. Based on the author's experience, the computation time is proportional to the point cloud's size, with an average of 300s of computation time on university servers for 8000 points in one frame, based on the simulation setting described at the beginning of the chapter. After applying the HPR algorithm, the computation time averagely shortens by ten times.

Nevertheless, it is important for future improvements of the proposed simulator to consider whether different approaches are possible to select the most salient points from the CAD models to be actually used for the radar simulator. A typical example is what happens with the wheels of the vehicles. In the original CAD models, the wheels contain a lot of points to model their curved shapes and many points remain even after the application of the HPR algorithm. However, these points are in terms of electromagnetic behavior weak scatterers due to the material (e.g. tires) and curved shape, with respect for instance to the flat metallic parts of the car chassis. Hence, additional work to refine the selection of points from the CAD model to the simulator can be an interesting direction of improvement.

Besides that, another point of improvement is related to the HPR algorithm. For multi-targets scenes, this could not accurately remove the shadowed points as for single-target. Due to the discontinuous distribution in space between two targets, the HPR algorithm could not effectively detect the non-shadowed points in the corner that occurred in 3D space. This is determined by its principle of the convex hull, which is accurate for detecting raised points on the surface.

6 Conclusion

As one of the strong supplements for lacking experimental data sets, simulation plays an important role in research. In the radar area, this is an even more important challenge than in other fields, since collecting experimental radar data is difficult and requires effort and hardware. Also, it is difficult to get the ground truth in real radar measurements. However, it is still a challenge to simulate good-quality radar signals. In the past decades, great progress has been made in radar simulations, from single-point targets to complex scene simulations.

By reviewing the development of radar simulation techniques and comparing the existing simulators, it is clear that to obtain realistic radar signals and signatures, there is always a trade-off between accuracy and computation. On the one hand, advanced simulation pursues accuracy with high-fidelity target models and complex propagation computation with the help of powerful solvers. On the other hand, conventional simulation aims at fast computation for acceptable results, but compromises the simulation reality, i.e. the complexity and the realism of the scene depicted, for instance in terms of number of targets or their movements.

Within this thesis, the work was focused on designing and building the FMCW MIMO radar simulator for realistic extended targets under the balance between computation time and simulation accuracy. The simulated results in this thesis proved that using dynamic point clouds with the help of the HPR algorithm can enable to simulate more realistic results containing important features for target classification, such as heading direction information and shapes of targets of interest.

The main contribution of the thesis could be briefly summarized below,

- The FMCW MIMO radar simulator is systematically analyzed and designed.
- A Motion control system containing coordinate transform is built
- Detailed analysis is provided and the simulated results using dynamic point clouds and HPR algorithm are summarized for scenes of interest in automotive, such as pedestrian crossing in front of the radar and cars overtaking each other

Future work could be focused on exploiting more advanced algorithms for accurate removal of shadowed/occluded points and adding multi-path into the simulation for more realistic simulation. Besides, also mentioned by M.Moore[28], a further study could be related to the radar cross-section (RCS) influence on dynamic points clouds simulation results. Last but not least, adapting the radar design for new generation 4D radar could be another challenging research direction.

References

[1] Khan Muhammad et al. “Deep learning for safe autonomous driving: Current challenges and future directions”. In: *IEEE Transactions on Intelligent Transportation Systems* 22.7 (2020), pp. 4316–4336.

[2] You Li and Javier Ibanez-Guzman. “Lidar for autonomous driving: The principles, challenges, and trends for automotive lidar and perception systems”. In: *IEEE Signal Processing Magazine* 37.4 (2020), pp. 50–61.

[3] Joel Janai et al. “Computer vision for autonomous vehicles: Problems, datasets and state of the art”. In: *Foundations and Trends® in Computer Graphics and Vision* 12.1–3 (2020), pp. 1–308.

[4] Shunqiao Sun, Athina P Petropulu, and H Vincent Poor. “MIMO radar for advanced driver-assistance systems and autonomous driving: Advantages and challenges”. In: *IEEE Signal Processing Magazine* 37.4 (2020), pp. 98–117.

[5] Taohua Zhou et al. “MMW radar-based technologies in autonomous driving: A review”. In: *Sensors* 20.24 (2020), p. 7283.

[6] Yi Zhou et al. “Towards deep radar perception for autonomous driving: Datasets, methods, and challenges”. In: *Sensors* 22.11 (2022), p. 4208.

[7] Holger Caesar et al. “nuscenes: A multimodal dataset for autonomous driving”. In: *Proceedings of the IEEE/CVF conference on computer vision and pattern recognition*. 2020, pp. 11621–11631.

[8] Dan Barnes et al. “The oxford radar robotcar dataset: A radar extension to the oxford robotcar dataset”. In: *2020 IEEE International Conference on Robotics and Automation (ICRA)*. IEEE. 2020, pp. 6433–6438.

[9] Michael Meyer and Georg Kuschk. “Automotive radar dataset for deep learning based 3d object detection”. In: *2019 16th european radar conference (EuRAD)*. IEEE. 2019, pp. 129–132.

[10] Nicolas Scheiner et al. “Seeing around street corners: Non-line-of-sight detection and tracking in-the-wild using doppler radar”. In: *Proceedings of the IEEE/CVF Conference on Computer Vision and Pattern Recognition*. 2020, pp. 2068–2077.

[11] Yizhou Wang et al. “Rodnet: Radar object detection using cross-modal supervision”. In: *Proceedings of the IEEE/CVF Winter Conference on Applications of Computer Vision*. 2021, pp. 504–513.

[12] Marcel Sheeny et al. “RADIATE: A radar dataset for automotive perception in bad weather”. In: *2021 IEEE International Conference on Robotics and Automation (ICRA)*. IEEE. 2021, pp. 1–7.

[13] Arthur Ouaknine et al. “Carrada dataset: Camera and automotive radar with range-angle-doppler annotations”. In: *2020 25th International Conference on Pattern Recognition (ICPR)*. IEEE. 2021, pp. 5068–5075.

[14] Mohammadreza Mostajabi et al. “High-resolution radar dataset for semi-supervised learning of dynamic objects”. In: *Proceedings of the IEEE/CVF Conference on Computer Vision and Pattern Recognition Workshops*. 2020, pp. 100–101.

[15] Teck-Yian Lim, Spencer A Markowitz, and Minh N Do. “RaDICaL: A Synchronized FMCW Radar, Depth, IMU and RGB Camera Data Dataset With Low-Level FMCW Radar Signals”. In: *IEEE Journal of Selected Topics in Signal Processing* 15.4 (2021), pp. 941–953.

[16] Ole Schumann et al. “RadarScenes: A real-world radar point cloud data set for automotive applications”. In: *2021 IEEE 24th International Conference on Information Fusion (FUSION)*. IEEE. 2021, pp. 1–8.

[17] Rob Weston, Oiwi Parker Jones, and Ingmar Posner. “There and Back Again: Learning to Simulate Radar Data for Real-World Applications”. In: *2021 IEEE International Conference on Robotics and Automation (ICRA)*. 2021, pp. 12809–12816. DOI: 10.1109/ICRA48506.2021.9562111.

[18] Olivier Chadebec, J-L Coulomb, and Fleur Janet. “A review of magnetostatic moment method”. In: *IEEE Transactions on magnetics* 42.4 (2006), pp. 515–520.

[19] Olek C Zienkiewicz, Robert L Taylor, and Jian Z Zhu. *The finite element method: its basis and fundamentals*. Elsevier, 2005.

[20] John B Schneider. “Understanding the finite-difference time-domain method”. In: *School of electrical engineering and computer science Washington State University* 28 (2010).

[21] Henri-Jose Mametsa et al. “Imaging radar simulation in realistic environment using shooting and bouncing rays technique”. In: *SAR Image Analysis, Modeling, and Techniques IV*. Vol. 4543. SPIE. 2002, pp. 34–40.

[22] The MathWorks Inc. *backscatterPedestrian*. Natick, Massachusetts, United States, 2019. URL: https://www.mathworks.com/help/radar/ref/backscatterpedestrian.html.

[23] The MathWorks Inc. *backscatterBicyclist*. Natick, Massachusetts, United States, 2021. URL: https://www.mathworks.com/help/radar/ref/backscatterpedestrian.html.

[24] Ushemadzoro Chipengo, Arien Sligar, and Shawn Carpenter. “High fidelity physics simulation of 128 channel MIMO sensor for 77GHz automotive radar”. In: *IEEE Access* 8 (2020), pp. 160643–160652.

[25] Ushemadzoro Chipengo et al. “High fidelity physics simulation-based convolutional neural network for automotive radar target classification using micro-Doppler”. In: *IEEE Access* 9 (2021), pp. 82597–82617.

[26] Christian Schüßler et al. “A Realistic Radar Ray Tracing Simulator for Large MIMO-Arrays in Automotive Environments”. In: *IEEE Journal of Microwaves* 1.4 (2021), pp. 962–974. DOI: 10.1109/JMW.2021.3104722.

[27] Jörn Thieling, Susanne Frese, and Jürgen Roßmann. “Scalable and physical radar sensor simulation for interacting digital twins”. In: *IEEE Sensors Journal* 21.3 (2020), pp. 3184–3192.

[28] Matthew Moore, Duncan A Robertson, and Samiur Rahman. “Simulating UAV micro-Doppler using dynamic point clouds”. In: *2022 IEEE Radar Conference (RadarConf22)*. IEEE. 2022, pp. 01–06.

[29] Shengzhi Xu and Alexander Yarovoy. “Motion-Based Separation and Imaging of Closely Spaced Extended Targets”. In: *IEEE Sensors Journal* 20.22 (2020), pp. 13542–13551. DOI: 10.1109/JSEN.2020.3004909.

[30] The MathWorks Inc. *Radar Signal Simulation and Processing for Automated Driving*. Natick, Massachusetts, United States, 2022. URL: https://www.mathworks.com/help/radar/ug/radar-signal-simulation-and-processing-for-automated-driving.html.

[31] Victor C Chen. *The micro-Doppler effect in radar*. Artech house, 2019.

[32] Ronan Boulic, Nadia Magnenat Thalmann, and Daniel Thalmann. “A global human walking model with real-time kinematic personification”. In: *The visual computer* 6 (1990), pp. 344–358.

[33] Martin Stolz et al. “Multi-target reflection point model of cyclists for automotive radar”. In: *2017 European Radar Conference (EURAD)*. IEEE. 2017, pp. 94–97.

[34] Shengzhi Xu, Bert Jan Kooij, and Alexander Yarovoy. “Joint Doppler and DOA estimation using (Ultra-) Wideband FMCW signals”. In: *Signal Processing* 168 (2020), p. 107259.

[35] Xin Li et al. “Research on millimeter wave radar simulation model for intelligent vehicle”. In: *International Journal of Automotive Technology* 21 (2020), pp. 275–284.

[36] Shunqiao Sun, Athina P. Petropulu, and H. Vincent Poor. “MIMO Radar for Advanced Driver-Assistance Systems and Autonomous Driving: Advantages and Challenges”. In: *IEEE Signal Processing Magazine* 37.4 (2020), pp. 98–117. DOI: 10.1109/MSP.2020.2978507.

[37] Texas Instruments. *CD4007UB*. original document from TI Instrument. 2022. URL: https://www.ti.com/lit/ds/symlink/awr1843.pdf?HQS=dis-mous-null-mousermode-dsf-pf-null-wwe&ts=1691947200173&ref_url=https%253A%252F%252Fnl.mouser.com%252F.

[38] Tuomas Aittomaki and Visa Koivunen. “Performance of MIMO Radar With Angular Diversity Under Swerling Scattering Models”. In: *IEEE Journal of Selected Topics in Signal Processing* 4.1 (2010), pp. 101–114. DOI: 10.1109/JSTSP.2009.2038971.

[39] Sagi Katz, Ayellet Tal, and Ronen Basri. “Direct visibility of point sets”. In: *ACM SIGGRAPH 2007 papers*. 2007, 24–es.

[40] J. Capon. “High-resolution frequency-wavenumber spectrum analysis”. In: *Proceedings of the IEEE* 57.8 (1969), pp. 1408–1418. DOI: 10.1109/PROC.1969.7278.

[41] Florian Engels et al. “Advances in automotive radar: A framework on computationally efficient high-resolution frequency estimation”. In: *IEEE Signal Processing Magazine* 34.2 (2017), pp. 36–46.

A

Comparison of datasets charastics and radar data details

In this section, some comparisons between previous introduced nine automotive radar datasets are shown below. From Table.A.1, it is noticeable that most of the automotive driving data set are released in recent three years, which indicates the lack of research in this field. Additionally, the data size are various from few gigabytes to hundreds of gigabytes (small size refers full data is smaller than 10GB, large means the data set is over 100GB, and medium is the data size between 10GB to 100GB).

Considered complexity of the traffic in reality, scenarios and object category number are the other two important conditions for the data set. Apparently, there is a trade-off between data size and scenarios and object category. Only in the large dataset, it is possible to include various scenarios and more object category. However, on the other hand, a large data size leads to the significantly increment in annotation. Meanwhile, to correctly understand the scene for automotive driving, more annotated objects means a better decision will be made by computer in the future. In the table, most of the data set only contains several types of annotated targets. One commonly-mentioned challenge among these data set is accurate annotation.

Table A.1: Dataset information

Dataset	Year	Other Modalities	Data size	Object Category	Scenarios	Label
Radar Scenes	2021	Camera	Medium	11	++	Yes
nuScene	2018	Lidar, Camera	Large	23	++	Yes
Asytax	2019	Lidar, Camera	Small	7	-	Yes
RaDICal	2021	RGB-D Camera	Large	2	-	No
NLOS	2020	Lidar	Small	2	-	Yes
CRUW	2020	Camera	Medium	3	++	Yes
RADIATE	2020	Lidar, Camera	Large	8	++	Yes
CARRADA	2020	Camera	Large	3	-	Yes
Oxford	2019	Lidar, Camera	Large	0	+	No
Zendar	2020	Lidar, Camera	Large	1	+	Yes

In Table. A.2, the radar related information is listed including radar resolution, data format, annotation method, and training model availability. Among these data, raw data is only very rarely provided, as most of the radar data are preprocessed radar point clouds. Some are range-azimuth images due to the limit of the used-radar. At the same time, the annotation is different for different datasets.

Table A.2: Radar data information

Dataset	Radar type	Radar resolution	Radar data format	Annotation	Help tools	Model
Radar Scenes	FMCW	Detection range<100m, Range resolution=0.15m, Velocity resolution=0.1km/h, Angular resolution=0.5° at boresight to 2° at the FoV border	2D point clouds	Point wise	Yes	No
nuScene	FMCW	Detection range<250m, Range resolution=0.1km/h,	3D point clouds	3D box	Yes	No
Asytax	FMCW	N/A	3D point clouds	3D box	No	No
RaDICal	FMCW	N/A	Raw data	Spectral box	Yes	Yes
NLOS	FMCW	Detection Range<153m, Range resolution=0.15m, Velocity resolution=0.087m/s, Angular resolution=1.8°	2D point clouds	Point wise	No	Yes
CRUW	FMCW	N/A	Range-azimuth array	Spectral box	Yes	Yes
RADIATE	Scanning FMCW	Detection range<100m, Range resolution=0.175m, Azimuth resolution=1.8°, Elevation resolution=1.8°.	Range-azimuth image	2D Box	Yes	No
CARRADA	FMCW	Detection range<50m, Range resolution=0.2m, Velocity resolution=0.42m/s, Angular resolution=0.70°	Raw data	Spectral box	Yes	Yes
Oxford	Scanning FMCW	Detection range<163m, Range resolution=4.38cm, Angular resolution=1.8°	Range-azimuth image	No	Yes	Yes
Zendar	FMCW	Detection range<90m, Range resolution=18cm, Azimuth resolution=0.1°	Raw data, SAR image and BEV 2D point clouds	Not mentioned	Yes	No

In conslusion, it is extremely difficult to compare different datasets with or without related models. Ignored the computation requirements, on the one hand, training models are limited and mainly designed for one special data set. On the other hand, the diversity in terms of sensor using, radar parameters, data format, annotation, and object category limits the evaluation performance of different state-of-art neural network models using different datasets.